

University of Strathclyde
Department of Mechanical Engineering

Novel computational methods to predict
the deformation of macroscopic
heterogeneous materials

A. J. Beveridge

A thesis presented in fulfilment of the requirements for the degree
of Doctor of Philosophy

2011

This thesis is the result of the author's original research. It has been composed by the author and has not been previously submitted for examination which has led to the award of a degree.

The copyright of this thesis belongs to the author under the terms of the United Kingdom Copyright Acts as qualified by University of Strathclyde Regulation 3.50. Due acknowledgement must always be made of the use of any material contained in, or derived from, this thesis.

Signed:

Date:

Acknowledgements

I must give special thanks to Dr Wheel for his diligent supervision. It was always an encouragement to know someone else was thinking about my work, willing to throw ideas around and steer the work in the right direction. Thanks also to Dr Nash for his pastoral support, particularly in the last year when employment took me away from Glasgow. And finally to Andy Crockett for helping with the experimental testing, Tommy Sherwood for the design and preparation of the aluminium model material and Afan Waseem for the experimental acrylic ring results.

To name and thank all who have given me support and help throughout the PhD, to repay their time in equal measure with the words about them, would take many times the length of this thesis.

Whether I have written many words about you, just a few or none at all, please know that I am very grateful to everyone who listened and humoured me throughout the ups and downs of these past years.

Thank you.

These words have been my goal:

“What ever you do work heartily, as for the Lord and not for men, knowing that from the Lord you will receive the inheritance as your reward. You are serving the Lord Christ”

Colossians 3:23-24 (ESV)

Contents

1	Introduction	2
1.1	Experimental Methods in Micropolar Elasticity	4
1.2	Numerical Methods in Micropolar Elasticity	7
1.3	Research Aims	9
2	Micropolar Elasticity	12
2.1	Generalised Linear Micropolar Elasticity	12
2.2	Two Dimensional Formulations	14
2.2.1	Plane Strain	17
2.2.2	Plane Stress	18
2.3	One Dimensional Formulations	19
2.3.1	Slender Beam	19
2.3.2	Thin Walled Ring	23
2.4	Conclusion	25

3	Model Material - Slender Beam	27
3.1	Experimental Procedure	30
3.2	Detailed Finite Element Analysis	33
3.3	Results	39
3.4	One Dimensional Beam Finite Element	42
3.4.1	Validation	44
3.4.2	Slender Beam Comparison	45
3.5	Conclusion	47
4	Control Volume Finite Element Method	49
4.1	Discrete Kirchhoff Triangular Element	50
4.2	Micropolar Linear Strain Triangular Element	51
4.2.1	Control Volume Formulation	55
4.2.2	Validation	61
4.3	Conclusion	70
5	Model Material - Deep Beam	71
5.1	Experimental Results	73
5.2	Iterative Constitutive Code	79
5.2.1	Procedure	79
6	Model Material - Diametrically Loaded Ring	86
6.1	Constitutive Properties	89

6.2	Discussion	90
7	Summary and Conclusions	93
A	Discrete Kirchhoff Triangular Element	97
A.1	Mindlin Plate Bending Theory	97
A.1.1	Deformations	97
A.1.2	Moment Curvature Relations	98
A.1.3	Equilibrium	99
A.2	DKT Element	99
A.3	Element Stiffness Matrix	102
A.3.1	Finite Element Method	102
A.3.2	Control Volume Finite Element Method	103
A.4	Boundary Conditions and Solution	107
A.5	Results	107
A.5.1	Patch Test	108
A.5.2	Uniformly Distributed Load (UDL)	109
A.5.3	Centrally Applied Load	109
A.5.4	Boundary Conditions	111
A.6	Conclusion	111
B	MATLAB Control Volume Finite Element Codes	117
B.1	CV-DKT	117
B.2	CV-MPLST	123

C	MATLAB Iterative Constitutive Code	132
C.1	MicropolarBeamREGbeta Code	132
D	Ansys Discrete Detail Input Files	136
D.1	HMD Geometry Input B1	136
D.2	LMD Geometry Input B1	138

List of Figures

2.1	Micropolar differential stress element	15
2.2	Deformation of stress element due to antisymmetric, τ_a , and symmetric, τ_s , shear stresses	16
2.3	Stress acting upon a one dimensional micropolar beam	20
2.4	Model beam subjected to three point bending	21
2.5	Model ring subject to diametrically opposing point loads	23
3.1	Diagram of hole pitch with horizontal pitch P_1 and vertical pitch P_2	28
3.2	Photograph of HMD test pieces	29
3.3	(a) LMD_B1 in three point bending with cross head measurement only (b) HMD_B1 in three point bending with independent central defection reading from extensometer	31
3.4	Test data plot from Microsoft Excel showing load displacement curve for HMD_B1_10 with fitted straight line and equation of straight line shown with gradient highlighted in box	32
3.5	Diagram showing relative crosshead and rig flexure displacements for three point bending experimental procedure	32
3.6	Stiffness against $1/\text{depth}^2$ for HMD beams at $L/d = 10.08$. Comparing discrete detail ANSYS, experimental results and experimental results corrected for test rig flexure against classical solution .	33

3.7	Stiffness against $1/\text{depth}^2$ for LMD beams at $L/d = 9.92$. Comparing discrete detail ANSYS, experimental results and experimental results corrected for test rig flexure against classical solution	34
3.8	Flow chart showing the sequence of steps used to create the detailed finite element beam geometry	35
3.9	Array of unit cells and half unit cells to create detailed beam geometry	36
3.10	Convergence of absolute central deflection against number of nodes for HMD_B1_10 geometry, comparing ANSYS elements 182 and 183	37
3.11	Convergence of absolute central deflection against number of nodes for LMD_B1_10 geometry, comparing ANSYS elements 182 and 183	37
3.12	Quarter mesh for HMD discrete detail finite element model. Mesh refinement parameter <code>refine= 1</code> , 378 nodes	38
3.13	Quarter mesh used in LMD discrete detail finite element model. Mesh refinement parameter <code>refine= 0.5</code> , 62 nodes	39
3.14	Beam element	43
3.15	Tip displacement convergence to couple stress beam theory for cantilever beam at various depth to characteristic length ratios . .	45
3.16	Stiffness result from Micropolar Beam element (EXPBeamE) for a given load ($100N$). Plotted against stiffness from the experimental procedure (EXP).	46
3.17	Stiffness result from Micropolar Beam element (ANSYSBeamE) for a given load ($100N$). Plotted against displacements gained from the ANSYS procedure (ANSYS).	46
4.1	Six node quadratic displacement triangular element	52

4.2	Dual control volume mesh constructed around the vertices of a six node triangular finite element mesh	55
4.3	Sign conversion for dual mesh on a single finite element mesh	56
4.4	Element stress resultants working on the face of the control volume	58
4.5	Mesh for micropolar element patch test, lengths in (mm)	62
4.6	Stress concentration mesh 8x15x4 $r = 0.864\text{mm}$. Quarter plate edge lengths are 16.2mm x 16.2mm.	65
4.7	Convergence to slender beam solution for increasing degrees of freedom	68
4.8	Time to solution for slender beam solution for increasing degrees of freedom	68
4.9	Unit beam mesh	69
5.1	Stiffness against $1/\text{depth}^2$ at $L/d = 7.56$ for various coupling numbers with material properties from slender HMD beams	72
5.2	Stiffness against $1/\text{depth}^2$ at $L/d = 5.04$ for various coupling numbers with material properties from slender HMD beams	72
5.3	Stiffness against $1/\text{depth}^2$ for HMD beams at $L/d = 7.56$. Comparing discrete detail ANSYS and experimental results corrected for test rig flexure against classical solution	76
5.4	Stiffness against $1/\text{depth}^2$ for HMD beams at $L/d = 5.04$. Comparing discrete detail ANSYS and experimental results corrected for test rig flexure against classical solution	76
5.5	Stiffness against $1/\text{depth}^2$ for LMD beams at $L/d = 8.50$. Comparing discrete detail ANSYS and experimental results corrected for test rig flexure against classical solution	77

5.6	Stiffness against $1/\text{depth}^2$ for LMD beams at $L/d = 5.67$. Comparing discrete detail ANSYS and experimental results corrected for test rig flexure against classical solution	77
5.7	Unit mesh used for HMD $L/d=10.08$	80
5.8	Best fit solutions for HMD samples based upon the ANSYS results at the three different spans after the first iteration to find the coupling number N using $L/d = 5.04$, $R^2 = 0.93$ at this span . . .	82
5.9	Flow chart showing iterative process to find the best fit material parameters for the HMD model material	83
5.10	Best fit solutions for HMD samples based upon the ANSYS results at the three different spans after the second iteration to find the couple modulus γ using $L/d = 10.08$, $R^2 = 0.99$ at this span . . .	84
5.11	Variation of stiffness for $\pm 15\%$ Poisson's ratio for different spans HMD	85
6.1	Model ring of radius R and depth d with radial void distribution dimensions of pitch n , pitch radius r_n , initial offset angle θ_{ni} and offset angle θ_n	87
6.2	Best fit solution for ring samples based upon experimental stiffness results	90
6.3	Flow chart showing iterative process to find the best fit material parameters from the model ring experimental results	92
A.1	Differential plate element undeformed (a) and deformed plate(b) .	98
A.2	Transition to the DKT element. (a) 6 noded Mindlin element with the triangular area coordinates δ , ξ and η . (b) 3 noded DKT element with vertex node degrees of freedom $(w_i, w_{,xi} w_{,yi})$. .	100

A.3	(a) Control volume dual mesh centred on finite element node P (b) Equilibrium of forces acting upon a differential line dr along the control volume face	103
A.4	(a) Element coordinate systems: global Cartesian, line and area. Element and control volume node labelling convention (b) Specific area coordinates relating to element and control volume nodes . .	106
A.5	Triangular mesh of 2x2 square plate of dimensions a and b	108
A.6	Patch test mesh	109
A.7	Central deflection convergence to thin plate theory. Hard clamped with uniform load, $a/b = 1$ and $h = 0.05$	112
A.8	Central deflection convergence to thin plate theory. Soft clamped with uniform load, $a/b = 1$ and $h = 0.05$	112
A.9	Central deflection convergence to thin plate theory. Hard simply supported with uniform load, $a/b = 1$ and $h = 0.05$	113
A.10	Central deflection convergence to thin plate theory. Soft simply supported with uniform load, $a/b = 1$ and $h = 0.05$	113
A.11	Central deflection convergence to thin plate theory. Hard clamped with central point load, $a/b = 1$ and $h = 0.05$	114
A.12	Central deflection convergence to thin plate theory. Soft clamped with central point load, $a/b = 1$ and $h = 0.05$	114
A.13	Central deflection convergence to thin plate theory. Hard simply supported with central point load, $a/b = 1$ and $h = 0.05$	115
A.14	Central deflection convergence to thin plate theory. Soft simply supported with central point load, $a/b = 1$ and $h = 0.05$	115
A.15	Convergence of rotation about the normal along plate boundary for CVFEM. Soft simply supported with central point load, $a/b = 1$ and $h = 0.05$	116

A.16 Convergence of rotation about the normal along plate boundary
for FEM. Soft simply supported with central point load, $a/b = 1$
and $h = 0.05$ 116

List of Tables

3.1	Hole radius, r , horizontal, P_1 , and vertical pitch, P_2 , for model material, see figure 3.1	30
3.2	Beam dimensions for HMD and LMD test pieces	30
3.3	Beam test geometry and corrected stiffness results, K , for HMD and LMD test pieces	40
3.4	Constitutive properties for HMD slender beams. Flexural modulus E_{fm} , couple modulus γ and characterisic length of bending l_b . .	41
3.5	Constitutive properties for LMD slender beams. Flexural modulus E_{fm} , couple modulus γ and characterisic length of bending l_b . .	41
3.6	Tip displacement for finite element micropolar beam compared against exact analytical solution for an end moment and a point load	44
4.1	Vertex coordinates, in triangular area coordinates, for the inter-connecting control volume (CV) of a six node triangular element shown in figure 4.3	56
4.2	Substitutions for the equilibrium equation integrals and stress displacement relationships	60
4.3	Body and boundary loadings and displacement field solutions for micropolar element patch test.	63

4.4	Vertex coordinates and constitutive properties for micropolar element patch test	63
4.5	Results for displacement and micro rotation at node 2. Stress and couple stress at point P in the patch test mesh under loading cases 1 and 2	64
4.6	Results for displacement and micro rotation at node 2. Stress and couple stress at point P in the patch test mesh under loading case 3. Results shown against exact solution for linear strain control volume CV-MPLST and constant strain control volume CV-MPCST	64
4.7	Stress concentration factors for maximum circumferential stress at circular hole by the constant strain control volume, CV-MPCST, linear strain control volume, CV-MPLST, constant strain finite element, FE-MPCST, and linear strain finite element, FE-MPLST. Hole radius 0.216mm, $G_m = 1.0e9\text{N/m}^2$, $\nu_m = 0.3$ and (A): $\frac{r}{l} = 1.063$ (B): $\frac{r}{l} = 10.63$. Mesh is 8x22x4 elements.	66
4.8	Stress concentration factors for maximum circumferential stress at circular hole by the constant strain control volume, CV-MPCST, linear strain control volume, CV-MPLST, constant strain finite element, FE-MPCST, and linear strain finite element, FE-MPLST. Hole radius 0.864mm, $G_m = 1.0e9\text{N/m}^2$, $\nu_m = 0.3$ and $a = 0.3333$. Mesh is 8x15x4 elements.	67
5.1	Beam test geometry and corrected stiffness results, K , for deep HMD test pieces	74
5.2	Beam test geometry and corrected stiffness results, K , for deep LMD test pieces	75
6.1	Geometric data for ring samples	88
6.2	Experimental stiffness results, K , for ring samples at two aspect ratios; $R/d = 8$ and $R/d = 4$	89

A.1	Substitutions for the discrete equation integrals and moment curvature matrix	105
A.2	Patch test results for a state of pure bending and twist, where w_n is the transverse displacement of node n and M_x , M_y and M_{xy} are the x bending moments, y bending moments and twisting moments respectively. Moments were calculated at the element centroids.	110

List of Symbols

Math Symbols

\square	matrix, row vector
$\{\}$	column vector
δ_{ij}	Kronecker delta
e_{ijk}	permutation tensor

Latin Symbols

a	coupling factor
A	area
b	beam breadth
\mathbf{B}	spatial derivatives of field variables
d	beam depth
\mathbf{d}	nodal displacement vector
D	constitutive property
\mathbf{D}	constitutive property matrix
E	Young's modulus
E_m	micropolar Young's modulus
E_{fm}	micropolar flexural modulus
\mathbf{F}	force resultant
G_m	observed micropolar shear modulus
\mathbf{H}	modified shape function vector

I	second moment of area
\mathbf{k}	element stiffness matrix
K	bending stiffness
\mathbf{K}	global stiffness matrix
l	control volume face length
l_b	characteristic length of bending
l_t	characteristic length of torsion
L	beam length
m_{ij}	couple stress tensor
M	applied bending moment
\mathbf{M}	bending moment vector, couple resultant
n	normal coordinate
n	number of nodes
N	coupling number, shape function
\mathbf{N}	shape function vector
p	body force per unit volume
P_1	horizontal void pitch
P_2	vertical void pitch
\mathbf{P}	applied load vector
q	body couple per unit volume
r	void radius, line coordinate
R	radius of curvature
R^2	coefficient of multiple determination
s	tangent coordinate
SS_{err}	sum of the squared residual errors
SS_{tot}	sum of the squared total errors
T	shear force per unit length
\mathbf{T}	shear force vector
u	displacement in x direction
u_{ij}	displacement vector
v	displacement in y direction
w	displacement in z direction
W	applied load
x	Cartesian coordinate

y	Cartesian coordinate
z	Cartesian coordinate, plate thickness

Greek Symbols

α	micropolar elastic constant
β	micropolar elastic constant
γ	micropolar couple modulus, shear strains
δ	triangular area coordinate
ϵ	direct strains
η	triangular area coordinate
ε_{ij}	strain tensor
θ	macro rotation
κ	micropolar elastic constant
λ	micropolar Lamé's constant
μ	observed shear modulus
μ^*	micropolar shear modulus
ν	Poisson's ratio
ν_m	micropolar Poisson's ratio
ξ	triangular area coordinate
τ_{ij}	force stress tensor
ϕ	micro rotation
χ	curvature vector
Ψ	polar ratio

Abstract

Heterogeneous materials can exhibit behaviour under load that cannot be described by classical continuum elasticity. Beams in bending can show a relative stiffening as the beam depth tends to zero, a size effect. Size effects are recognised in higher order continuum elastic theories such as micropolar elasticity. The drawback of higher order theories is the requirement of additional constitutive relations and associated properties that are often difficult to establish experimentally. Furthermore the finite element method, of great benefit in classical elasticity, has shown limitations when applied to micropolar elasticity. The determination of additional constitutive properties and the numerical modelling of micropolar elasticity is discussed in the context of two model heterogeneous materials.

The first model material was created by drilling holes in an aluminium bar in a regular pattern, with the hole axis normal to the plane of bending. Bending tests show that a size effect is present. These results are compared against a model of the detailed beam geometries in the finite element package ANSYS, which confirms the size effect. Constitutive properties are extracted from the ANSYS results in a new iterative procedure using approximate numerical solutions from a newly developed control volume finite element. This iterative procedure is then used to obtain constitutive properties from the second model material tested as diametrically loaded acrylic rings, with a material size scale equal to a quarter of that of the perforated aluminium beams.

Despite difficulties, associated with the anisotropic nature of the model materials, micropolar elasticity will be shown to be capable of modelling the size effects identified in these model materials.

Chapter 1

Introduction

Considering Scale

It is clear from observing any material that, from a sufficiently far distance, it can appear as of one phase, a homogeneous continuum. On magnifying the material, however, it can be seen that it is in fact made up of a number of phases. This scale effect is dependent upon the material. For example, steel would require to be magnified to a micro metre level to notice the different constituent phases of its microstructure, whereas the microstructure of polymeric foam can be seen with the naked eye. All materials are heterogeneous but it depends upon the scale at which they are observed whether this is significant. As scale has an effect upon what is observed so has it upon the deformation of the material under load. At a macroscopic level steel is classed as being homogenous and thus the deformation can be described by classical continuum elasticity. On a microscopic level, however, the deformation becomes dependent upon the individual responses of the phases and their interactions. In many respects the macroscopic response, characterised by a classical continuum, is an averaging of the microscopic response, but when the overall deformation is occurring on a scale similar to that of the microstructure then a different approach to classical elasticity may be required. This has become an engineering challenge due to the increased use of heterogeneous materials in structural applications [1]. For example, polymeric and metallic foams, particularly as part of sandwich panels, are now being used

more extensively in both automotive and aerospace applications because of the weight saving they afford [1]. It is an active research area to find constitutive models that can describe the elastic response of these materials as they are often endowed with enhanced mechanical behaviour, which are termed size effects [2] due the dependence of this behaviour upon the size of the material domain.

Generalised Elastic Continua

Classical elasticity [3] is a local theory; the forces acting upon an individual point depend only upon its location. Non local theories take note of effects neighbouring that point and how these affect the forces acting upon it. Therefore the deformation of an individual element is now dependant upon its location and neighbourhood. Intrinsic length scales link the two effects. As the problem domain approaches the length scale the non local effect will increase. Conversely as the domain expands away from the length scale the local effects dominate and a local continuum approach is sufficient.

In elasticity non-local effects can be expressed within a continuum by generalised elasticity, or non-local elasticity, of which there are two different classes; higher grade and higher order [2]. Higher grade theories incorporate higher or additional derivatives of the displacement vector whereas higher order theories include additional microstructural degrees of freedom. Couple stress theory [4] is an example of a higher grade theory. An example of a higher order theory is the linear micropolar theory [5]. Linear micropolar theory is endowed with only one additional degree of freedom, a micro rotation, and is therefore the least complex of the higher order theories.

As with many of the generalised elastic theories these two different approaches are linked. If the additional micro rotation of micropolar elasticity is no longer kinematically distinct, equalling the macro rotation, then we have couple stress theory. There are numerous other generalised theories with greater complexity than couple stress or micropolar elasticity. The historical development of generalised theories has been discussed at length in the literature and the reader can be directed to [2,6–8], and references therein for an overview.

This work is concerned with the simplest of the higher order theories, micropolar elasticity. An additional independent micro rotation is present in the formulation, enabling the complimentary shear stress requirement of classical elasticity to be relaxed. Additional couple stresses balance the differential element. The couple stresses have an intrinsic length scale associated with them. Endowed with this additional degree of freedom micropolar elasticity predicts elastic behaviour that is not predicted by classical elasticity. For example the dispersion of stress waves, a dependence of stress concentration factors upon discontinuity size and a size stiffening of smaller samples in bending and torsion are all predicted. The prediction of these additional material behaviours led to research into experimental identification of these size effects and the determination of the additional constitutive properties associated with the theory. To date this has proved to be a challenging task.

1.1 Experimental Methods in Micropolar Elasticity

“...experiments with micropolar constants require much precision and elaborate instrumentation, since we are faced with the measurements of microscopic-level quantities ... At this range, many other physical phenomenon begin to interfere with observation, introducing distortions and errors.” Eringen 1999 [7]

Since the development of non-local theories there have been attempts to identify if the size effects, noted by the theories, exist in real materials. Initial attempts to identify size effects in heterogeneous materials did not prove fruitful [9]. Indeed it is recognised as a difficult task [7], see quote above, as any experiment is trying to identify microscopic level interactions via the macroscopic response of a material under load. Gauthier and Jahsman [10] were the first researchers to separate and devise an experimental procedure to identify all six of the micropolar material constants. Analytical expressions were developed for the mechanical response

in tension, torsion and plate bending. If a micropolar material were tested at reduced sample sizes then the analytic solution predicts that, in torsion and bending, there would be relative stiffening as the sample size reduces. These size effects can be used to determine all of the micropolar material constants [10]. To test this procedure a model material was created where aluminium shot was suspended in an epoxy polymer matrix to 99.5%; it is not stated if this is by volume or weight [9, 10]. The resulting displacement in the torsion case was measured using both holographic interferometry and precision dial gauges. The torsion results proved inconclusive with a large scatter in the data and if any conclusion could be drawn it suggested that a reduction in stiffness was present, not the increase that might have been expected. This was attributed to the friction in the testing equipment and material inhomogeneity. Dynamic tests are a suggested alternative and in a later publication these tests show some presence of micropolar behaviour [10] but are unable to extract all micropolar material properties. Theoretical work conducted by Bigoni [11] may shed some light upon why Gauthier and Jahsman did not find size effects in the model material that was created. Through a homogenisation procedure Bigoni shows that, in a two phase composite, the inclusion must be less stiff than the matrix material before the material will behave in a micropolar manner. This is the opposite of the model material that Gauthier and Jahnsman manufactured. Although no size effects were found using the static test these did form the foundation for future work under the name of “the method of size effects”.

Lakes is the most prolific researcher in the field of experimental determination of micropolar material properties. In his extensive review [12] he makes note of the state of the art, as of fifteen years ago, discussing the merits and drawbacks of various approaches. The salient details mentioned are: the technique that was adopted, in which materials size effects were discovered, whether micropolar elasticity is indeed an adequate model, how the preparation of sample affects size effects and what comment his work has attracted. These will now be discussed.

Lakes advanced Gauthier and Jahsman’s work in the method of size effects by developing a magnetic torque and bending rig that could transmit the required loads without friction. Displacement was measured using a holographic interferometer. Employing both a non contact loading and measurement technique

reduced the parasitic error, due to instrument friction [13]. Analytical solutions for the bending [14] and torsion of circular cylinders were used to identify the micropolar moduli. Although size effects were identified in torsion of polymeric foam, the bending of smaller samples identified a departure from micropolar elasticity. Lakes proposed that this could be due to additional degrees of freedom in the microstructure. Micromorphic elasticity [7], a more generalised microstructure elasticity theory, may have provided a better correlation to the experimental data. In further work [15], size effects are identified in dense polyurethane foam but not in syntactic foams. It is thought that in the syntactic foam the inclusion is stiffer than the matrix. This confirms Bigoni's hypothesis [11] as consequently the material behaves in a nearly classical manner. Micropolar moduli are also identified in compact bone [16]. Comment is passed by Eringen [7] about the measured coupling number being too high which would imply a near zero shear modulus.

Later work by Anderson and Lakes [17], analysing the size effects in closed cell polymethacrylimide, identified that surface damage during sample preparation can cause size softening rather than size stiffening. A surface damage model is incorporated into the analytic solutions for bending and torsion of circular cylinders. Surface damage effects are due to half open voids being present at the boundary of the material. The half open voids are less able to carry the load than the fully enclosed voids. As the size of the boundary increases with respect to the overall cross section of the material it is possible that an anti micropolar effect is present. Careful sample preparation can mitigate this error. There is an apparent trade off between testing a material at smaller sample sizes, where the size effect will be more pronounced and distinguishable from the systematic error of the testing procedure, and testing at such a small scale that the surface damage of the material becomes significant with respect to the overall material response.

Further to the method of size effects and dynamic tests, Lakes presented a field method for qualitatively determining the correct continuum model that the material exhibits. Analysis of the strain field on the surface of a rectangular section under torsion is presented in [18]. It was found that at the edge of the rectangular section the shear stress was non zero, indicating that non classical material

behaviour is present. A screening method using a holographic image to follow the motion of a small edge crack in a rectangular beam under torsion is presented in [19]. A moving crack would be indicative of a micropolar material.

Since the review of Lakes, further work has identified size effects, in the shear modulus and damping of bovine plexiform bone [20], using Lakes torsion technique. Beuchner's work suggests that an understanding of size effects will inform upon the understanding of the scaling laws of bones, identified in larger animals, and geological structures. McFarland [21] returned to Gauthier and Jahsman's work to retrieve the, yet unused, analytical solution for the bending of micropolar plates to identify size effects in micro electro mechanical systems (MEMS). A polypropylene micro cantilever beam, end loaded by a nanoindenter, showed a size stiffening up to four times greater than that predicted by classical beam theory. This work only allowed the determination of the characteristic length of bending but this is sufficient to gain a displacement field for a slender micropolar beam.

As can be seen size effects have been identified in a wide variety of materials including micro mechanical beams, biomaterials and polymeric foams, which have impact upon many fields of engineering. An adequate approach is therefore required to both determine the constitutive properties of heterogeneous materials and apply them to the analysis of these materials in engineering design.

1.2 Numerical Methods in Micropolar Elasticity

"...bring the topic of microelastic continua from one of abstraction to that of reality..." Goldberg 1974 [22]

The finite element method (FEM), of great popularity in the field of computational structural mechanics, was first turned to micropolar elasticity by Baluch,

Goldberg and Koh [23]. They formulated a bi-linear triangular element with linear displacement and linear micro rotation fields. Although no numerical results are presented they note that their purpose is to bring micropolar elasticity and its associated micro continuum models from “one of abstraction to that of reality”. The nature of micro continuum theories is complex and therefore very few analytical solutions exist. Goldberg [22], in a later work states that the finite element method is used “in order to alleviate the inherent complexity” involved in solving the system of governing equations. His later work presents an FEM for the bending of micropolar plates using a 3 noded triangular element with 15 degrees of freedom; transverse displacement, rotation and micro rotation.

Nakamura, Benedict and Lakes [24] present another bi-linear triangular element for orthotropic micropolar elasticity. Results are shown for the estimation of stress concentration factors of a circular hole in an infinite plate, for which an analytical solution exists. The model is capable of identifying the size effect, although there is an error in the computed value that appears to be dependent upon the coupling number; the larger the value of the coupling number, which is a constitutive property governing the antisymmetry of the shear stresses in micropolar elasticity, the greater the error. This issue is identified in other works [25,26]. In a later work Nakamura and Lakes [27] present a finite element analysis package called MIRACS (Micro rotation and couple stress) which is used to investigate Saint-Venant end effects in micropolar elastic materials. A 3 node constant strain triangular element, a 4 node isoparametric element and an 8 node isoparametric element make up the package. Further plane elements have been published [25, 28–30]. The quadratic element of Providas and Kattis [25] is the most accurate plane finite element to date. In [25], a patch test is presented to better assess the published element. Wheel [26] departs from the standard finite element procedure to publish a constant strain planar control volume method. This method shows enhanced performance in the patch test of Providas and Kattis; returning the exact stress states for each test, which the finite element formulations were unable to.

The first three dimensional element to be developed was by Huang et al [31]; a Wilson’s non-compatibility brick element with 6 nodal degrees of freedom and 8 nodes. An interesting investigation of the role of various constitutive prop-

erties upon the computed displacement to the exact solution of a beam with a non kinematically distinct micro rotation, i.e. couple stress beam, is presented. Large errors are reported for certain material properties used. There appears to be no discussion as to whether the author believes that this is due to numerical inaccuracy in the finite element solution or if it is not converging to the solution because the FEM is displaying behaviour that the beam solution is unable to display due to its couple stress assumptions. Their results show that as κ , a micropolar elastic constant, increases then the solution will converge to the analytical, couple stress solution. In the definition of the coupling number, N , as κ tends to infinity, N tends to 1. If $N = 1$ the shear stresses are fully antisymmetric and thus the problem is that of couple stress theory; hence the convergence to the exact solution. Branke et. al. [32] presents a three dimensional element for micropolar elasticity, with the couple stress assumption. It is used to simulate four point bending of a textile-reinforced composite and material parameters are determined by homogenisation. Numerical homogenisation of material properties offers an alternative to physical experiments [33, 34].

Goldberg's work was presented to motivate the use of the FEM in the engineering analysis of materials with a microstructure but identified a debate about the correct use of constitutive properties which experiments can shed light upon. Indeed these conclusions are the same today. There is still discussion in the literature about the correct constitutive properties to use and most presented work to date has yet to find a useful application where experiments and numerical work tie up to showcase a useful analysis technique for materials with micro structure. It is the aim of this work to strive towards this goal.

1.3 Research Aims

Size effects have been identified previously in real materials but is micropolar elasticity really an adequate model to quantify this? Previous work has shown that it is difficult to distinguish size effects from experimental errors. In addition to this bespoke testing equipment is often required. To date no work has conducted the experimental determination of constitutive properties and the development of

numerical models to assist in this. Both these aspects are essential if micropolar elasticity is to be used in computational engineering analysis and design. What is discussed in this work is a designed model heterogeneous material that will be examined to see if micropolar elasticity can describe its deformation. In addition numerical techniques will be developed that will be used to assess if micropolar elasticity can be used as an appropriate analysis tool and, for the first time, used in the identification of the constitutive properties. This will be the first comparison between a real material, experimentally tested to determine the constitutive properties, and a numerical solution to micropolar elastic problems.

Due to the inherent complexity of heterogeneous materials and micropolar elasticity only one and two dimensional problems are considered. There is, however, much to be considered in these cases that will impact upon any future work moving into full three dimensional representations. Beginning with the general linear theory of micropolar elasticity, this will be reduced in complexity to look at first the bending of slender micropolar beams and secondly the bending of deep micropolar beams. Solutions to these problems, by analytical and numerical methods, are compared against experimental responses of a model material under three point bending at various spans using the method of size effects. In addition to the method of size effects, limited by available analytical solutions, it is proposed that advances in the computational modelling of micropolar materials can bring about an inverse method for identifying the constitutive properties. This utilises a newly developed linear strain micropolar control volume element which iteratively finds the correct constitutive properties from experimental testing data. Further to this, the new iterative search procedure will be used to fit constitutive properties to the, experimentally determined, stiffness of diametrically loaded heterogeneous rings. These rings are made of a different model material.

This thesis sets out the mathematics of linear micropolar elasticity and the progression to plane stress and plane strain problems, followed by the formulation for a slender micropolar beam and a thin walled micropolar ring. With the solution of a slender beam in place, the creation of the model material and its testing as a slender beam will be discussed. After this, a return will be made to the plane stress and plane strain formulations when a linear strain micropolar

control volume finite element will be formulated. This will then be used in the analysis of deep beams, based upon the constitutive properties gained from the slender beams, and used to identify a further constitutive property. Finally, to prove the method assembled in the analysis of thick beams, micropolar constitutive properties from diametrically loaded ring samples will be determined. This work therefore shows a useful application of micropolar elasticity as an analysis tool to predict the deformations of heterogeneous materials in bending.

Chapter 2

Micropolar Elasticity

Micropolar elasticity is one of the higher order non-local theories of Eringen [7]. It is endowed with an additional micro rotation vector that removes the restriction upon classical elasticity that the shear stresses are symmetric. It is a general model and will converge to both classical elasticity and couple stress theory. The three dimensional stress tensors of linear micropolar elasticity are introduced and the constitutive properties are discussed. Following this, and reducing the complexity, four special cases of linear micropolar elasticity are considered; the two dimensional formulations of plane stress and plane strain, the one dimensional formulation for a slender beam and the one dimensional formulation for a thin walled ring, these being the focus of the research in this thesis.

2.1 Generalised Linear Micropolar Elasticity

Linear micropolar elasticity takes into account the deformation of the microstructure by introducing a length scale dependent couple stress, m , and an additional degree of freedom, the micro rotation ϕ . For a linear elastic isotropic micropolar material the force stress tensor, τ_{ij} , and couple stress tensor, m_{ij} , respectively are [5],

$$\tau_{ij} = \lambda \varepsilon_{kk} \delta_{ij} + (2\mu^* + \kappa) \varepsilon_{ij} + \kappa e_{ijk} (\theta_k - \phi_k) \quad (2.1)$$

$$m_{ij} = \alpha \phi_{k,k} \delta_{ij} + \beta \phi_{i,j} + \gamma \phi_{j,i} \quad (2.2)$$

The repeated indices denote summation over the range $(i, j, k = 1, 2, 3)$, δ_{ij} is the Kronecker delta and e_{ijk} is the permutation tensor. These are defined in the following way:

$$\delta_{ij} = \begin{cases} 1, & \text{if } i = j \\ 0, & \text{if } i \neq j \end{cases} \quad (2.3)$$

$$e_{ijk} = \begin{cases} +1, & \text{if } ijk \text{ is an even permutation of } (1, 2, 3) \\ -1, & \text{if } ijk \text{ is an odd permutation of } (1, 2, 3) \\ 0, & \text{otherwise} \end{cases} \quad (2.4)$$

An index followed by a comma represents a partial differentiation with respect to the coordinate system. τ is the force stress tensor, m is the couple stress tensor, θ is the macro rotation, ϕ is the micro rotation and $\lambda, \mu_m, \kappa, \alpha, \beta, \gamma$ are six elastic constants. μ^* is the micropolar shear modulus. This is related to the observed shear modulus μ by,

$$\mu = \mu^* + \frac{\kappa}{2} \quad (2.5)$$

The macro rotation and strain tensor respectively are,

$$\theta_i = \frac{1}{2} e_{ijk} u_{k,j} \quad (2.6)$$

$$\varepsilon_{ij} = \frac{1}{2} (u_{i,j} + u_{j,i}) \quad (2.7)$$

where u is the displacement vector. The six elastic constants can be expressed in terms of seven engineering constants [12]:

$$E_m = \frac{(2\mu^* + \kappa)(3\lambda + 2\mu^* + \kappa)}{(2\lambda + 2\mu^* + \kappa)} \quad (2.8)$$

$$G_m = \mu^* + \frac{\kappa}{2} \quad (2.9)$$

$$\nu_m = \frac{\lambda}{(2\lambda + 2\mu^* + \kappa)} \quad (2.10)$$

$$l_t^2 = \frac{(\beta + \gamma)}{(2\mu^* + \kappa)} \quad (2.11)$$

$$l_b^2 = \frac{\gamma}{2(2\mu^* + \kappa)} \quad (2.12)$$

$$N^2 = \frac{\kappa}{2(\mu^* + \kappa)} \quad (2.13)$$

$$\Psi = \frac{(\beta + \gamma)}{(\alpha + \beta + \gamma)} \quad (2.14)$$

where E_m is the micropolar Young's modulus, G_m the observed micropolar shear modulus, ν_m the micropolar Poisson's ratio, l_t the characteristic length of torsion, l_b the characteristic length of bending, N the coupling number and Ψ the polar ratio. The micropolar equivalents of the classic elastic constants inform the behaviour in much the same way as in the classical theory. The characteristic lengths of torsion and bending dictate the length scale of the size effects. The coupling number controls the antisymmetry of the shear stresses. The polar ratio is equivalent to Poisson's ratio but with respect to the micro rotation. The micropolar theory contains two limits. If α, β, γ and κ are set to zero, the solid will behave in a classical manner. Alternatively if the coupling number N is set to 1 then the material will behave as in couple stress theory, where the micro rotation is no longer kinematically distinct from the macro rotation.

2.2 Two Dimensional Formulations

Reducing the complexity of the general form of linear micropolar elasticity produces two dimensional formulations for plane stress and plane strain [27]. The static equilibrium equations for the balance of stress and couple stress, see figure 2.1, are respectively;

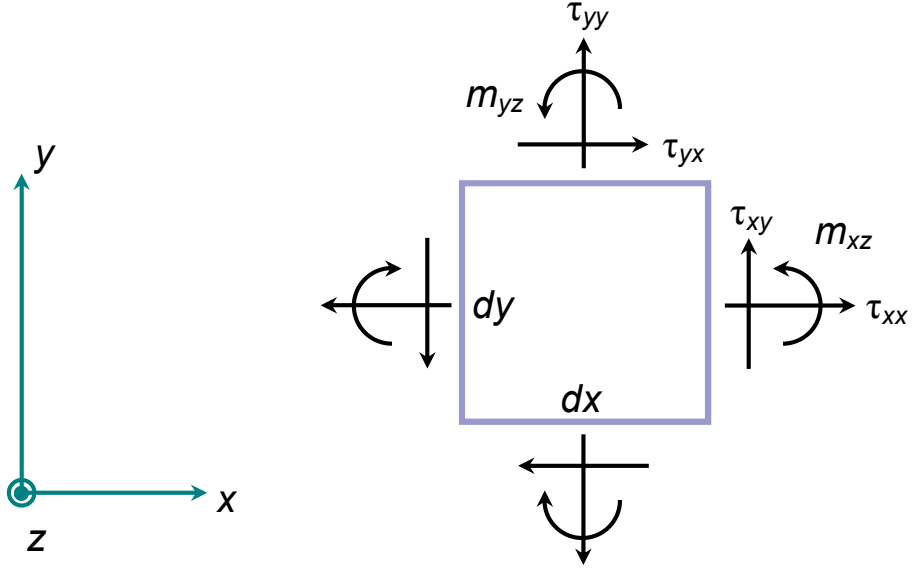


Figure 2.1: *Micropolar differential stress element*

$$\tau_{ij,i} + p_j = 0 \quad (2.15)$$

$$m_{i3,i} + e_{ij3}\tau_{ij} + q_3 = 0 \quad (2.16)$$

where the repeated indices denote summation over the range $(i, j = 1, 2)$. p_j are body forces per unit volume and q_3 represents a body couple per unit volume. Expanding the equilibrium equations for Cartesian coordinates, $(i, j = x, y)$ and setting the free index 3 to z gives;

$$\tau_{xx,x} + \tau_{yx,y} + p_x = 0 \quad (2.17)$$

$$\tau_{yy,y} + \tau_{xy,x} + p_y = 0 \quad (2.18)$$

$$m_{xz,x} + m_{yz,y} + \tau_{xy} - \tau_{yx} + q_z = 0 \quad (2.19)$$

The linear constitutive equations can be expressed as,

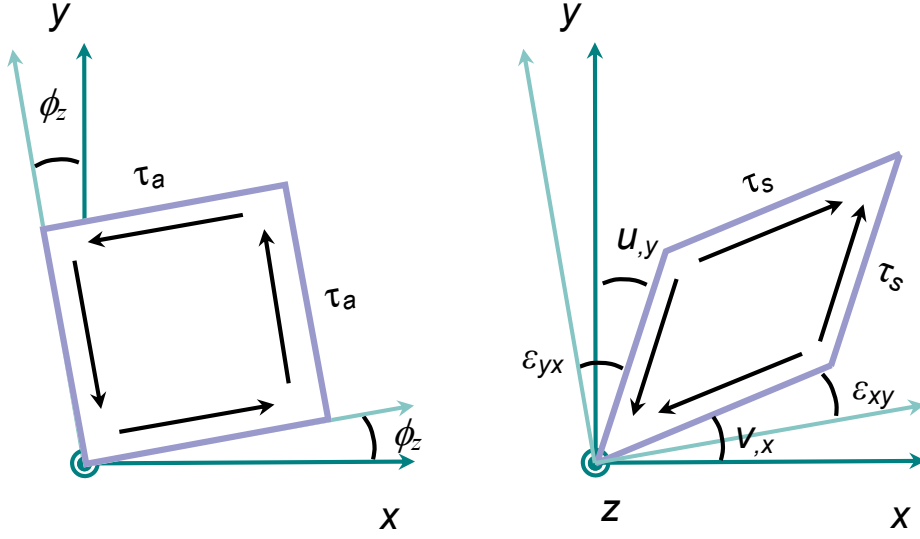


Figure 2.2: Deformation of stress element due to antisymmetric, τ_a , and symmetric, τ_s , shear stresses

$$\tau_{ij} = \lambda \varepsilon_{kk} \delta_{ij} + (\mu^* + \kappa) \varepsilon_{ij} + \mu^* \varepsilon_{ji} \quad (2.20)$$

$$m_{ij} = \alpha \phi_{k,k} \delta_{ij} + \beta \phi_{i,j} + \gamma \phi_{j,i} \quad (2.21)$$

where the repeated indices denote summation over the range $(i, j, k = 1, 2, 3)$. Introducing a modified strain displacement relationship where,

$$\varepsilon_{ij} = u_{i,j} + e_{ijk} \phi_k \quad (2.22)$$

which expanded for Cartesian coordinates $(i, j, k = x, y, z)$ gives,

$$\begin{bmatrix} \varepsilon_{xx} \\ \varepsilon_{yy} \\ \varepsilon_{yx} \\ \varepsilon_{xy} \end{bmatrix} = \begin{bmatrix} u_{,x} \\ v_{,y} \\ u_{,y} + \phi_z \\ v_{,x} - \phi_z \end{bmatrix} \quad (2.23)$$

where u and v are the displacement components of the x and y directions respectively. The displacement gradients $u_{,y}$, $v_{,x}$ are associated with the symmetric

component of the shear stresses, τ_s , while the micro rotation ϕ_z is due to the antisymmetric component of the shear stresses, τ_a , see figure 2.2. The constitutive equations are now modified to account for the specific assumptions present in both the plane stress and plane strain theory.

2.2.1 Plane Strain

In plane strain it is assumed that the z component of strain is zero as in the classical case. In addition for micropolar elasticity the micro rotation is assumed to be zero about the x and y directions. Therefore $\varepsilon_{zz} = \varepsilon_{xz} = \varepsilon_{yz} = \varepsilon_{zx} = \varepsilon_{zy} = 0$ and $\phi_x = \phi_y = 0$. This gives rise to the modified constitutive equations, expressed in expanded matrix form in the Cartesian coordinates for force stress,

$$\begin{bmatrix} \tau_{xx} \\ \tau_{yy} \\ \tau_{yx} \\ \tau_{xy} \end{bmatrix} = \begin{bmatrix} \lambda + 2\mu^* + \kappa & \lambda & 0 & 0 \\ \lambda & \lambda + 2\mu^* + \kappa & 0 & 0 \\ 0 & 0 & \mu^* + \kappa & \mu^* \\ 0 & 0 & \mu^* & \mu^* + \kappa \end{bmatrix} \begin{bmatrix} \varepsilon_{xx} \\ \varepsilon_{yy} \\ \varepsilon_{yx} \\ \varepsilon_{xy} \end{bmatrix} \quad (2.24)$$

and couple stress,

$$\begin{bmatrix} m_{xz} \\ m_{yz} \end{bmatrix} = \begin{bmatrix} \gamma & 0 \\ 0 & \gamma \end{bmatrix} \begin{bmatrix} \phi_{z,x} \\ \phi_{z,y} \end{bmatrix} \quad (2.25)$$

These can be reformulated in term of the engineering material constants E_m , ν_m , l_b and N from equations (2.8),(2.10),(2.12) and (2.13) respectively as,

$$\begin{bmatrix} \tau_{xx} \\ \tau_{yy} \\ \tau_{yx} \\ \tau_{xy} \end{bmatrix} = \frac{E_m}{(1 + \nu_m)} \begin{bmatrix} \frac{(1-\nu_m)}{(1-2\nu_m)} & \frac{\nu_m}{(1-2\nu_m)} & 0 & 0 \\ \frac{\nu_m}{(1-2\nu_m)} & \frac{(1-\nu_m)}{(1-2\nu_m)} & 0 & 0 \\ 0 & 0 & \frac{1}{2(1-N^2)} & \frac{(1-2N^2)}{2(1-N^2)} \\ 0 & 0 & \frac{(1-2N^2)}{2(1-N^2)} & \frac{1}{2(1-N^2)} \end{bmatrix} \begin{bmatrix} \varepsilon_{xx} \\ \varepsilon_{yy} \\ \varepsilon_{yx} \\ \varepsilon_{xy} \end{bmatrix} \quad (2.26)$$

$$\begin{bmatrix} m_{xz} \\ m_{yz} \end{bmatrix} = \begin{bmatrix} \frac{2E_m l_b^2}{(1+\nu_m)} & 0 \\ 0 & \frac{2E_m l_b^2}{(1+\nu_m)} \end{bmatrix} \begin{bmatrix} \phi_{z,x} \\ \phi_{z,y} \end{bmatrix} \quad (2.27)$$

An alternative relationship between the shear stresses and the shear strains can be formulated by introducing a new constitutive parameter, the coupling factor, a , where,

$$N^2 = \frac{a}{1+a} \quad (2.28)$$

Then expressing the shear modulus G_m as

$$G_m = \frac{E_m}{2(1+\nu_m)} \quad (2.29)$$

allows the shear stresses to be related to the shear strains in the simpler form,

$$\begin{bmatrix} \tau_{yx} \\ \tau_{xy} \end{bmatrix} = G_m \begin{bmatrix} 1+a & 1-a \\ 1-a & 1+a \end{bmatrix} \begin{bmatrix} \varepsilon_{yx} \\ \varepsilon_{xy} \end{bmatrix} \quad (2.30)$$

2.2.2 Plane Stress

In plane stress theory it is assumed that the stress in the z direction is zero and again it is assumed that the micro rotations about the x and y axes are zero. Therefore $\tau_{zz} = \tau_{xz} = \tau_{yz} = \tau_{zx} = \tau_{zy} = 0$ and $\phi_x = \phi_y = 0$. As the assumptions with respect to the couple stress are unchanged between plane stress and plane strain the constitutive relationships are unchanged from equations (2.25) and (2.27). However the modified force stress constitutive relationships are,

$$\begin{bmatrix} \tau_{xx} \\ \tau_{yy} \\ \tau_{yx} \\ \tau_{xy} \end{bmatrix} = \begin{bmatrix} \frac{(2\mu^*+\kappa)(2\lambda+2\mu^*+\kappa)}{\lambda+2\mu^*+\kappa} & \frac{\lambda(2\mu^*+\kappa)}{\lambda+2\mu^*+\kappa} & 0 & 0 \\ \frac{\lambda(2\mu^*+\kappa)}{\lambda+2\mu^*+\kappa} & \frac{(2\mu^*+\kappa)(2\lambda+2\mu^*+\kappa)}{\lambda+2\mu^*+\kappa} & 0 & 0 \\ 0 & 0 & \mu^* + \kappa & \mu^* \\ 0 & 0 & \mu^* & \mu^* + \kappa \end{bmatrix} \begin{bmatrix} \varepsilon_{xx} \\ \varepsilon_{yy} \\ \varepsilon_{yx} \\ \varepsilon_{xy} \end{bmatrix} \quad (2.31)$$

and again expressed in terms of the engineering constants,

$$\begin{bmatrix} \tau_{xx} \\ \tau_{yy} \\ \tau_{yx} \\ \tau_{xy} \end{bmatrix} = \frac{E_m}{(1 - \nu_m^2)} \begin{bmatrix} 1 & \nu_m & 0 & 0 \\ \nu_m & 1 & 0 & 0 \\ 0 & 0 & \frac{(1-\nu_m)}{2(1-N^2)} & \frac{(1-\nu_m)(1-2N^2)}{2(1-N^2)} \\ 0 & 0 & \frac{(1-\nu_m)(1-2N^2)}{2(1-N^2)} & \frac{(1-\nu_m)}{2(1-N^2)} \end{bmatrix} \begin{bmatrix} \varepsilon_{xx} \\ \varepsilon_{yy} \\ \varepsilon_{yx} \\ \varepsilon_{xy} \end{bmatrix} \quad (2.32)$$

2.3 One Dimensional Formulations

In generalised linear micropolar elasticity the micro rotation is kinematically distinct from the macro rotation but a simplification can be made for slender beams and rings where the micro rotation equals the macro rotation [35]. This special case is often referred to as couple stress theory in the literature.

2.3.1 Slender Beam

The derivation for the moment curvature relationships for a slender micropolar beam and the maximum vertical displacement under three point bending follows. The radius of curvature, R , of a beam under pure bending, being bent through a small angle is,

$$\frac{1}{R} = \frac{d\theta}{dx} = \frac{d\phi_z}{dx} = -\frac{d^2v}{dx^2} \quad (2.33)$$

Considering only the in plane couple stress, m_{xz} and direct stress τ_{xx}

$$m_{xz} = \gamma \frac{d\phi_z}{dx} \quad (2.34)$$

$$\tau_{xx} = \frac{E_{fm}y}{R} \quad (2.35)$$

where E_{fm} is a micropolar flexural modulus. Taking the internal resisting moment equal to any externally applied moment, M , see figure 2.3,

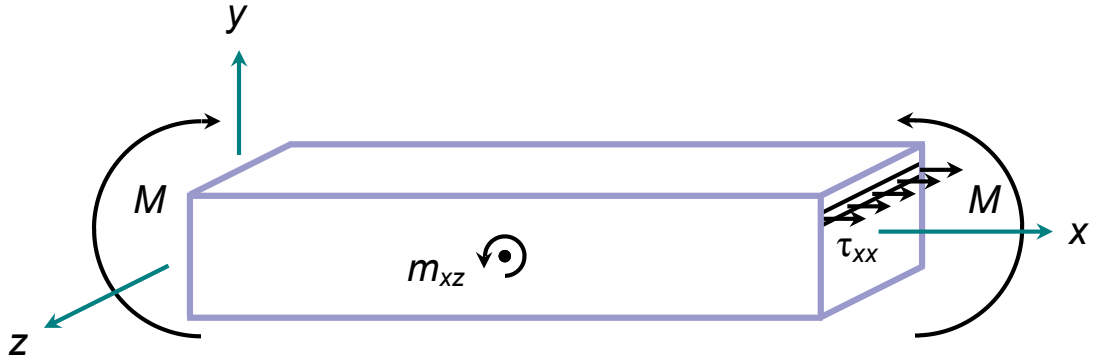


Figure 2.3: *Stress acting upon a one dimensional micropolar beam*

$$M = \int_A (y\tau_{xx} + m_{xz})dA \quad (2.36)$$

Substituting for

$$m_{xz} = \frac{\gamma}{R} \quad (2.37)$$

and

$$\tau_{xx} = \frac{E_{fm}y}{R} \quad (2.38)$$

,

$$M = \frac{1}{R} \int_A (y^2 E_{fm} + \gamma) dA \quad (2.39)$$

Completing the integration where the second moment of area, I is,

$$I = \int_A y^2 dA \quad (2.40)$$

and area, A is

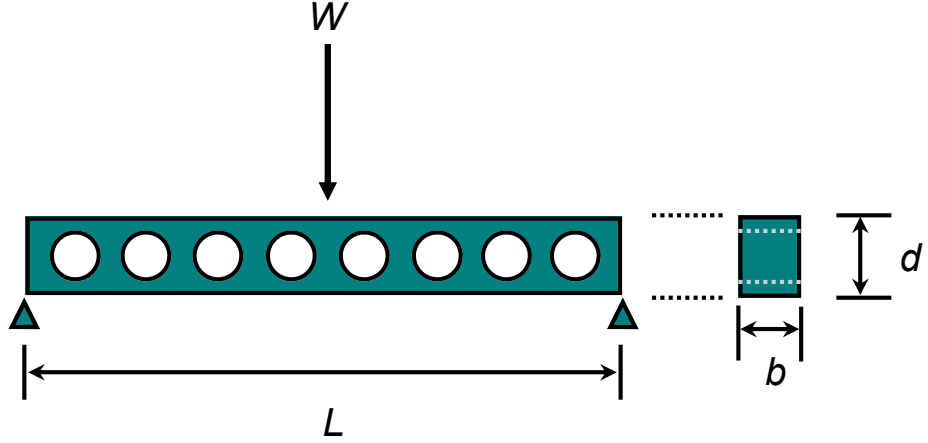


Figure 2.4: Model beam subjected to three point bending

$$A = \int_A dA \quad (2.41)$$

and substituting for

$$\frac{1}{R} = -\frac{d^2v}{dx^2} \quad (2.42)$$

the moment curvature relationship is,

$$\frac{d^2v}{dx^2} = -\frac{M}{E_{fm}I + \gamma A} \quad (2.43)$$

From the moment curvature relationship the maximum displacement, v_{max} for a micropolar beam under three point bending, figure 2.4, is,

$$v_{max} = \frac{WL^3}{48(E_{fm}I + \gamma A)} \quad (2.44)$$

where W is the central applied load, L is the length of the beam, E_{fm} is the micropolar flexural modulus, I is the second moment of area, γ is a length scale dependent micropolar constant and A is the cross-sectional area. This can be

rearranged to express the stiffness, K in terms of the beam depth d , where the stiffness is the applied load W divided by the maximum displacement v_{max} .

For a rectangular cross section, the substitutions for the second moment of area, I , and area, A , are,

$$I = \frac{bd^3}{12} \quad (2.45)$$

$$A = bd \quad (2.46)$$

where b is the breadth and d is the depth. The stiffness K is,

$$K = 4E_{fm}b \left(\frac{d}{L} \right)^3 \left(1 + \left[\frac{l_b}{d} \right]^2 \right) \quad (2.47)$$

where l_b (m) is the characteristic length in bending for a rectangular cross section,

$$l_b = \sqrt{\frac{12\gamma}{E_{fm}}} \quad (2.48)$$

For a classically elastic beam the equation for determining the maximum deflection of a beam under three point bending loading is

$$v_{max} = \frac{WL^3}{48E_{fm}I} \quad (2.49)$$

therefore the stiffness is

$$K = 4E_{fm}b \left(\frac{d}{L} \right)^3 \quad (2.50)$$

From this, it can be seen that in equation (2.47) the expression outside the bracket is that of the classical beam equation and inside is the term associated with the micropolar stiffening. It can also be seen that as the depth of the beam increases the significance of the characteristic length reduces and the solution converges to the equation for a classically elastic beam.

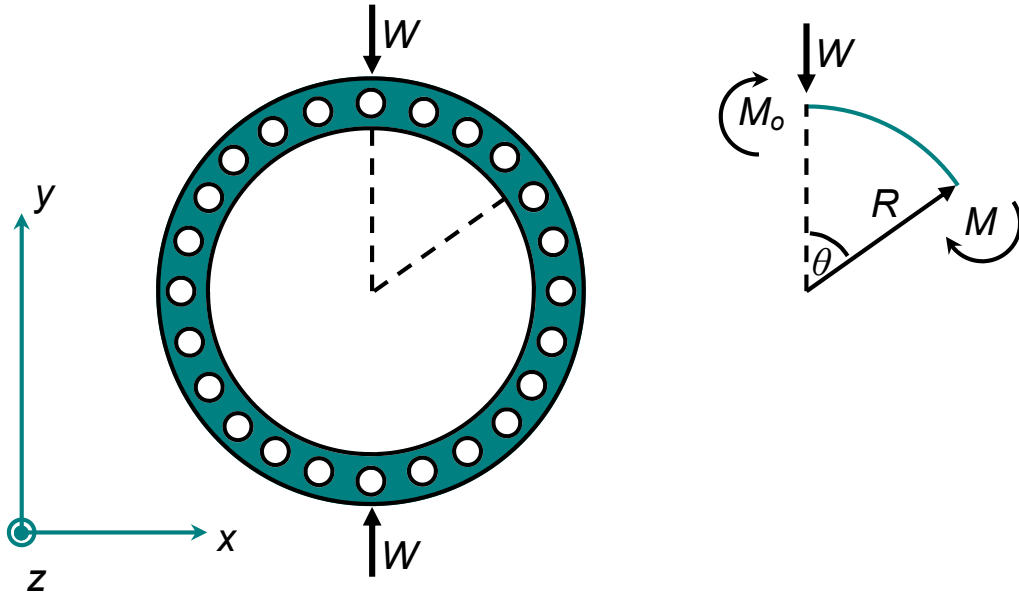


Figure 2.5: Model ring subject to diametrically opposing point loads

2.3.2 Thin Walled Ring

The derivation for the vertical displacement in a thin walled ring with diametrically opposing point loads follows. The derivation will differ from that of the slender beam and begins by defining the elastic strain energy, U , in the thin micropolar ring of radius, R , as

$$U = \frac{1}{2} \int_0^{\pi/2} \frac{M^2}{(E_{fm}I + \gamma A)} R d\theta \quad (2.51)$$

This equation is a modification of the strain energy function derived in [35] and the other symbols have the same meaning as in the slender beam derivation. Summing the moments about a cut made at angle θ away from the applied load W , see figure 2.5, gives the total moment as

$$M = WR \sin \theta - M_o \quad (2.52)$$

From Castigliano's theorem the vertical displacement, v , at the load point can

be gained from,

$$v = \frac{\partial U}{\partial W} = \frac{1}{(E_{fm}I + \gamma A)} \int_0^{\frac{\pi}{2}} M \frac{\partial M}{\partial W} R d\theta \quad (2.53)$$

Making substitutions for M, equation 2.52, and

$$\frac{\partial M}{\partial W} = R \sin \theta \quad (2.54)$$

The vertical displacement can be expressed as

$$v = \frac{R^2}{(E_{fm}I + \gamma A)} \left(\frac{\pi}{4} WR - M_o \right) \quad (2.55)$$

To find the unknown resultant moment M_o , the macro rotation m_o of the ring is derived, again by Castigliano's theorem, as

$$m_o = \frac{\partial U}{\partial M_o} = \frac{1}{(E_{fm}I + \gamma A)} \int_0^{\frac{\pi}{2}} M \frac{\partial M}{\partial M_o} R d\theta \quad (2.56)$$

Again making the substitution for M and letting

$$\frac{\partial M}{\partial M_o} = -1 \quad (2.57)$$

The macro rotation is

$$m_o = \frac{R}{(E_{fm}I + \gamma A)} \left(-WR + \frac{\pi}{2} M_o \right) \quad (2.58)$$

Assuming that there is no macro rotation, owing to symmetry where the load is applied then

$$M_o = \frac{2}{\pi} WR \quad (2.59)$$

Making the substitution for M_o into equation 2.55 gives the vertical displacement at the load point as

$$v = \frac{WR^3}{(E_{fm}I + \gamma A)} \left(\frac{\pi^2 - 8}{4\pi} \right) \quad (2.60)$$

This equation can be rearranged to gain an expression for the stiffness K of the thin walled ring

$$K = \frac{\pi E_{fm} b}{3(\pi^2 - 8)} \left(\frac{d}{R} \right)^3 \left(1 + \left[\frac{l_b}{d} \right]^2 \right) \quad (2.61)$$

where b is the breadth of the ring, d is the depth of the ring wall and l_b is the characteristic length in bending as defined in equation 2.48. Similar to the slender beam formulation, the stiffness of a classically elastic thin walled ring is outside the brackets of equation 2.61 and the bracketed term governs the length scale dependent component of the stiffness.

2.4 Conclusion

In this chapter the constitutive, equilibrium and kinematic equations of the general linear theory of micropolar elasticity have been laid out. This was followed by the presentation of plane stress and strain micropolar elasticity which will be used in chapter 4 to derive a linear strain control volume finite element for micropolar elasticity. Further to this two, one dimensional derivations were presented. The first was for determining the stiffness of slender micropolar beams, loaded in three point bending. This will be used in the next chapter to assess if a model heterogeneous material is displaying a size dependent stiffening consistent with micropolar elasticity. Further to this it will be used in chapter 5 to aid in the determination of the micropolar plane stress constitutive properties from experimental data gained from three point bending of heterogeneous beams of different aspect ratios. Finally using the approach set out in chapter 5 the second one di-

mensional derivation, that of a thin walled ring, will be used to obtain micropolar plane stress constitutive properties from rings of different aspect ratios.

Chapter 3

Model Material - Slender Beam

With the mathematical approach set out in the previous chapter for the deformation of a slender micropolar beam, a heterogeneous material that exhibits a size effect in bending is required. This will enable constitutive properties to be determined, using the method of size effects, and the deformation predicted by numerical procedure. In an attempt to avoid experimental difficulties associated with real heterogeneous materials an idealised model material, that is designed to mitigate errors and produce a noticeable size effect, is required.

Three factors, that will inform upon the design of the model material, have been identified in the literature. The first is the stiffness of the inclusions in the matrix material. Previous experimental work with a model material had used inclusions that were stiffer than the matrix material [10], and found no conclusive size effect. Recent theoretical work, however, on homogenisation procedures in micropolar elasticity has identified that the inclusion needs to be less stiff than the matrix material [11], and relatively dilute within the matrix. Therefore a material with compliant inclusions is sought. The second is the size of the inclusions with respect to the overall test sample size. If the inclusions are too small then any micropolar material response will be masked by systemic errors inherent in the test procedure [12]. If the inclusions, however, are too large, in comparison to the overall sample size, then local loading effects may become significant. The material would be better modelled as a classical continuum with all the discrete

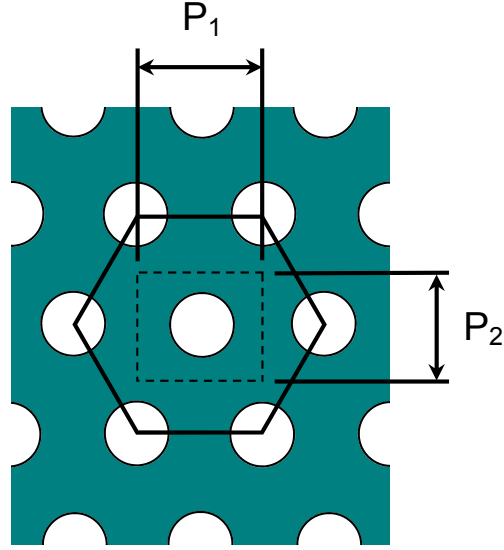


Figure 3.1: *Diagram of hole pitch with horizontal pitch P_1 and vertical pitch P_2*

detail present, as a micropolar continuum assumption would break down. The third issue is sample preparation [17], mitigating any potential anti size effect. This can be achieved by having minimal surface damage around the boundary of the test sample, ideally with no broken voids on the boundary.

In addition to these desirable material attributes a suitable testing procedure is also required. As stated above, systematic errors in the testing procedure can mask any size effect. In previous work low friction force application and non contact measurement techniques have been employed to mitigate this. It was, however, a desire of this work to use standard materials testing equipment to allow easy reproduction of these tests in the future.

The model material was chosen to be an aluminium matrix with circular voids. The aluminium was alloy 6082 T6 with an elastic modulus of 70GPa. Standard aluminium bar stock of sizes 12.7, 25.4, 38.1 and 50.8 mm depth and a common breadth of 12.7 mm was used. Holes were drilled through the breadth in a regular hexagonal pattern. The void pattern is designed in such a way that no voids intersect the boundary of the top and bottom edges of the bar. Two pitch sizes were made to experimentally determine how this might influence the size effect

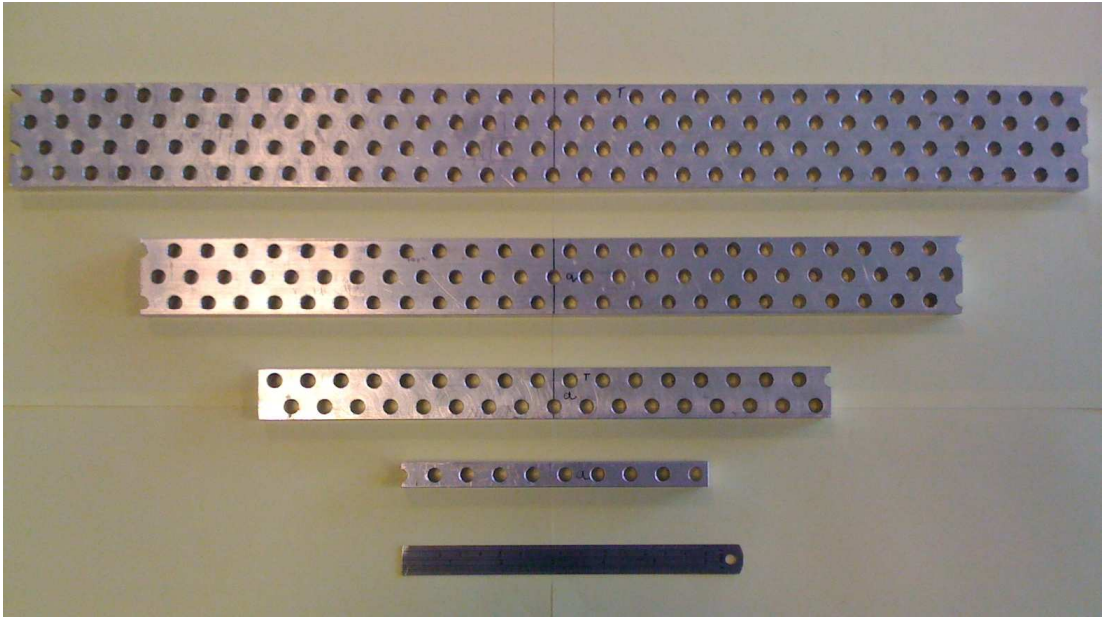


Figure 3.2: *Photograph of HMD test pieces*

in bending. A lower mass density (LMD) and higher mass density (HMD) set of sample were made by maintaining the same void radius and vertical packing while the horizontal pitch was altered. Figure 3.1 shows the void pitch measurements and table 3.1 gives dimensions for the sizes of the void pitches. This model material is anisotropic due to the hexagonal packing and different horizontal and vertical pitches. The length of the test samples were such that they could be tested at an aspect ratio of approximately 10:1, (length:depth). This allows a slender beam assumption to be made, meaning that the dominant mode of deformations is due to bending and any shear deformation is minimised. A size effect in bending can be identified by varying the depth of a beam while maintaining the same aspect ratio of length relative to depth. If the beams were behaving in a classical manner then the stiffness of the sample should remain constant. For a micropolar material, however, the stiffness should increase with a reduction in depth. This is demonstrated mathematically in section 2.3.1. To this end test pieces of four different depths were manufactured for each density, dimensions of which can be seen in table 3.2. The four HMD test pieces can be seen in figure 3.2.

Table 3.1: Hole radius, r , horizontal, P_1 , and vertical pitch, P_2 , for model material, see figure 3.1

Beam	$r(\text{mm})$	$P_1(\text{mm})$	$P_2(\text{mm})$
HMD	3.5	16	12.7
LMD	3.5	9	12.7

Table 3.2: Beam dimensions for HMD and LMD test pieces

Beam	Breadth(mm)	Depth(mm)	Length(mm)
B1	12.7	12.7	150
B2	12.7	25.4	280
B3	12.7	38.1	400
B4	12.7	50.8	530

3.1 Experimental Procedure

The test pieces were loaded in three point bending in a Zwick 2061 materials testing machine with a 50kN load cell. The advantage of testing in three point bending is that, when loaded, the two supports at either end of the beam are driven by the testing rig cross head. This means that the maximum displacement, which will be at the supports, as the central point remains fixed, can easily be obtained from the crosshead displacement output. Testing in a cantilever configuration would have also given the same displacement output, however, it is difficult to enforce the built in boundary condition experimentally.

In each case, the aspect ratio remained constant for each depth tested. The support points were located horizontally midway between adjacent voids. This restriction on load positioning resulted in the LMD and HMD tests being carried out at slightly different aspect ratios. The stiffness of the sample was determined by incrementally loading the sample in the linear elastic region and recording the cross head displacement and applied load, see figure 3.3 (a) for a photograph of the experimental setup. The tensile testing machine output an ASCII data file which was imported into Microsoft Excel where a plot of load against crosshead displacement was made. In some tests the data was cropped to remove any non-linearity that was associated with the initial load being taken up by the beam.

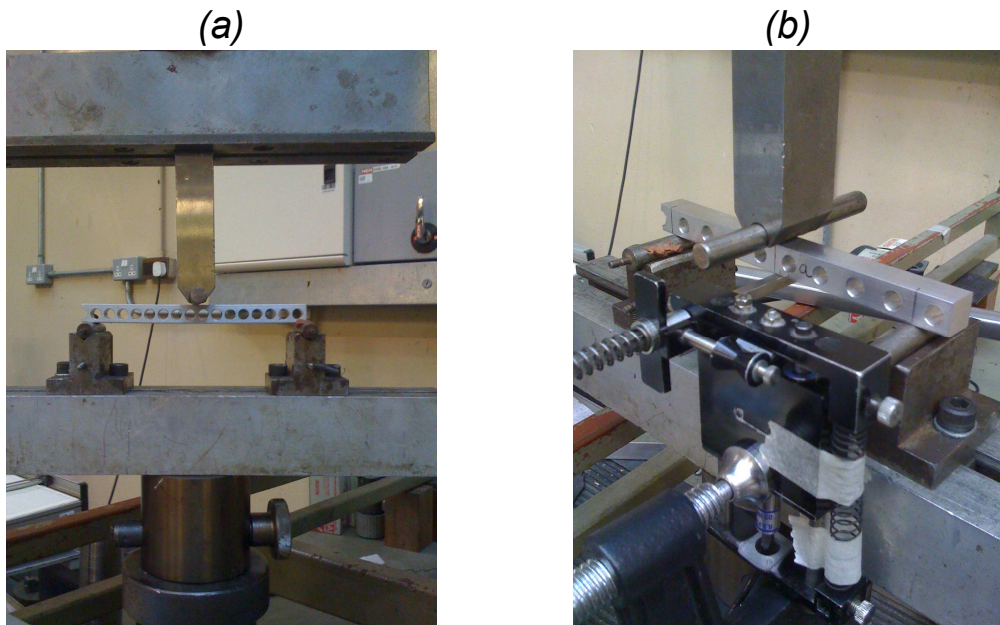


Figure 3.3: (a) *LMD_B1* in three point bending with cross head measurement only (b) *HMD_B1* in three point bending with independent central deflection reading from extensometer

The stiffness was calculated by fitting a straight line to the resulting linear load displacement curve; the gradient of that line yielding the stiffness, see figure 3.4. This was repeated for a second set of test pieces and the results presented are an average of the stiffness values obtained.

To complement this experimental work, a finite element analysis of each test was performed using models capturing all the geometric details of the samples; details of which can be seen in section 3.2. A comparison of the measured and predicted stiffnesses found that they did not initially agree so the experiments were repeated using an independent reading of the central deflection of the test sample using an extensometer clamped to the test rig, see figure 3.3 (b). While this improved the measured results they were still in error with those obtained by FEA. Again the test pieces were loaded, however, this time the deflection of the supports was also measured. For the larger test sample the support base flexed quite considerably causing the supports to displace vertically. Therefore two deformations were taking place during the loading. The first was the bending of the test pieces and secondly the flexure of the support base, see figure 3.5. When

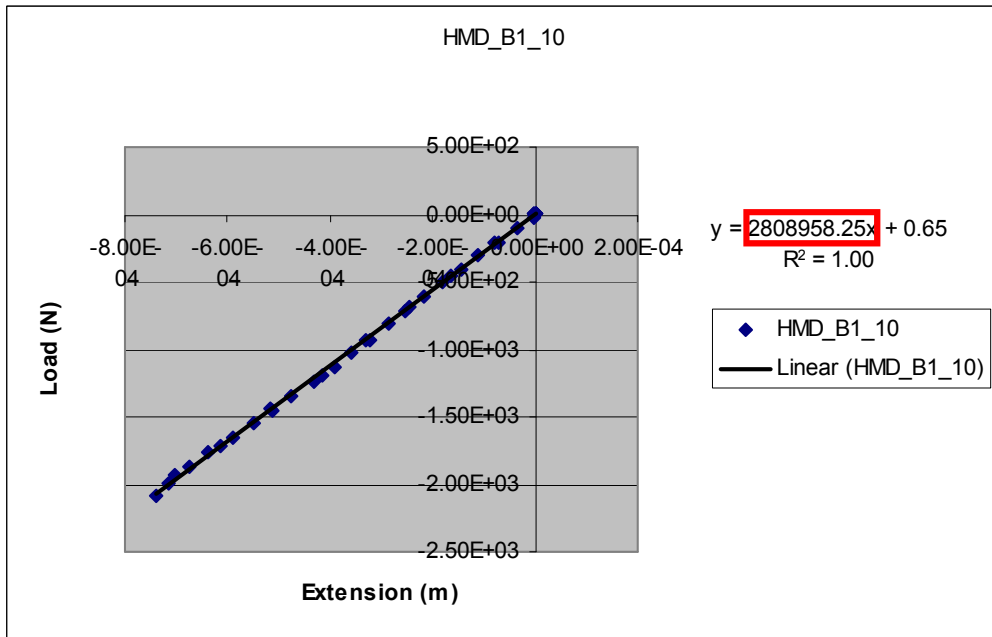


Figure 3.4: Test data plot from Microsoft Excel showing load displacement curve for HMD_B1_10 with fitted straight line and equation of straight line shown with gradient highlighted in box

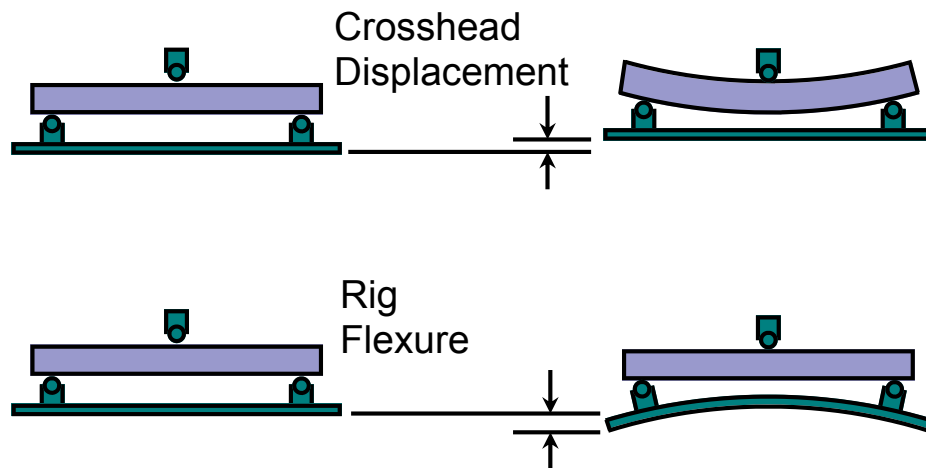


Figure 3.5: Diagram showing relative crosshead and rig flexure displacements for three point bending experimental procedure

the rig flexed the cross head would displace without any corresponding bending of the beam therefore this vertical displacement requires to be subtracted in order to get a true reading of the central deflection of the beam. If this subtraction is not performed this leads to an underestimation of the stiffness, particularly at larger spans where the flexure is greater. This is evident in the results. Once this vertical displacement was subtracted from the central deflection of the test sample then the measured stiffness values were in good agreement with those of the finite element analysis. The corrected and uncorrected results can be seen in figures 3.6 and 3.7 for slender HMD and LMD beams respectively.

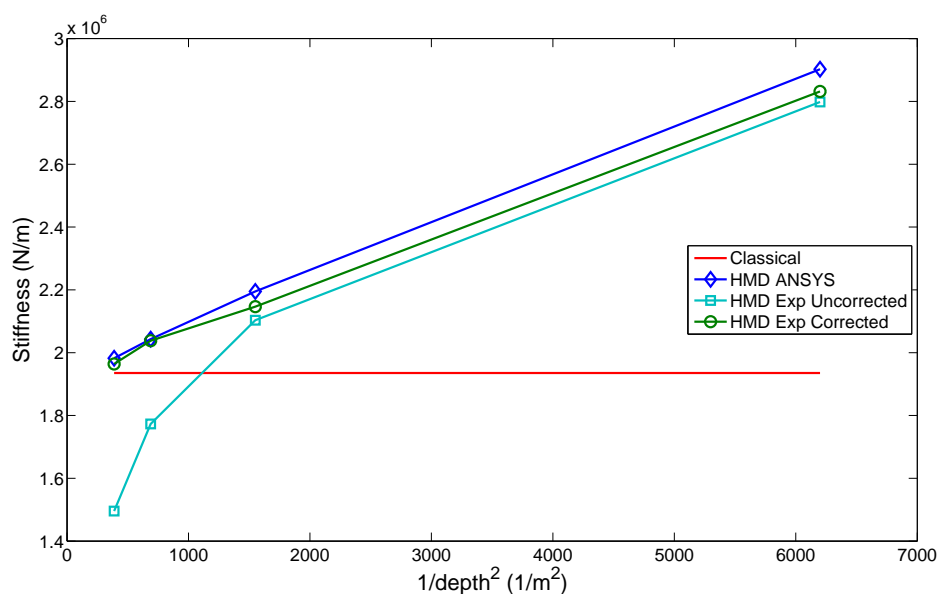


Figure 3.6: *Stiffness against $1/\text{depth}^2$ for HMD beams at $L/d = 10.08$. Comparing discrete detail ANSYS, experimental results and experimental results corrected for test rig flexure against classical solution*

3.2 Detailed Finite Element Analysis

The complementary finite element analysis was carried out in the commercial package ANSYS [36]. The definition of the beam geometry follows the sequence of steps set out in the flow diagram of figure 3.8 and the input files for each

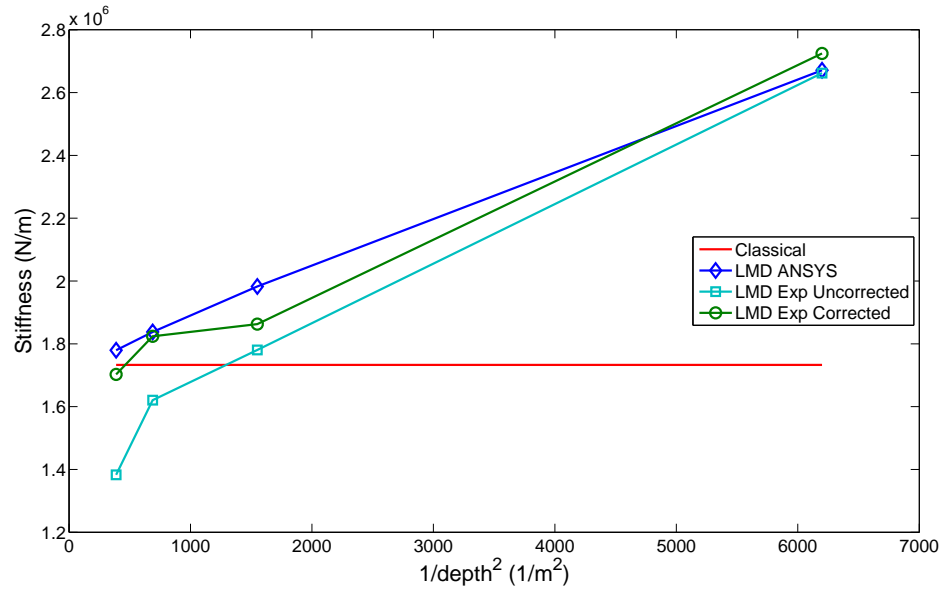


Figure 3.7: *Stiffness against $1/\text{depth}^2$ for LMD beams at $L/d = 9.92$. Comparing discrete detail ANSYS, experimental results and experimental results corrected for test rig flexure against classical solution*

geometry can be seen in appendix D. To begin with, the vertical and horizontal void pitches and the void radius were defined as parametric inputs. Next, using these parameters, an area bounded by half the horizontal and vertical pitches with a quarter void at one corner was created. This area was then meshed and reflected about the x and y axis in order to make a unit cell; an area bounded by the horizontal and vertical pitch with the circular void at the centre. Finally the unit cell was duplicated and arrayed to form the complete beam geometry. A schematic representation of this can be seen in figure 3.9. The process to create the complete beam geometry was automated by the `AGEN` command of ANSYS ADPL within a `DO` loop. Using this approach created duplicate keypoints and nodes that were coincident but unconnected. These had to be merged first before the loads and boundary conditions were applied.

It must be noted that although a line of symmetry exists, at the mid point of a beam under three point bending, it was decided to model the full beam geometry to avoid errors, if any, that could arise in prescribing a symmetry boundary condition through the voids. Modelling the full geometry did not increase the

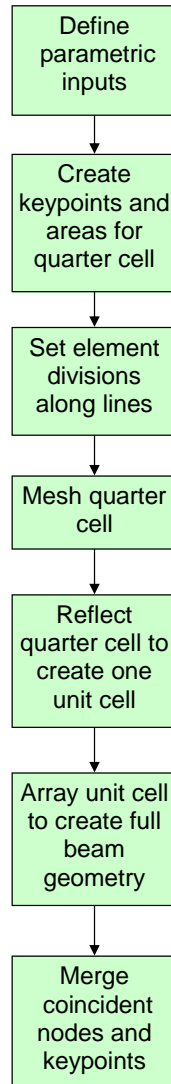


Figure 3.8: *Flow chart showing the sequence of steps used to create the detailed finite element beam geometry*

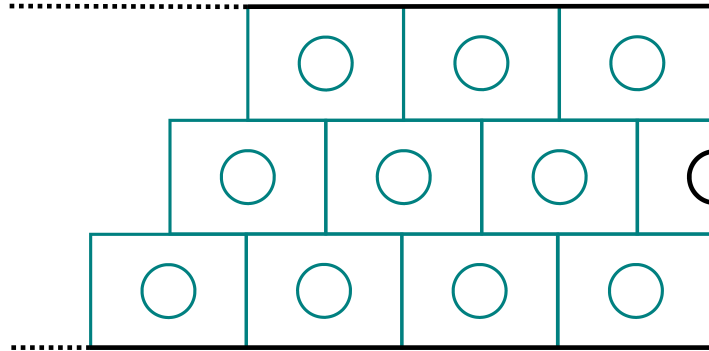


Figure 3.9: *Array of unit cells and half unit cells to create detailed beam geometry*

computation time to an inconvenient level.

With the geometry defined the nodal displacement boundary conditions were applied, to represent the supports, with the left end node constrained in both the horizontal and vertical directions and the right end node constrained only in the vertical direction. The load was applied as a point nodal load on the top edge of the beam at mid span. A value of stiffness from the beam analysis was gained by taking an average of the vertical displacement of the nodes at the mid span and dividing by the applied load.

Looking more closely at the mesh, different mesh distributions are required for the HMD and LMD test pieces. This is due the different pitch sizes. In order to check that the model was converging to a solution, as the number of nodes was increased, a parameter was introduced into the input file to refine the mesh parametrically. This parameter is termed “**refine**” in the input files and dictates the relative number of element divisions along the lines defining the perimeter of the quarter cell. Convergence of the central displacement upon mesh refinement for the HMD and LMD sample of one unit cell depth is shown in figures 3.10 and 3.11 respectively. Both figures contain a comparison between a four node quadrilateral element in plane stress, ANSYS element 182, and an eight node quadrilateral element in plane stress, ANSYS element 183. It can be seen that element 183 has superior convergence and therefore it is selected and a refinement

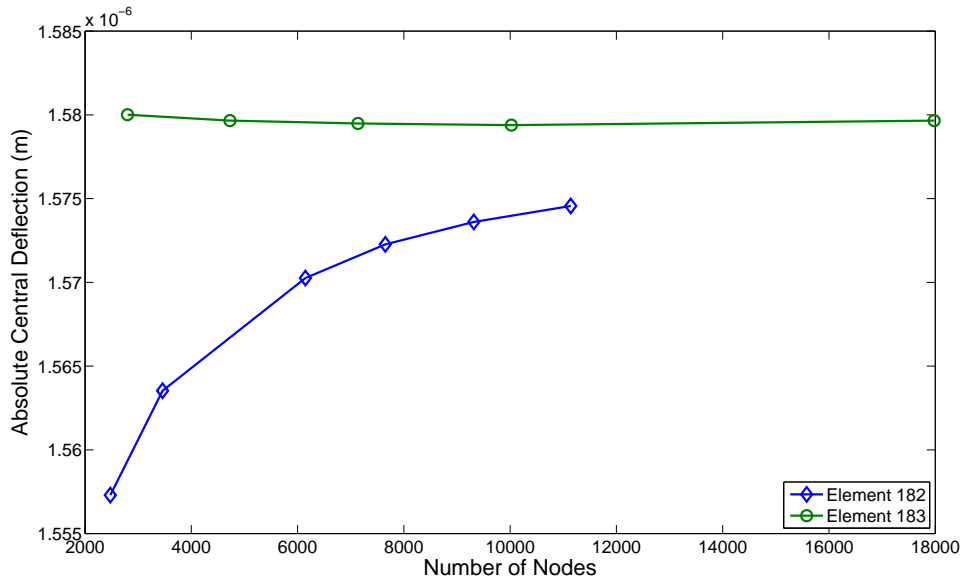


Figure 3.10: Convergence of absolute central deflection against number of nodes for HMD_B1_10 geometry, comparing ANSYS elements 182 and 183

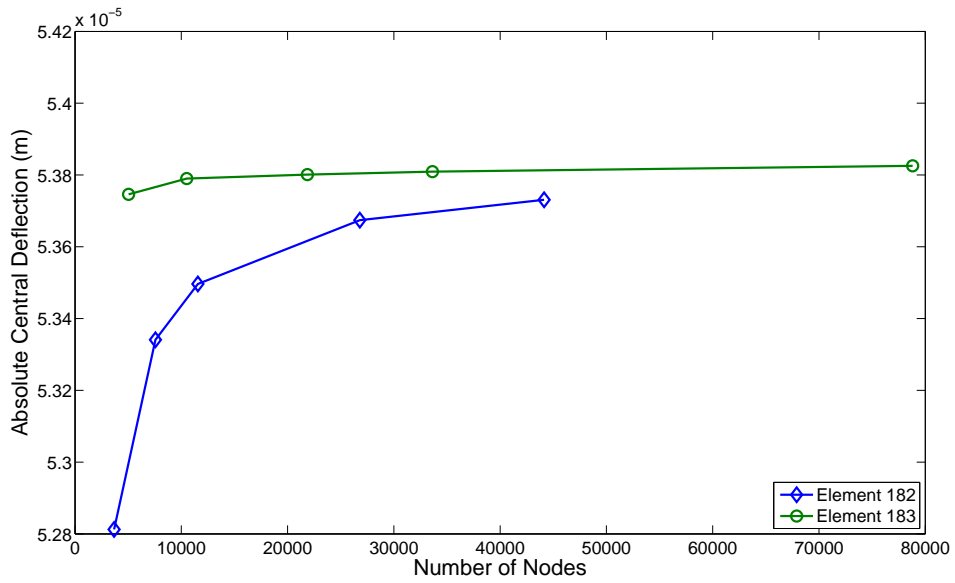


Figure 3.11: Convergence of absolute central deflection against number of nodes for LMD_B1_10 geometry, comparing ANSYS elements 182 and 183

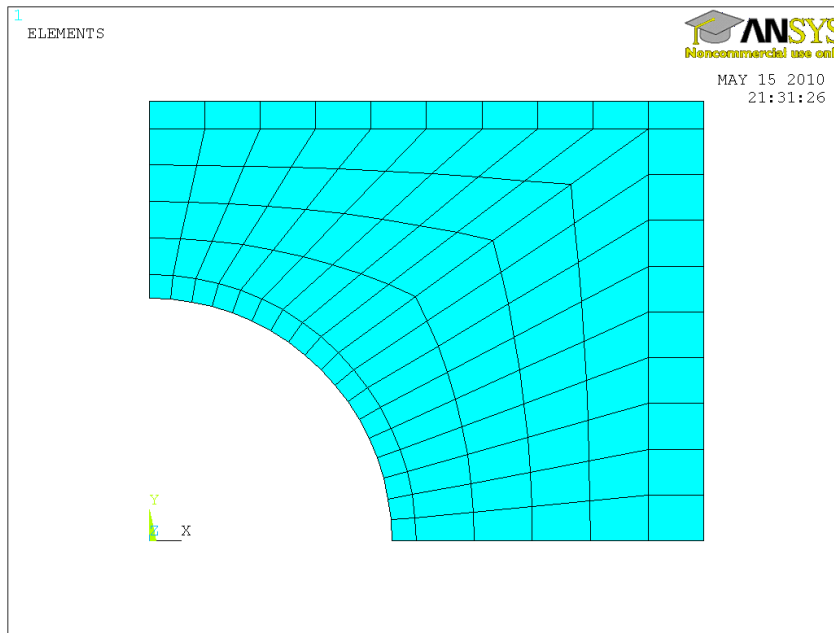


Figure 3.12: Quarter mesh for HMD discrete detail finite element model. Mesh refinement parameter *refine*= 1, 378 nodes

factor of *refine*= 1 (7136 total nodes or 378 nodes per quarter cell) and *refine*= 0.5 (10512 total nodes or 62 nodes per quarter cell) is selected for the HMD and LMD models respectively. The large difference in the number of nodes per quarter mesh between the HMD and LMD models is due to an attempt to keep the global number of nodes similar. The LMD model, however, has a greater number of global nodes to ensure that there is the same number of nodes vertically through the centre of the unit cell as the HMD model. This was to ensure that the same number of vertical nodes in both the HMD and LMD models described the stress variation in the vertical direction as this would be of greater significance, than that in the horizontal, for bending problems. The meshes of the quarter unit cells can be seen in figure 3.12 for the HMD model and figure 3.13 for the LMD model

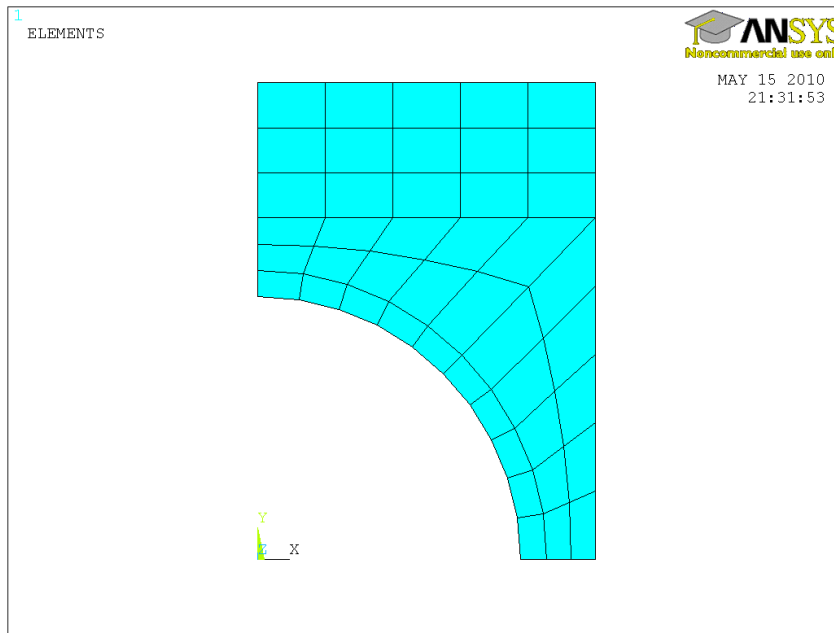


Figure 3.13: Quarter mesh used in LMD discrete detail finite element model. Mesh refinement parameter *refine*= 0.5, 62 nodes

3.3 Results

The experimental and detailed finite element results, for the HMD beams, can be seen in figure 3.6 and table 3.3 and, for the LMD beams, in figure 3.7 and table 3.3. The tabulated results show the corrected experimental stiffness values. Agreement between the HMD corrected experimental results and the HMD ANSYS results are good although with a slight departure for the shallower beams, approx 2.4%. The significant correction that occurs when the flexure of the supports is removed can be seen for the beams with greater depth. The correlation is much the same for the LMD beams, however, a larger mismatch for the B.2 beam sample with a 6.4% departure is noted. Although there is scatter present in the experimental results it is clear that there is size dependent stiffening for this model material.

From the observed size dependent stiffening, micropolar constitutive properties have been determined. Fitting a straight line to the data allows the micropolar

Table 3.3: *Beam test geometry and corrected stiffness results, K , for HMD and LMD test pieces*

Beam	Depth (mm)	Length (mm)	L/d	K_{Exp} (N/m)	K_{ANSYS} (N/m)
HMD_B1_10	12.7	128	10.08	2.832e6	2.903e6
HMD_B2_10	25.4	256	10.08	2.147e6	2.195e6
HMD_B3_10	38.1	384	10.08	2.038e6	2.043e6
HMD_B4_10	50.8	512	10.08	1.964e6	1.982e6

Beam	Depth (mm)	Length (mm)	L/d	K_{Exp} (N/m)	K_{ANSYS} (N/m)
LMD_B1_10	12.7	126	9.92	2.725e6	2.671e6
LMD_B2_10	25.4	252	9.92	1.863e6	1.983e6
LMD_B3_10	38.1	378	9.92	1.824e6	1.838e6
LMD_B4_10	50.8	504	9.92	1.702e6	1.780e6

Table 3.4: *Constitutive properties for HMD slender beams. Flexural modulus E_{fm} , couple modulus γ and characterisitc length of bending l_b*

	E_m (N/m ²)	γ (N)	l_b (mm)
EXP	3.871e10	2.469e5	8.75
ANSYS	3.900e10	2.629e5	8.99

Table 3.5: *Constitutive properties for LMD slender beams. Flexural modulus E_{fm} , couple modulus γ and characterisitc length of bending l_b*

	E_m (N/m ²)	γ (N)	l_b (mm)
EXP	3.148e10	2.745e5	10.23
ANSYS	3.310e10	2.416e5	9.36

flexural modulus, E_{fm} , and characteristic length of bending, l_b , to be found. Rearranging equation 2.47 in the form

$$K = \left(4l_b^2 E_{fm} b \left(\frac{d}{L} \right)^3 \right) \left[\left(\frac{1}{d} \right)^2 \right] + 4E_{fm} b \left(\frac{d}{L} \right)^3 \quad (3.1)$$

enables E_{fm} to be determined from the intercept and l_b from the gradient when the sample stiffness is plotted as a function of the reciprocal of the beam depth squared, $\left(\frac{1}{d^2} \right)$, as in figure 3.6. The constitutive properties are shown in tables 3.4 and 3.5.

It has been proposed that the characteristic length should be of the same order as the microstructure [12] and it is promising that, for the model materials, both HMD and LMD, the characteristic length is of the same order as the microstructure. There is an increase in the characteristic length from the HMD to LMD samples, by 4% in the ANSYS and 17% in the experimental. The vertical pitch and radius remains constant between the two samples, however the horizontal pitch is smaller for the LMD sample thus increasing the scale of the heterogeneity with respect to the beam length. This would suggest that the characteristic length should increase, which is seen. The flexural modulus reduces between HMD and LMD by 15% in the ANSYS and 19% in the experimental. This is expected as there is 18.5% less matrix material between the HMD and LMD

sample.

The flexural modulus values obtained from the bending tests are compared against Young's modulus values obtained from simulated tensile tests carried out in ANSYS. Due to the anisotropic nature of the model material the Young's modulus was calculated in two orthogonal directions corresponding to the transverse and longitudinal directions of the beams. The Young's modulus converged, on increasing numbers of unit cells, for the HMD material to $4.05e10$ N/m² and $4.20e10$ N/m² in the transverse and longitudinal directions respectively. For the LMD material the orthogonal Young's moduli were $2.64e10$ N/m² and $3.58e10$ N/m² in the transverse and longitudinal directions respectively. Comparing these moduli with those from the bending test it is encouraging to note that the flexural modulus is similar to the along length modulus. This is expected as the modulus along the length would be the modulus that would be expected to have the greatest role in beam bending, particularly at a slender aspect ratio. In both cases the error is similar, approximately an 8% difference. This simple test of the Young's modulus in orthogonal directions highlights the level of anisotropy in each model material with the greatest variation in the LMD materials. This will be shown to be significant in later chapters.

With a method for determining the micropolar material properties, flexural modulus, E_{fm} , and characteristic length of bending, l_b , in place a micropolar slender beam finite element formulation was embarked upon to enable the future modelling of complex lattice structures and space frames comprised of slender beams.

3.4 One Dimensional Beam Finite Element

A four degree of freedom, 2 noded, straight beam element is set up, see figure 3.14 , in a similar manner to a standard Euler beam element [37]. The degrees of freedom are the transverse displacement, v , and rotation, θ , at each node. The rotation is assumed to remain small therefore $\theta \approx \frac{dv}{dx}$. The four degrees of freedom \mathbf{d} are interpolated along the beam with cubic shape functions \mathbf{N} to gain

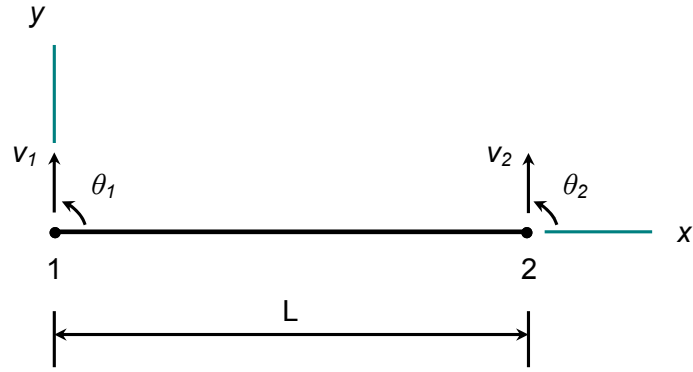


Figure 3.14: *Beam element*

the transverse displacement.

$$v = [\mathbf{N}] \{\mathbf{d}\} \quad (3.2)$$

Expanded;

$$v = \left[\left(1 - \frac{3x^2}{L^2} + \frac{2x^3}{L^3}\right) \quad \left(x - \frac{2x^2}{L^2} + \frac{x^3}{L^3}\right) \quad \left(\frac{3x^2}{L^2} - \frac{2x^3}{L^3}\right) \quad \left(\frac{2x^2}{L^2} - \frac{x^3}{L^3}\right) \right] \begin{bmatrix} v_1 \\ \theta_1 \\ v_2 \\ \theta_2 \end{bmatrix} \quad (3.3)$$

The curvature of the beam element is $v_{,xx} = [\mathbf{B}] \{\mathbf{d}\}$, where

$$\mathbf{B} = \frac{d^2}{dx^2} \mathbf{N} = \left[\left(-\frac{6}{L^2} + \frac{12x}{L^3}\right) \quad \left(-\frac{4}{L} + \frac{6x}{L^2}\right) \quad \left(\frac{6}{L^2} - \frac{12x}{L^3}\right) \quad \left(-\frac{2}{L} + \frac{6x}{L^2}\right) \right] \quad (3.4)$$

The element stiffness matrix is expressed in the form,

$$\mathbf{k} = \int_0^L \mathbf{B}^T (E_{fm}I + \gamma A) \mathbf{B} dx \quad (3.5)$$

Table 3.6: *Tip displacement for finite element micropolar beam compared against exact analytical solution for an end moment and a point load*

	$v_{FE}^{\frac{d}{l_b}=1}$ (m)	$v_{exact}^{\frac{d}{l_b}=1}$ (m)	$v_{FE}^{\frac{d}{l_b}=25}$ (m)	$v_{exact}^{\frac{d}{l_b}=25}$ (m)
End Moment	0.00003	0.00003	5.99042e-05	5.99042e-05
Point Load	0.00002	0.00002	3.99361e-05	3.99361e-05

$$\mathbf{k} = \frac{E_{fm}I + \gamma A}{L^3} \begin{bmatrix} 12 & 6L & -12 & 6L \\ 6L & 4L^2 & -6L & 2L^2 \\ -12 & -6L & 12 & -6L \\ 6L & 2L^2 & -6L & 4L^2 \end{bmatrix} \quad (3.6)$$

where E_{fm} is the micropolar flexural modulus, I is the second moment of area, γ is the couple stress modulus, A is the cross sectional area and L is the length of the beam element. The global stiffness matrix is assembled and solved in the standard finite element manner,

$$[\mathbf{K}] \{\mathbf{d}\} = \{\mathbf{P}\} \quad (3.7)$$

where $\{\mathbf{P}\}$ is the vector of externally applied forces and moments.

3.4.1 Validation

A cantilever beam of length, $L = 1\text{m}$, depth, $d = 0.1\text{m}$ and breadth, $b = 0.1\text{m}$ was loaded by an end moment of 100Nm , an end point load of 100N and a uniformly distributed load of 100N/m consecutively. For the material properties, the micropolar flexural modulus, E_{fm} , was 100GPa , while two ratios of depth to characteristic length of bending d/l_b were chosen, $d/l_b = 1$ and 25 . The tip displacement was compared against that of the slender micropolar beam theory derived in section 2.3.1. For the end moment and point load cases the tip displacement is predicted exactly by one element and is insensitive to the value of characteristic length, shown in table 3.6. For a uniformly distributed load the transverse displacement is no longer fully described by the element shape functions therefore the convergence to the exact solution of the tip displacement, with

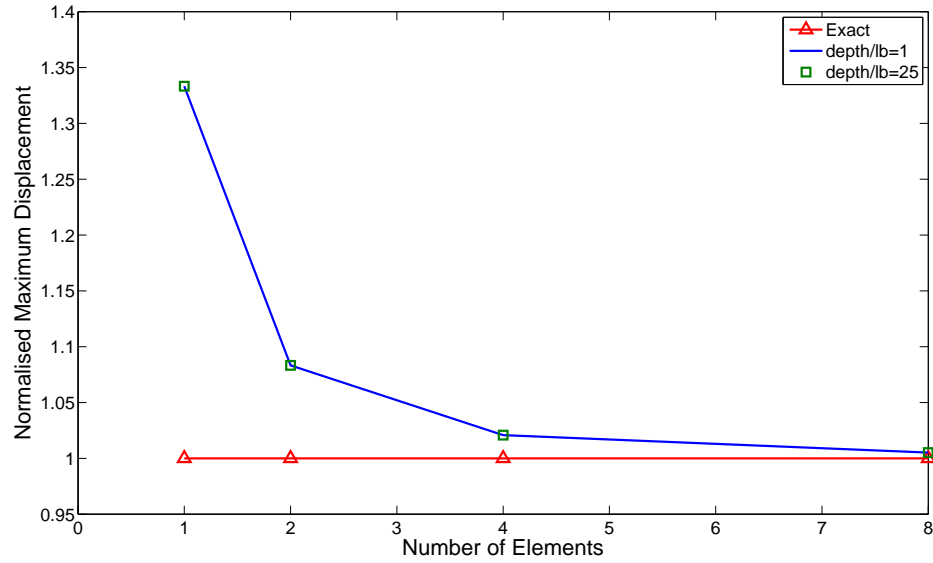


Figure 3.15: *Tip displacement convergence to couple stress beam theory for cantilever beam at various depth to characteristic length ratios*

increasing number of elements, can be checked. The convergence is shown in figure 3.15. It can be seen that convergence to the analytical solution is achieved to within 0.5% for 8 elements and the convergence is unaffected by the d/l_b ratio.

3.4.2 Slender Beam Comparison

Using the material properties determined from the slender beam sample of the model material, it is possible to replicate the size stiffening, shown by the model material beams. This can be seen in figure 3.16, from the experimental data, and figure 3.17, from the detailed ANSYS model. As expected, it has replicated the size stiffening faithfully. This set of results, provided by the new beam finite element, is obtained in a reduced computation time when compared against the detailed finite element. When the time taken to input the detailed geometry is considered along side the computation time, then the time savings that could be achieved, if a micropolar continuum is chosen as the modelling route, rather than a classical continuum is quite considerable. To highlight this a computation time comparison was carried out on a PC with an Intel[®] Atom[™] N270 1.60GHz

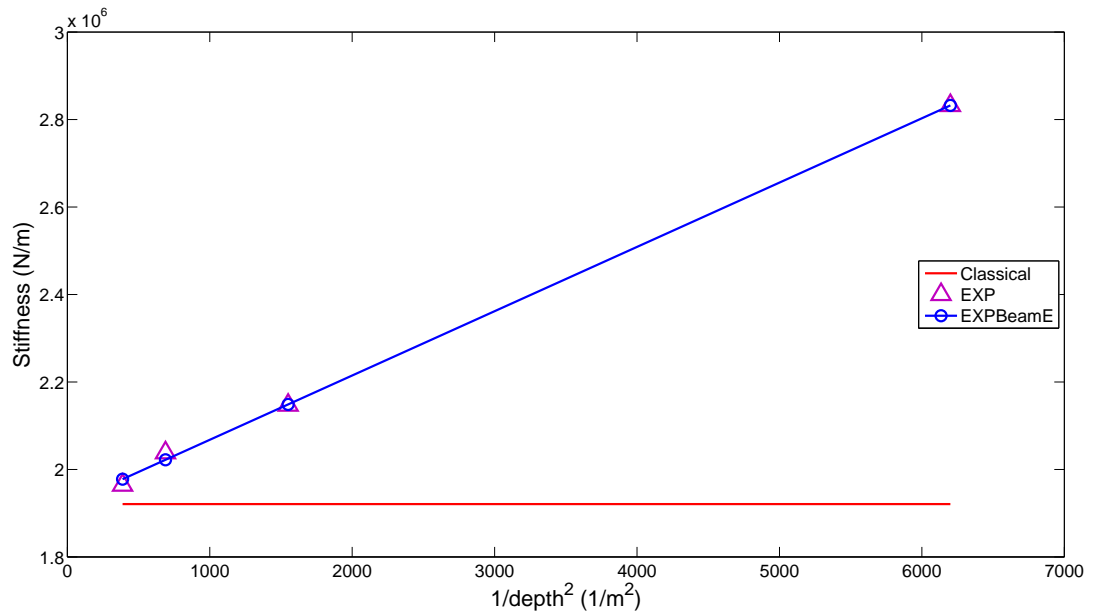


Figure 3.16: Stiffness result from Micropolar Beam element (*EXPBeamE*) for a given load (100N). Plotted against stiffness from the experimental procedure (*EXP*).

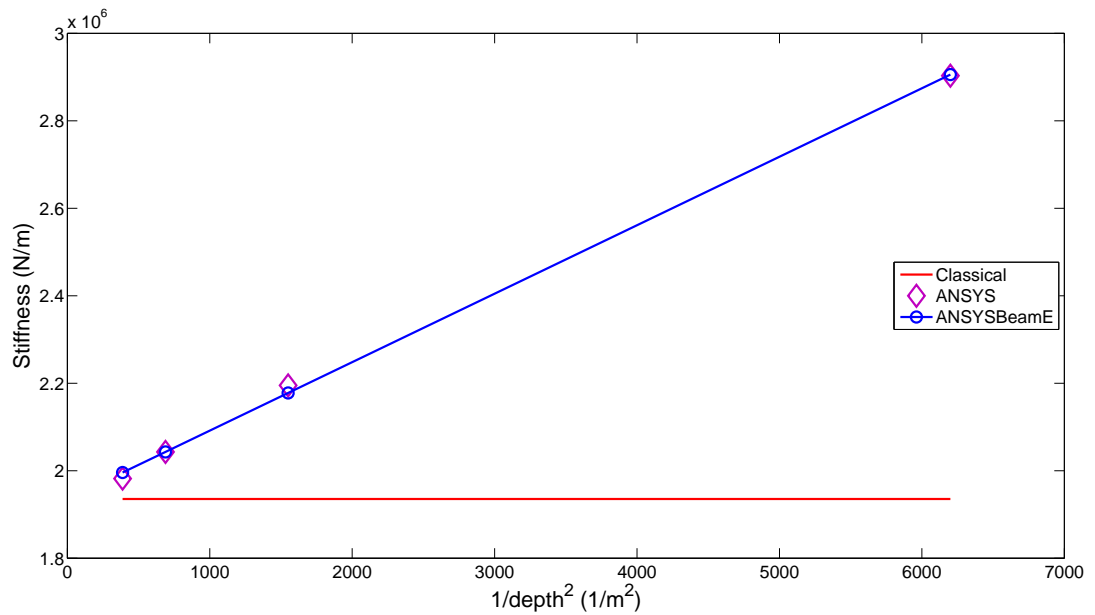


Figure 3.17: Stiffness result from Micropolar Beam element (*ANSYSBeamE*) for a given load (100N). Plotted against displacements gained from the ANSYS procedure (*ANSYS*).

processor with 1GB of RAM. The detailed finite element solution for all the HMD beams was computed in 233.8 seconds using ANSYS [36]. The new beam finite element computed the same displacement results in just 0.3 seconds using MATLAB [38]. The only drawback is that the material parameters, which are required to define the length scale of the micro structure, have to be determined experimentally. An understanding of which aspect of the microstructure informs the characteristic length may reduce the necessity to do this.

3.5 Conclusion

The use of a slender beam has identified that a size effect does exist in this model material and the micropolar flexural modulus and characteristic length of bending has been identified from this data using an analytical solution for the bending of slender micropolar beams. A slender micropolar beam finite element model has then been developed to allow the analysis of more complex space frame and lattice structures than can be achieved otherwise.

So far the model material has been shown to exhibit a size dependent stiffening for slender beam samples. This, however, does not identify if the model material is truly micropolar; the analytical slender beam solution is equivalent to couple stress theory. To distinguish between micropolar and couple stress theory the coupling number N requires to be identified. If the model material obeys couple stress elasticity then the coupling number would equal 1. Any other value between 0 and 1 would indicate that it is micropolar. This coupling number is identifiable in loading modes where shear is present. To date the identification of material properties by the method of size effects has been restricted to cases where an analytical solution exists. Typically the coupling number has been identified from torsion tests [12]; for the model material samples presented here this is not practicable. It is proposed that the beam samples can be tested at shorter spans thus introducing more transverse shear into the samples which would allow the coupling number to be identified. As an analytical solution is not easily achieved for this loading case, it is suggested that an approximate solution, obtained from a numerical procedure, can be used to identify the coupling number using exper-

imental data that is obtained from testing at shorter spans. A plane linear strain micropolar element is chosen as the preferred route as the constitutive relationships are readily available in the literature [27] and a linear strain formulation will capture the bending deformation more efficiently. The control volume finite element method will be used as it has been shown to have better performance over the equivalent finite element [26]. Seeking a plane micropolar element will also demonstrate numerical modelling at a different level of complexity. This will be the first time that a micropolar numerical procedure has been compared against experimental test results for the purpose of identifying constitutive properties. In the following chapter, a linear strain control volume finite element is compared against an equivalent finite element and constant strain formulation.

Chapter 4

Control Volume Finite Element Method

The finite element method (FEM) is the leading analysis technique in the field of computational structural mechanics. This is due, in part, to its versatility in accurately representing complex geometries. Control volume (CV) methods, allowing the same versatility with complex geometries, have been developed for both computational fluid mechanics and structural analysis applications [39–42]. In particular the control volume finite element method (CVFEM) is constructed upon the same mesh as the finite element discretisation. There are two types of CVFEM; a cell centred method and a vertex centred method. Recently a vertex centred CVFEM has been shown to provide better convergence, than the equivalent FEM, for a plane triangular element with both rotation and translation degrees of freedom [43]. The CVFEM has found favour with plate bending problems where both the cell centred [44] and vertex centred methods [45] have shown to be locking free for thick and thin Mindlin plates. It has also shown an increased accuracy over the FEM for micropolar elasticity [26]. Noting the promise of the CVFEM this was selected as the method of choice to develop a two dimensional linear strain micropolar element to gain an enhanced formulation better suited for beam bending. Before embarking upon the new formulation, however, a framework was developed within MATLAB [46], utilising symbolic mathematics, to allow a direct comparison of the FEM and CVFEM. The discrete Kirchhoff

triangular (DKT) element was chosen due to the readily available moment curvature relations, already presented in the literature [47], and the previous work presented with relation to Mindlin plate elements demonstrated that the CVFEM method has an aptitude for plate bending problems. A brief outline of the element formulation will follow. For further detail of the CV-DKT formulation and results see appendix A.

4.1 Discrete Kirchhoff Triangular Element

The DKT element is based upon Mindlin plate theory but has discrete Kirchhoff constraints, that is transverse shear is zero, applied at each node, giving rise to an element that converges to the thin Kirchhoff plates solution. The solution convergence of the control volume DKT is compared against the existing finite element DKT to evaluate the performance of the new procedure. Both the FE-DKT and CV-DKT formulations were build upon the same moment curvature matrix and both were solved in a quadrature free routine in order to have the best comparison of the numerical procedures. The CVFEM differs from the FEM by introducing a dual mesh of interconnecting control volumes over a standard triangular finite element mesh. The element stress resultants are then integrated around the control volume faces and equilibrium is imposed on the control volume. The resulting equilibrium equations then relate the control volume centre unknown displacements to those at the neighbouring centres, in a manner equivalent to the relationships between the nodal displacements characteristic of the FE method. A quadrature free implementation is achieved using the symbolic mathematics toolbox of MATLAB [46] which is built upon the Maple kernel. Symbolic integration (SI) is carried out in both the FE-DKT (A.20) and CV-DKT (A.27) codes to obtain the element stiffness matrix. The advantage of using symbolics is that an explicit solution to the stiffness matrix is achieved. The symbolic toolbox is capable of integrating the moment curvature matrix in a relatively quick time, with the solution extractable to form conventional code, see appendix B.1 for the code. This was validated by comparing the solution to the FE-DKT element stiffness matrix against the explicit FORTRAN code of Jeychandrabose et al. [48].

Both methods gave an identical solution. Results from the quadrature free FE-DKT and CV-DKT elements were compared against the SHELL63 element of ANSYS, a quadratic element composed of four DKT elements [49] where three point quadrature is employed in evaluating the stiffness matrix.

The CV-DKT has a proper rank to its stiffness matrix and passes the patch test for states of pure bending and twist. Convergence tests of maximum displacement against increasing discretisation, for various loading types and boundary conditions, were used to assess the performance of the CV-DKT element against the FE-DKT, quadrature free DKT, and the quadrature based ANSYS-DKT. For a uniform pressure load the convergence to the exact solution is more rapid than in the FE equivalents. For a point load case it is noted that the CV-DKT method predicts the central displacement as accurately as the quadrature free FE formulation at a given mesh refinement. Further results and discussions of boundary conditions can be found in appendix A.

With a framework developed, which utilises symbolic integration, the formulation of a six node triangular element, for plane micropolar elasticity, is now considered.

4.2 Micropolar Linear Strain Triangular Element

A quadratic displacement, linear strain, triangular micropolar plane stress/strain control volume finite element (CV-MPLST) has been developed. It is a 6 noded, 18 degrees of freedom element. The formulation of the CV-MPLST begins with a straight edged triangle with 3 vertex and 3 midside nodes, figure 4.1. The displacements in the x direction u , y direction v , and micro rotation ϕ_z are interpolated over the element with a complete quadratic polynomial from the nodal degrees of freedom, u_i , v_i and ϕ_{zi} where $i = 1 : 6$ refer to the element nodes.

$$u = \sum_{i=1}^6 N^i u_i \quad v = \sum_{i=1}^6 N^i v_i \quad \phi_z = \sum_{i=1}^6 N^i \phi_{zi} \quad (4.1)$$

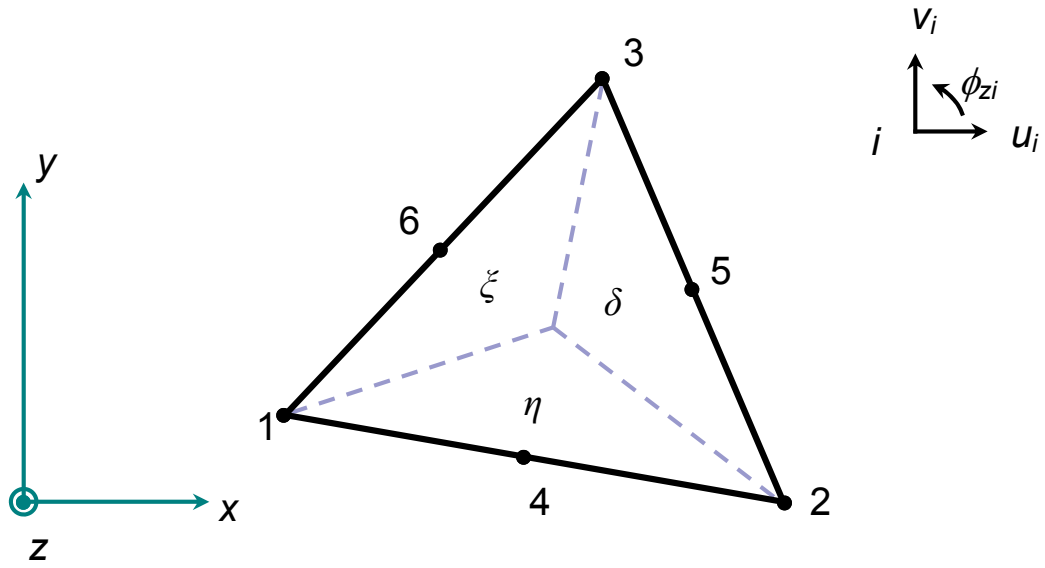


Figure 4.1: *Six node quadratic displacement triangular element*

The superscript i indicates position within the array. The shape functions N^i are functions of the natural area coordinates (δ, ξ, η) . The natural area coordinates are related to the element vertex coordinates, (x_1, x_2, x_3) and (y_1, y_2, y_3) , and global coordinate (x, y) by

$$\begin{aligned} x &= \delta x_1 + \xi x_2 + \eta x_3 \\ y &= \delta y_1 + \xi y_2 + \eta y_3 \end{aligned} \quad (4.2)$$

Vector $[\mathbf{N}]$ of shape functions is

$$[\mathbf{N}] = \left[\delta(2\delta - 1) \quad \xi(2\xi - 1) \quad \eta(2\eta - 1) \quad 4\delta\xi \quad 4\xi\eta \quad 4\eta\delta \right] \quad (4.3)$$

The displacement vector $\{\mathbf{d}\}$ is

$$\{\mathbf{d}\} = \left[u_i \quad v_i \quad \phi_{zi} \right]^T \quad \text{for } i = 1 : 6 \quad (4.4)$$

The unknown element displacements and micro rotations are related to the nodal degrees of freedom by

$$\begin{bmatrix} u \\ v \\ \phi_z \end{bmatrix} = [\mathbf{N}] \{\mathbf{d}\} \quad (4.5)$$

The strain vector $\{\varepsilon\}$ is related to the element displacements by

$$\{\varepsilon\} = \begin{bmatrix} \varepsilon_{xx} \\ \varepsilon_{yy} \\ \varepsilon_{yx} \\ \varepsilon_{xy} \\ \phi_{z,x} \\ \phi_{z,y} \end{bmatrix} = \begin{bmatrix} u_{,x} \\ v_{,y} \\ u_{,y} + \phi_z \\ v_{,x} - \phi_z \\ \phi_{z,x} \\ \phi_{z,y} \end{bmatrix} = \begin{bmatrix} \frac{\partial}{\partial x} & 0 & 0 \\ 0 & \frac{\partial}{\partial y} & 0 \\ \frac{\partial}{\partial y} & 0 & 1 \\ 0 & \frac{\partial}{\partial x} & -1 \\ 0 & 0 & \frac{\partial}{\partial x} \\ 0 & 0 & \frac{\partial}{\partial y} \end{bmatrix} \begin{bmatrix} u \\ v \\ \phi_z \end{bmatrix} \quad (4.6)$$

and the stress vector $\{\tau\}$ is related to the strain vector by

$$\{\tau\} = \begin{bmatrix} \tau_{xx} \\ \tau_{yy} \\ \tau_{yx} \\ \tau_{xy} \\ m_{xz} \\ m_{yz} \end{bmatrix} = [\mathbf{D}] \{\varepsilon\} \quad (4.7)$$

where \mathbf{D} refers to the constitutive matrix defined in section 2.2 with the inclusion of the constitutive properties for the micro rotation. For example in the plane stress case;

$$[\mathbf{D}] = \begin{bmatrix} \lambda + 2\mu^* + \kappa & \lambda & 0 & 0 & 0 & 0 \\ \lambda & \lambda + 2\mu^* + \kappa & 0 & 0 & 0 & 0 \\ 0 & 0 & \mu^* + \kappa & \mu^* & 0 & 0 \\ 0 & 0 & \mu^* & \mu^* + \kappa & 0 & 0 \\ 0 & 0 & 0 & 0 & \gamma & 0 \\ 0 & 0 & 0 & 0 & 0 & \gamma \end{bmatrix} \quad (4.8)$$

Differentiating the shape functions with respect to the spatial coordinates,

$$\begin{bmatrix} N_{,x} \\ N_{,y} \end{bmatrix} = \frac{1}{2A} \begin{bmatrix} y_{23}N_{,\delta} + y_{31}N_{,\xi} + y_{12}N_{,\eta} \\ -x_{23}N_{,\delta} - x_{31}N_{,\xi} - x_{12}N_{,\eta} \end{bmatrix} \quad (4.9)$$

where $y_{ij} = y_i - y_j$, $i = 1, 2, 3$ represents the vertex node numbers and (x_i, y_i) are the vertex node coordinates. A is the area of the triangular element. The derivatives of the shape functions with respect to the area coordinates are

$$N_{,\delta} = \begin{bmatrix} 4\delta - 1 & 0 & 0 & 4\xi & 0 & 4\eta \end{bmatrix} \quad (4.10)$$

$$N_{,\xi} = \begin{bmatrix} 0 & 4\xi - 1 & 0 & 4\delta & 4\eta & 0 \end{bmatrix} \quad (4.11)$$

$$N_{,\eta} = \begin{bmatrix} 0 & 0 & 4\eta - 1 & 0 & 4\xi & 4\delta \end{bmatrix} \quad (4.12)$$

These are used in the formulation of the strain displacement matrix $[\mathbf{B}]$ which relates the unknown nodal degrees of freedom to the element strain vector $\{\varepsilon\}$

$$\{\varepsilon\} = [\mathbf{B}] \begin{bmatrix} u_i \\ v_i \\ \phi_{zi} \end{bmatrix} \quad \text{for } i = 1 : 6 \quad \text{where } [\mathbf{B}] = \begin{bmatrix} N_{,x}^i & 0 & 0 \\ 0 & N_{,y}^i & 0 \\ N_{,y}^i & 0 & N^i \\ 0 & N_{,x}^i & -N^i \\ 0 & 0 & N_{,x}^i \\ 0 & 0 & N_{,y}^i \end{bmatrix} \quad (4.13)$$

It can now be said that the element stress resultants are related to the unknown nodal displacements by

$$\{\tau\} = [\mathbf{D}] [\mathbf{B}] \{\mathbf{d}\} \quad (4.14)$$

Now that the element stress displacement relationships have been defined the formulation of the CVFEM will depart from that of the standard finite element procedure.

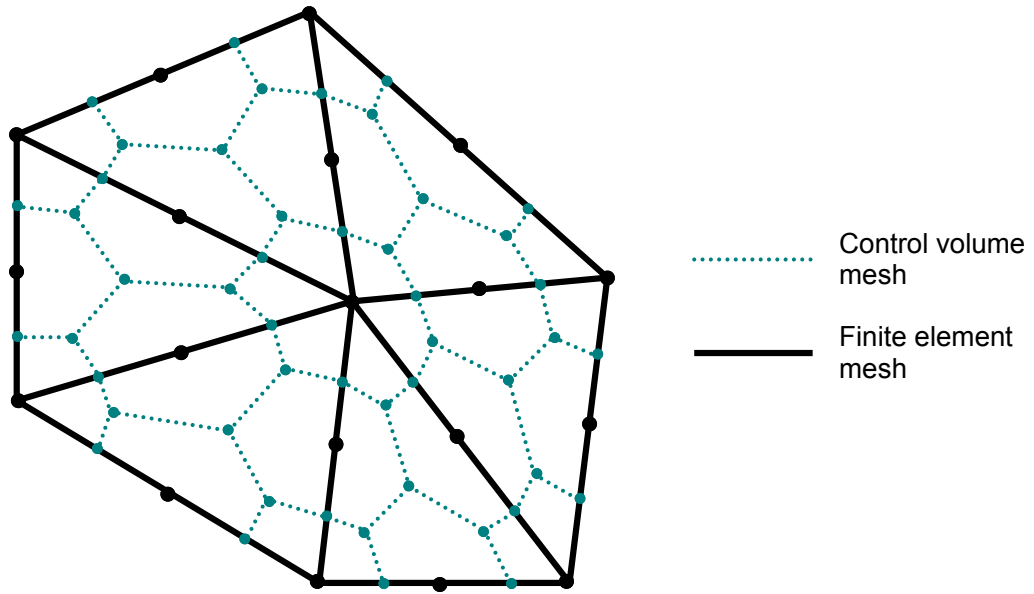


Figure 4.2: *Dual control volume mesh constructed around the vertices of a six node triangular finite element mesh*

Finite Element Stiffness Matrix

If, however, the formulation had been continued in the standard finite element manner the stiffness matrix is calculated thus,

$$\mathbf{k}_{\text{FEM}} = 2A \int_0^1 \int_0^{1-\eta} \mathbf{B}^T \mathbf{D}_b \mathbf{B} d\xi d\eta \quad (4.15)$$

In the comparison, that is made later between the FEM and CVFEM formulations of the element, this equation (4.15) is obtain by symbolic integration using the Maple kernel of MATLAB as in the DKT element.

4.2.1 Control Volume Formulation

A dual mesh of interconnecting control volumes is set up on the finite element mesh. Each control volume is centred upon a node of the element, see figure 4.2. The control volumes are constructed on an element by element basis as shown in figure 4.3. Table 4.1 shows the coordinates of the control volume nodes as

Table 4.1: Vertex coordinates, in triangular area coordinates, for the interconnecting control volume (CV) of a six node triangular element shown in figure 4.3

CV vertex	δ	ξ	η
a	3/4	1/4	0
b	1/4	3/4	0
c	0	3/4	1/4
d	0	1/4	3/4
e	1/4	0	3/4
f	3/4	0	1/4
g	3/5	1/5	1/5
h	1/5	3/5	1/5
g	1/5	1/5	3/5
h	1/3	1/3	1/3

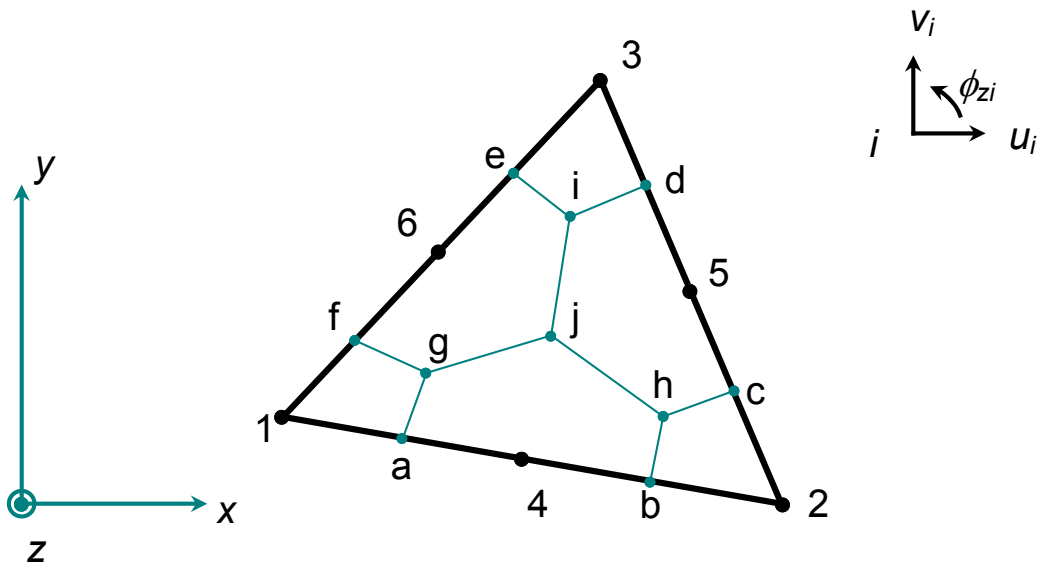


Figure 4.3: Sign convention for dual mesh on a single finite element mesh

represented by the area coordinates of the triangular element, although other coordinates can be used.

The equilibrium equations, section 2.2 and equations (2.17), (2.18) and (2.19), are setup for each control volume where the stress resultants acting upon the boundaries of the control volume are equilibrated against any body loadings imposed upon the control volume,

$$\sum_{i=1}^n F_x^i + p_x A_v = 0 \quad (4.16)$$

$$\sum_{i=1}^n F_y^i + p_y A_v = 0 \quad (4.17)$$

$$\sum_{i=1}^n M_z^i + q_z A_v = 0 \quad (4.18)$$

where F_x^i and F_y^i are components of the force resultants acting upon control volume face i , M_z^i is the couple resultant, A_v is the area of the control volume and n is the number of control volume faces around the finite element vertex or midside node that the control volume is centred on. The force and couple resultants are computed by integrating the functions of the stress variations within the finite element along each control volume face, figure 4.4. As each control volume face lies entirely within a given element, this is performed without storing any information relating to CV connectivity and is done on an element by element basis, giving a stiffness matrix for each triangular element. This allows the global stiffness matrix to be assembled in an identical manner to the finite element method. The discrete equilibrium equations for one control volume face are,

$$F_x^{mn} = \int \tau_{xx} \cos \theta_{mn} dr + \int \tau_{yx} \sin \theta_{mn} dr \quad (4.19)$$

$$F_y^{mn} = \int \tau_{yy} \sin \theta_{mn} dr + \int \tau_{xy} \cos \theta_{mn} dr \quad (4.20)$$

$$M_{zi}^{mn} = \int m_{xz} \cos \theta_{mn} dr + \int m_{yz} \sin \theta_{mn} dr + \int x' \tau_{xy} \cos \theta_{mn} dr - \int y' \tau_{yx} \sin \theta_{mn} dr \quad (4.21)$$

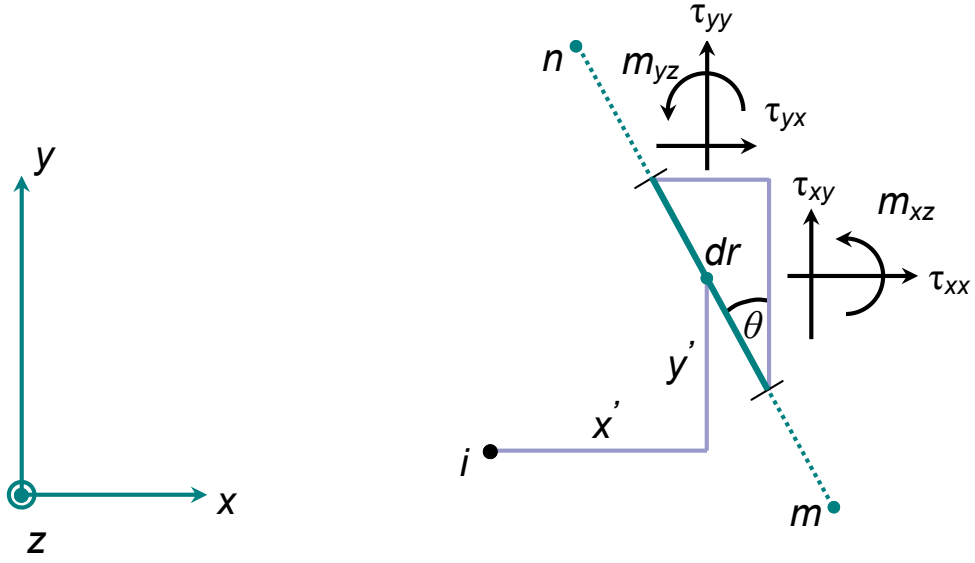


Figure 4.4: *Element stress resultants working on the face of the control volume*

where

$$\begin{aligned}
 \cos \theta_{mn} &= -\frac{y_{mn}}{l_{mn}} & x_{mn} &= x_m - x_n \\
 \sin \theta_{mn} &= \frac{x_{mn}}{l_{mn}} & y_{mn} &= y_m - y_n \\
 l_{mn} &= (x_{mn}^2 + y_{mn}^2)^{\frac{1}{2}}
 \end{aligned} \tag{4.22}$$

and m and n denote the vertices of the control volume face, figure 4.4. Moment arm functions x' and y' are the distances from the vertex or midside node i of the finite element, that the control volume is centred upon, and the control volume face:

$$\begin{aligned}
 x' &= x_e - x_i \\
 y' &= y_e - y_i
 \end{aligned} \tag{4.23}$$

where (x_i, y_i) are the coordinates of the finite element node that the control volume is centred upon and (x_e, y_e) are functions of the area coordinates that relate any point within the element to the vertex nodes of the corresponding

element.

$$\begin{aligned}x_e &= \delta x_1 + \xi x_2 + \eta x_3 \\y_e &= \delta y_1 + \xi y_2 + \eta y_3\end{aligned}\tag{4.24}$$

This becomes useful when the integration of the stress and couple stress resultants, equations (4.19), (4.20) and (4.21), is changed from the local line coordinate dr into an integration with the area coordinates of the triangular element. The integration in one of the area coordinates is dependent upon the CV face and thus each face has a different set of rules governing the integration of the stress resultants. As an example, consider the face lying between the CV vertices of a and g with length l_{ga} . The following substitutions are required,

$$\begin{aligned}\xi &= \frac{1}{3}\delta \\ \delta &= \frac{3}{4}(1 - \eta)\end{aligned}\tag{4.25}$$

These are substituted into the strain displacement matrix $[\mathbf{B}]$, equation (4.13), and the element coordinates x_e y_e , equation (4.24). This is to constrain the integration so that it is performed along the control volume face. A full list of these substitutions and the limits of the integration for each face is given in table 4.2. For this particular case the equilibrium equations become,

$$\mathbf{F}_x^{ga} = 5l_{ga} \cos \theta_{ga} \int_0^{\frac{1}{5}} \tau_{xx} d\eta + 5l_{ga} \sin \theta_{ga} \int_0^{\frac{1}{5}} \tau_{yx} d\eta\tag{4.26}$$

$$\mathbf{F}_y^{ga} = 5l_{ga} \sin \theta_{ga} \int_0^{\frac{1}{5}} \tau_{yy} d\eta + 5l_{ga} \cos \theta_{ga} \int_0^{\frac{1}{5}} \tau_{xy} d\eta\tag{4.27}$$

$$\begin{aligned}\mathbf{M}_{z1}^{ga} &= 5l_{ga} \cos \theta_{ga} \int_0^{\frac{1}{5}} m_{xz} d\eta + 5l_{ga} \sin \theta_{ga} \int_0^{\frac{1}{5}} m_{yz} d\eta \\ &+ 5l_{ga} \cos \theta_{ga} \int_0^{\frac{1}{5}} (x_e - x_1) \tau_{xy} d\eta - 5l_{ga} \sin \theta_{ga} \int_0^{\frac{1}{5}} (y_e - y_1) \tau_{yx} d\eta\end{aligned}\tag{4.28}$$

These integrations are repeated for each individual CV face, performing the necessary substitutions. This will give three row vectors, \mathbf{F}_x , \mathbf{F}_y and \mathbf{M}_z , for each CV face that relates the internal actions to the unknown nodal degrees of freedom. These are calculated for each CV face in an element and assembled to form the element stiffness matrix, \mathbf{k} , thus

Table 4.2: *Substitutions for the equilibrium equation integrals and stress displacement relationships*

Direction of Integration	Integral Substitutions	Area Coordinate Substitutions
from a to g	$\int dr = 5l_{ga} \int_0^{\frac{1}{5}} d\eta$	letting $\xi = \frac{1}{3}\delta$ and $\delta = \frac{3}{4}(1 - \eta)$
from b to h	$\int dr = 5l_{hb} \int_0^{\frac{1}{5}} d\eta$	letting $\delta = \frac{1}{3}\xi$ and $\xi = \frac{3}{4}(1 - \eta)$
from j to i	$\int dr = \frac{15}{4}l_{ji} \int_{\frac{1}{3}}^{\frac{3}{5}} d\eta$	letting $\delta = \xi$ and $\xi = \frac{1}{2}(1 - \eta)$
from e to i	$\int dr = 5l_{ie} \int_0^{\frac{1}{5}} d\xi$	letting $\delta = \frac{1}{3}\eta$ and $\eta = \frac{3}{4}(1 - \xi)$
from f to g	$\int dr = 5l_{gf} \int_0^{\frac{1}{5}} d\xi$	letting $\eta = \frac{1}{3}\delta$ and $\delta = \frac{3}{4}(1 - \xi)$
from j to h	$\int dr = \frac{15}{4}l_{jh} \int_{\frac{1}{3}}^{\frac{3}{5}} d\xi$	letting $\delta = \eta$ and $\eta = \frac{1}{2}(1 - \xi)$
from c to h	$\int dr = 5l_{hc} \int_0^{\frac{1}{5}} d\delta$	letting $\eta = \frac{1}{3}\xi$ and $\xi = \frac{3}{4}(1 - \delta)$
from d to i	$\int dr = 5l_{id} \int_0^{\frac{1}{5}} d\delta$	letting $\xi = \frac{1}{3}\eta$ and $\eta = \frac{3}{4}(1 - \delta)$
from j to g	$\int dr = \frac{15}{4}l_{jg} \int_{\frac{1}{3}}^{\frac{3}{5}} d\delta$	letting $\xi = \eta$ and $\eta = \frac{1}{2}(1 - \delta)$

$$[\mathbf{k}] \{\mathbf{d}\} = \begin{bmatrix}
\mathbf{F}_x^{gf} - \mathbf{F}_x^{ga} \\
\mathbf{F}_y^{gf} - \mathbf{F}_y^{ga} \\
\mathbf{M}_{z1}^{gf} - \mathbf{M}_{z1}^{ga} \\
\mathbf{F}_x^{hb} - \mathbf{F}_x^{hc} \\
\mathbf{F}_y^{hb} - \mathbf{F}_y^{hc} \\
\mathbf{M}_{z2}^{hb} - \mathbf{M}_{z2}^{hc} \\
\mathbf{F}_x^{id} - \mathbf{F}_x^{ie} \\
\mathbf{F}_y^{id} - \mathbf{F}_y^{ie} \\
\mathbf{M}_{z3}^{id} - \mathbf{M}_{z3}^{ie} \\
\mathbf{F}_x^{ga} + \mathbf{F}_x^{jg} - \mathbf{F}_x^{jh} - \mathbf{F}_x^{hb} \\
\mathbf{F}_y^{ga} + \mathbf{F}_y^{jg} - \mathbf{F}_y^{jh} - \mathbf{F}_y^{hb} \\
\mathbf{M}_{z4}^{ga} + \mathbf{M}_{z4}^{jg} - \mathbf{M}_{z4}^{jh} - \mathbf{M}_{z4}^{hb} \\
\mathbf{F}_x^{hc} + \mathbf{F}_x^{jh} - \mathbf{F}_x^{ji} - \mathbf{F}_x^{id} \\
\mathbf{F}_y^{hc} + \mathbf{F}_y^{jh} - \mathbf{F}_y^{ji} - \mathbf{F}_y^{id} \\
\mathbf{M}_{z5}^{hc} + \mathbf{M}_{z5}^{jh} - \mathbf{M}_{z5}^{ji} - \mathbf{M}_{z5}^{id} \\
\mathbf{F}_x^{ie} + \mathbf{F}_x^{ji} - \mathbf{F}_x^{jg} - \mathbf{F}_x^{gf} \\
\mathbf{F}_y^{ie} + \mathbf{F}_y^{ji} - \mathbf{F}_y^{jg} - \mathbf{F}_y^{gf} \\
\mathbf{M}_{z6}^{ie} + \mathbf{M}_{z6}^{ji} - \mathbf{M}_{z6}^{jg} - \mathbf{M}_{z6}^{gf}
\end{bmatrix} = \{\mathbf{P}\} \quad (4.29)$$

where $\{\mathbf{P}\}$ is the vector of applied forces and moments. An explicit code for carrying out this assembly of the stiffness matrix, in MATLAB using the symbolic mathematics tool box, can be seen in appendix B.2. Now that the element stiffness matrix has been formulated the procedure returns to that of the standard finite element method. The global stiffness matrix is assembled, boundary conditions applied and the solution found in the usual way. The stress recovery routine is also the same as the finite element method.

4.2.2 Validation

The element is validated using the patch tests [25] to test the accuracy for simple stress states and the stress concentration problem [26], for which an analytical solution exists, to ascertain how the element accuracy performs with changing length scale and coupling factors. In the validations, comparisons are made to a

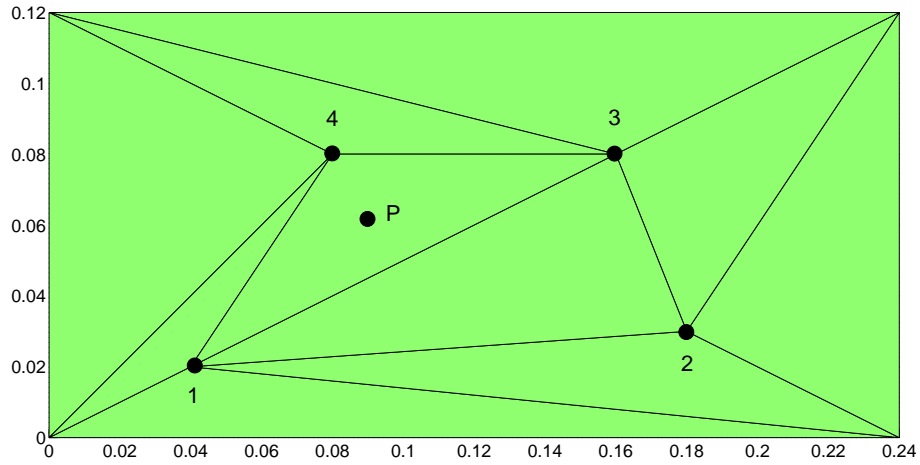


Figure 4.5: *Mesh for micropolar element patch test, lengths in (mm)*

constant strain control volume element, CV-MPCST, from [26]. Reference is also made to finite element formulations based upon the same strain displacement relationships as their equivalent linear and constant strain control volume elements. For the finite elements, the determination of the element stiffness matrix is the same as in [23] and symbolic integration of equation 4.15 is employed, as in the formulation of the DKT, so as to eliminate quadrature.

Patch Test

The mesh of elements shown in figure 4.5 is loaded under three different loading conditions. For each loading conditions there is a known displacement and stress field that should be gained, a summary of which can be seen in table 4.3. The internal vertex nodal coordinates and constitutive properties can be found in table 4.4. The plane strain formulation was used. Midside nodes are equal distance along the finite element edge. The first patch is for a uniform direct stress with symmetric shear. In the second test the direct stress remains uniform whereas the shear stress is now antisymmetric and a body couple is applied. The final test has constant direct stresses and body forces, linearly varying body couples

Table 4.3: *Body and boundary loadings and displacement field solutions for micropolar element patch test.*

<i>Patch 1</i>
Load: $p_x = p_y = q$, $\tau_{xx} = \tau_{yy} = 4$, $\tau_{xy} = \tau_{yx} = 1.5$, $m_x = m_y = 0$
Solution: $u = 10^{-3} [x + \frac{1}{2}y]$, $v = 10^{-3} [x + y]$, $\phi = \frac{1}{4}10^{-3}$
<i>Patch 2</i>
Load: $p_x = p_y$, $q = 1$, $\tau_{xx} = \tau_{yy} = 4$, $\tau_{xy} = 1$, $\tau_{yx} = 2$, $m_x = m_y = 0$
Solution: $u = 10^{-3} [x + \frac{1}{2}y]$, $v = 10^{-3} [x + y]$, $\phi = 10^{-3} [\frac{1}{4} + \frac{1}{4\alpha}]$, $\alpha = 0.5$
<i>Patch 3</i>
Load: $p_x = p_y = 1$, $q = 2[x - y]$, $\tau_{xx} = \tau_{yy} = 4$, $\tau_{xy} = 1.5 - [x - y]$, $\tau_{yx} = 1.5 + [x - y]$, $m_x = -m_y = \frac{2l^2}{\alpha}$, $\alpha = 0.5$
Solution: $u = 10^{-3} [x + \frac{1}{2}y]$, $v = 10^{-3} [x + y]$, $\phi = 10^{-3} [\frac{1}{4} + \frac{1}{2\alpha} (x - y)]$

Table 4.4: *Vertex coordinates and constitutive properties for micropolar element patch test*

node	$x(\text{mm})$	$y(\text{mm})$
1	0.04	0.02
2	0.18	0.03
3	0.16	0.08
4	0.08	0.08
P	0.0933	0.06

$G_m = 1.0\text{e}9\text{N}/\text{m}^2$
 $\nu_m = 0.25$
 $l = 0.1\text{mm}$
 $a = 0.5$

Table 4.5: Results for displacement and micro rotation at node 2. Stress and couple stress at point P in the patch test mesh under loading cases 1 and 2

Test	$u(10^3)$	$v(10^3)$	$\phi(10^3)$	τ_{xx}	τ_{yy}	m_x
1	0.19500	0.21000	0.25000	4.00000	1.49999	$-3.0e-15$
Exact	0.19500	0.21000	0.25000	4.00000	1.50000	0
2	0.20999	0.11999	0.24999	3.99999	0.99999	$-3.7e-9$
Exact	0.21000	0.12000	0.25000	4.00000	1.00000	0

Table 4.6: Results for displacement and micro rotation at node 2. Stress and couple stress at point P in the patch test mesh under loading case 3. Results shown against exact solution for linear strain control volume CV-MPLST and constant strain control volume CV-MPCST

Code	$u(10^3)$	$v(10^3)$	$\phi(10^3)$	τ_{xx}	τ_{yy}	m_x
CV-MPCST	0.19500	0.21000	0.40000	4.00000	1.46666	0.04000
CV-MPLST	0.19499	0.20999	0.39999	3.99999	1.46669	0.03999
Exact	0.19500	0.21000	0.40000	4.00000	1.46666	0.04000
CV-MPLST (inc. direct τ)	0.19499	0.20999	0.39999	3.99999	1.46669	0.03999

and linearly varying antisymmetric shear. The control volume passes the first two tests, table 4.5, and results for the final test are shown in table 4.6 where a comparison is made between the linear strain control volume, CV-MPLST from this work, and the constant strain control volume, CV-MPCST, which has been shown to out perform the equivalent, constant and linear strain, finite element formulations [26]. As can be seen, the CV-MPLST does not reproduce the analytical solution as accurately as the CV-MPCST formulation; this is put down to rounding errors. There is also a difference in the formulation from the linear strain to the constant strain. The constant strain formulation wrongly includes moments contributed by the direct stresses τ_{xx} and τ_{yy} in the moment equilibrium equation. As these are not included in the equilibrium equation (2.16) for a micropolar material, these were omitted in the CV-MPLST formulation. To check the validity of this assumption, however, the direct stresses are included in one run of patch test 3, with the additional loads made on the boundary. These additional loads are required to keep the boundary control volumes in rotational

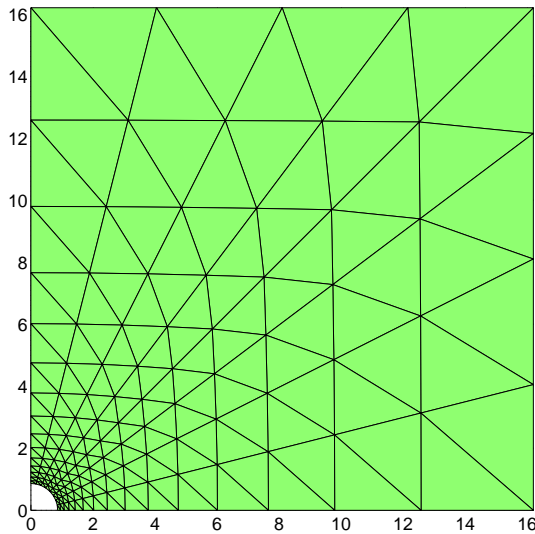


Figure 4.6: *Stress concentration mesh $8 \times 15 \times 4$ $r = 0.864\text{mm}$. Quarter plate edge lengths are $16.2\text{mm} \times 16.2\text{mm}$.*

equilibrium as the applied direct stresses introduce an out of balance moment. It can be seen that the patch test results are the same.

Stress Concentration Problem

A common test to check the accuracy of a micropolar code is to check it against one of the few analytical solutions available; that of the stress concentration factor of maximum circumferential stress around a circular hole in an infinite plate [7]. For the purposes of the analysis, the plate considered will be finite but the hole radius will be small in comparison to the width of the plate. A comparison is made between the constant strain control volume, linear strain control volume, constant strain finite element and linear strain finite element all for the same mesh. A quarter of the plate is modelled with symmetry boundary conditions, see figure 4.6. The results presented here are different from those given in the published literature. This is because it is difficult to determine the element distributions given in the different publications. This is important as the stress concentration values are mesh sensitive. Therefore to gain a better understanding

Table 4.7: Stress concentration factors for maximum circumferential stress at circular hole by the constant strain control volume, CV-MPCST, linear strain control volume, CV-MPLST, constant strain finite element, FE-MPCST, and linear strain finite element, FE-MPLST. Hole radius 0.216mm, $G_m = 1.0e9N/m^2$, $\nu_m = 0.3$ and (A): $\frac{r}{l} = 1.063$ (B): $\frac{r}{l} = 10.63$. Mesh is 8x22x4 elements.

a	(A)				
	Exact	CV-MPCST	CV-MPLST	FE-MPCST	FE-MPLST
0.0	3.000	2.871 (4.3)	3.040 (1.3)	2.871 (4.3)	3.047 (1.6)
0.0667	2.849	2.758 (3.2)	2.888 (1.4)	2.757 (3.2)	2.893 (1.5)
0.3333	2.555	2.520 (1.4)	2.589 (1.3)	2.518 (1.4)	2.591 (1.4)
1.2857	2.287	2.276 (0.5)	2.315 (1.2)	2.272 (0.7)	2.316 (1.3)
4.2632	2.158	2.111 (2.2)	2.184 (1.2)	2.103 (2.5)	2.185 (1.3)
a	(B)				
	Exact	CV-MPCST	CV-MPLST	FE-MPCST	FE-MPLST
0.0	3.000	2.871 (4.3)	3.040 (1.3)	2.871 (4.3)	3.047 (1.6)
0.0667	2.956	2.849 (3.6)	2.995 (1.3)	2.837 (4.0)	3.002 (1.6)
0.3333	2.935	2.830 (3.6)	2.978 (1.5)	2.808 (4.3)	2.985 (1.7)
1.2857	2.927	2.789 (4.7)	2.986 (2.0)	2.745 (6.2)	2.993 (2.3)
4.2632	2.923	2.684 (8.2)	3.020 (3.3)	2.594 (11.3)	3.027 (3.6)

of the accuracy of the competing methods the same element distribution should ideally be used.

The first test compares how the accuracy of the solution is affected by changing the level of coupling between the shear strains, governed by the coupling factor, a . This is carried out for two ratios of hole radius r and characteristic length l . As the radius is fixed for both (A) and (B) cases, see table 4.7, then only the characteristic length is changed. It can be seen in (A), when the characteristic length is almost equal to the radius, that CV-MPLST has a more consistent error compared to CV-MPCST. CV-MPCST is more accurate for middle values of coupling factor, a , where as CV-MPLST is a better accuracy for the classical case ($a=0$) and approaching the couple stress case ($a \rightarrow \infty$). This pattern is repeated for the finite element formulations however these are marginally less accurate than the equivalent control volume formulation. On reducing the characteristic length, case (B), the error for large coupling factors is greater. This is particularly prominent for the constant strain formulations.

Table 4.8: *Stress concentration factors for maximum circumferential stress at circular hole by the constant strain control volume, CV-MPCST, linear strain control volume, CV-MPLST, constant strain finite element, FE-MPCST, and linear strain finite element, FE-MPLST. Hole radius 0.864mm, $G_m = 1.0e9N/m^2$, $\nu_m = 0.3$ and $a = 0.3333$. Mesh is 8x15x4 elements.*

$\frac{r}{l}$	Exact	CV-MPCST	CV-MPLST	FE-MPCST	FE-MPLST
1.0	2.549	2.518 (1.2)	2.589 (1.6)	2.516 (1.3)	2.588 (1.5)
2.0	2.641	2.603 (1.5)	2.685 (1.7)	2.595 (1.7)	2.684 (1.6)
3.0	2.719	2.674 (1.6)	2.766 (1.7)	2.662 (2.1)	2.765 (1.7)
4.0	2.779	2.730 (1.7)	2.829 (1.8)	2.712 (2.4)	2.827 (1.7)
6.0	2.857	2.806 (1.8)	2.912 (1.9)	2.778 (2.8)	2.909 (1.8)
8.0	2.902	2.851 (1.8)	2.961 (2.0)	2.815 (3.0)	2.956 (1.9)
10.0	2.929	2.879 (1.7)	2.991 (2.1)	2.837 (3.2)	2.985 (1.9)

The other case considered is that of a larger hole within the same finite plate. The coupling factor is kept constant and the characteristic length reduced, see table 4.8. It can be seen for this hole radius the CV-MPLST is less accurate at predicting the stress concentration factor compared to the CV-MPCST. Indeed for this case, it is performing less favourably than the CV-MPCST. It is proposed that the finite nature of the plate, compared to the size of the larger hole, is affecting the linear strain element more than the constant strain element. It is of interest that this conclusion is not borne out in the finite element formulations where the reverse is observed. Nevertheless, when a comparison is made between the two quadratic formulations, CV-MPLST and FE-MPLST, the solution accuracy is broadly similar with the FE-MPLST, at most 0.2% more accurate.

Beam Bending

With the primary focus of this work being concerned with beam bending, the convergence of CV-MPCST, CV-MPLST and FE-MPLST to micropolar slender beam theory, figure 4.7, and solution time, figure 4.8, were compared using the constitutive properties from ANSYS HMD and beam dimensions for HMD.B.1. Using these constitutive properties, $E_{fm} = 3.900e10 N/m^2$ and $l_b = 8.99$ mm and beam dimensions, $L = 128$ mm and $d = 12.7$ mm, means that $l_b \approx d$ which will

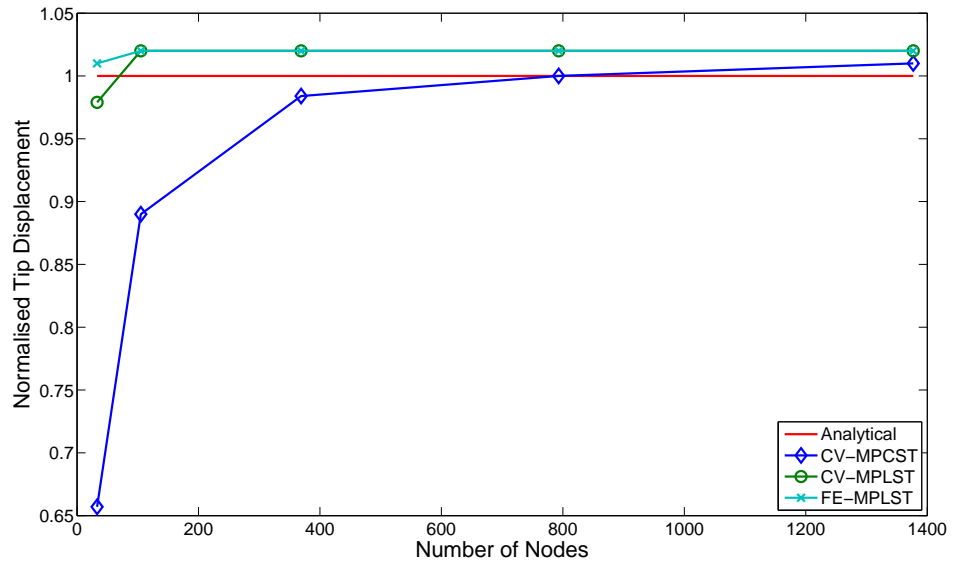


Figure 4.7: Convergence to slender beam solution for increasing degrees of freedom

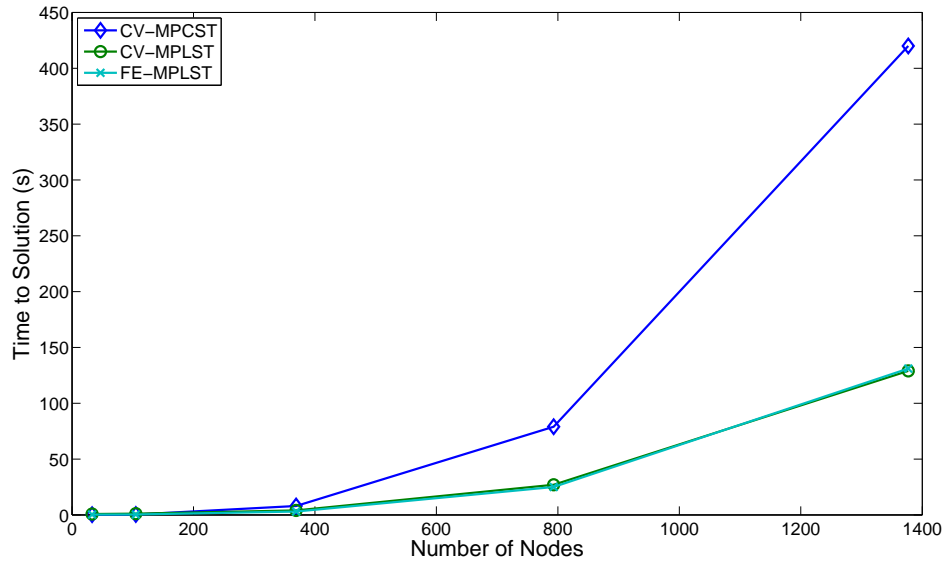


Figure 4.8: Time to solution for slender beam solution for increasing degrees of freedom

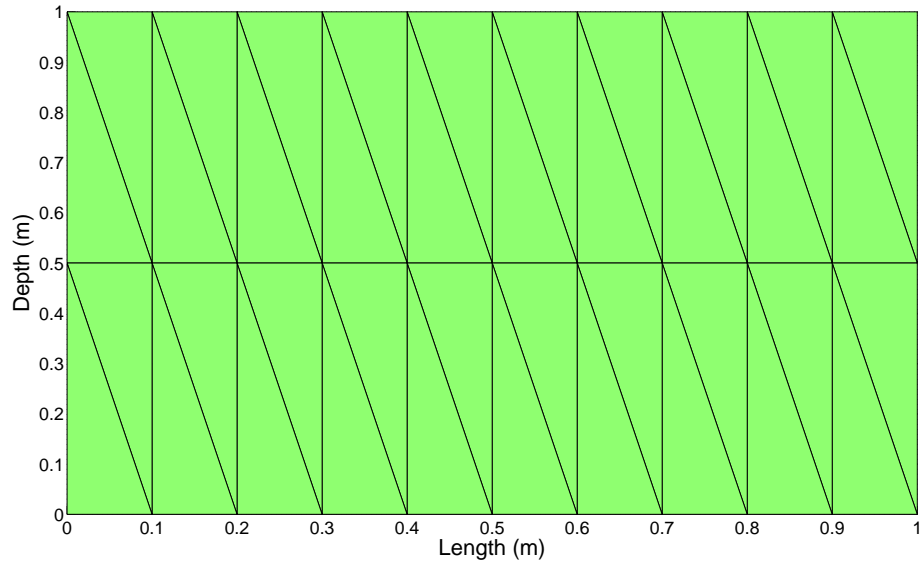


Figure 4.9: *Unit beam mesh*

give a micropolar response. The beam mesh used is of the form shown in figure 4.9, where the horizontal and vertical nodal coordinates are scaled by the length and depth of the beam respectively. To replicate the three point bending loading condition the beam was modelled as a cantilever with half the length and half the applied load of the corresponding beam in three point bending. The built in boundary condition of the cantilever is necessary to enforce a zero micro rotation boundary condition that is required at the midspan of the beam under three point bending. In order to get the corresponding stiffness, the maximum displacement should be divided by twice the load applied to the cantilever. CV-MPLST has greater convergence of maximum displacement on increasing number of nodes and a reduced solution time when compared to CV-MPCST. Comparing the FE and CV linear strain formulations there is no appreciable difference in convergence or solution time; the same matrix solver, MATLAB “\” was used in both cases. Neither formulation converges to the slender beam solution due to the use of $N = 0.9$ and not $N = 1$. If $N = 1$ were used it would lead to indeterminate shear stresses. Using $N = 0.9$, however, does show that the accuracy of the element is close to that of the slender beam analytical solution, predicting an increased tip displacement as would be expected.

4.3 Conclusion

Based upon the results shown the CV-MPLST is chosen as the formulation to be used in the determination of the coupling number. Although it has no appreciable advantage over the FE-MPLST in bending problems, it does show an increased accuracy for the stress concentration problem, particularly over a wide range of coupling factors. As the numerical procedure will be used for determining the coupling number, CV-MPLST is chosen.

Chapter 5

Model Material - Deep Beam

A linear strain micropolar control volume finite element, CV-MPLST, has been developed. The CV-MPLST element will now be used to ascertain the coupling number allowing a distinction to be made between couple stress and micropolar elasticity. As already stated; if the model material obeys couple stress elasticity then the coupling number would equal 1. Any other value between 0 and 1 would indicate that it is micropolar. To this effect the model material beam test pieces were loaded again in three point bending at shorter spans. The lower aspect ratios introduce transverse shear into the test samples and as shear stress is related to the shear strain by the coupling number, in a micropolar material, this should allow the coupling number to be identified.

The figures that follow detail the classical lower bound limit $N = 0$ and the upper bound corresponding to $N = 0.9$ that approximates the couple stress limit. These are calculated using the CV-MPLST in plane stress, as in the ANSYS model, and constitutive properties from the slender beam ANSYS results (table 3.4); a Poisson's ratio of 0.3 is assumed. It is not possible to include results for $N = 1$ as the numerical solution becomes unstable as it approaches the couple stress limit because it leads to indeterminate shear stresses. If the model material was micropolar the stiffness results should lie between these bounds. The beams were tested at two reduced aspect ratios, these being approximately 75% and 50% of the slender beams. Sample plots with a range of N values, based upon the HMD

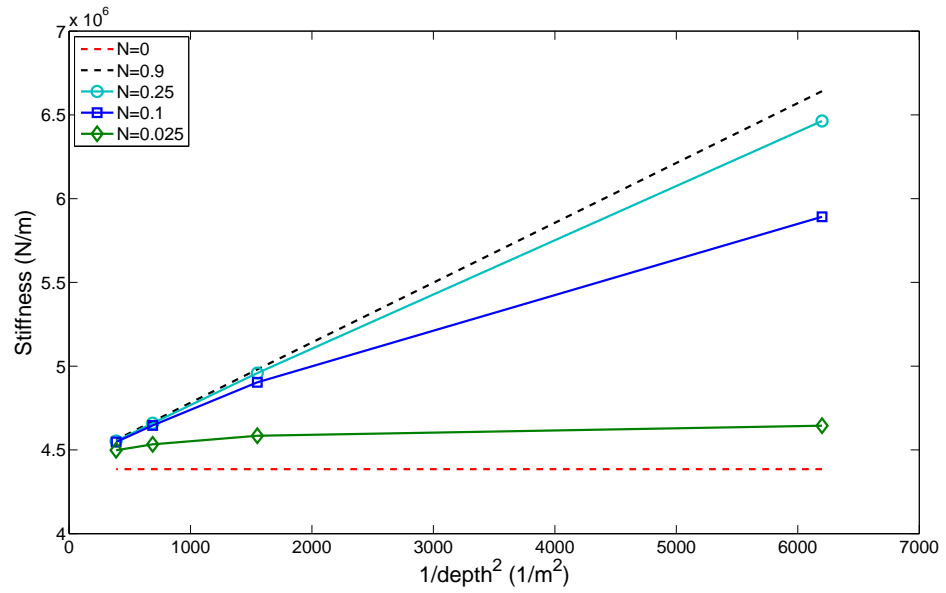


Figure 5.1: *Stiffness against $1/\text{depth}^2$ at $L/d = 7.56$ for various coupling numbers with material properties from slender HMD beams*

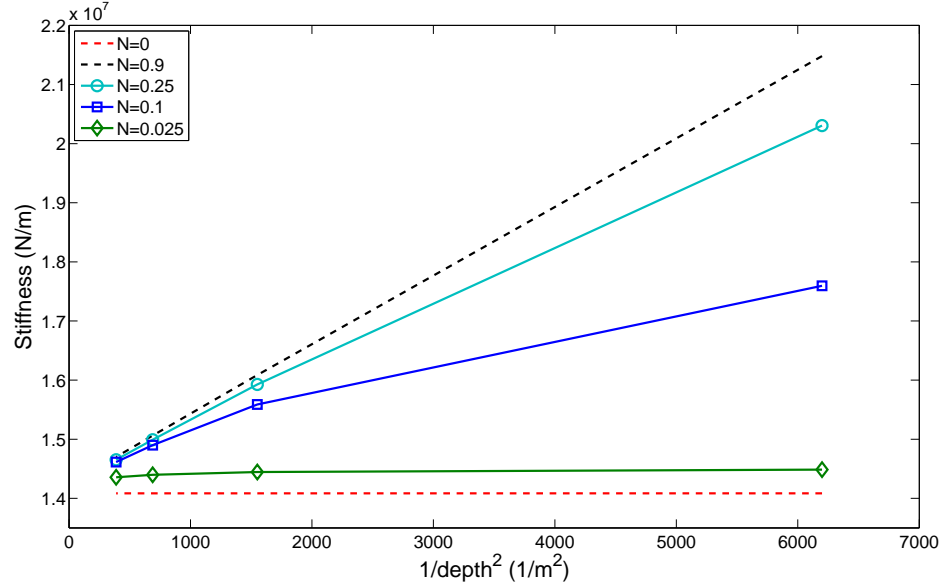


Figure 5.2: *Stiffness against $1/\text{depth}^2$ at $L/d = 5.04$ for various coupling numbers with material properties from slender HMD beams*

slender beam constitutive properties are shown for both of the lower aspect ratios in figures 5.1 and 5.2. These demonstrate the sensitivity of the stiffness variation to the value of N . Clearly as N reduces the variation departs from the linear couple stress case and tends towards the classical case as N vanishes.

5.1 Experimental Results

The shorter beam samples were tested in a similar manner to the slender beams. Again the three point bending rig flexure was subtracted from the experimental stiffness results and a detailed finite element analysis was carried out in ANSYS. As in the slender beams, the aspect ratios are not exact integer values because a consistent load position midway between voids is maintained. Table 5.1 shows the beam dimensions and stiffness results from the experiments and detailed ANSYS model for the HMD test pieces and table 5.2 for the LMD test pieces. The results are also depicted in figures 5.3 and 5.4 for the HMD and figures 5.5 and 5.6 for the LMD materials. All reported stiffness values are from displacement results corrected for test rig flexure.

Excellent agreement is shown between the corrected and ANSYS results for HMD at $L/d = 7.56$, figure 5.3. It can be seen that there is a departure from linearity and the solution sits between the classical and couple stress solutions, as would be expected for a genuinely micropolar material. The departure from linearity becomes more noticeable still in HMD at $L/d = 5.04$, figure 5.4. At this span, however, there is less agreement between the ANSYS model and corrected experimental results. While the plots vary similarly the data are not coincident and there is an offset from the anticipated range between the bounds determined using the constitutive properties from the slender beam tests. A noticeable error is, again, seen for LMD at $L/d = 8.50$ between ANSYS and the corrected experimental results, figure 5.5. This is also true for LMD at $L/d = 5.67$, figure 5.6 with the same departure from the expected range of results set by the coupling number.

There are two phenomena in these results that merit discussion; the lack of agree-

Table 5.1: *Beam test geometry and corrected stiffness results, K , for deep HMD test pieces*

Beam	Depth (mm)	Length (mm)	L/d	K_{Exp} (N/m)	K_{Ansys} (N/m)
HMD_B1_7	12.7	96	7.56	6.423e6	6.441e6
HMD_B2_7	25.4	192	7.56	4.986e6	5.018e6
HMD_B3_7	38.1	288	7.56	4.621e6	4.706e6
HMD_B4_7	50.8	384	7.56	4.423e6	4.557e6
HMD_B1_5	12.7	64	5.04	1.683e7	1.826e7
HMD_B2_5	25.4	128	5.04	1.356e7	1.522e7
HMD_B3_5	38.1	192	5.04	1.313e7	1.459e7
HMD_B4_5	50.8	256	5.04	1.260e7	1.400e7

Table 5.2: *Beam test geometry and corrected stiffness results, K , for deep LMD test pieces*

Beam	Depth (mm)	Length (mm)	L/d	K_{Exp} (N/m)	K_{Ansys} (N/m)
LMD_B1_7	12.7	108	8.50	3.891e6	4.012e6
LMD_B2_7	25.4	216	8.50	2.709e6	3.043e6
LMD_B3_7	38.1	324	8.50	2.756e6	2.833e6
LMD_B4_7	50.8	432	8.50	2.813e6	2.742e6
LMD_B1_5	12.7	72	5.67	8.715e6	1.083e7
LMD_B2_5	25.4	144	5.67	7.357e6	8.837e6
LMD_B3_5	38.1	216	5.67	7.765e6	8.372e6
LMD_B4_5	50.8	288	5.67	7.499e6	8.066e6

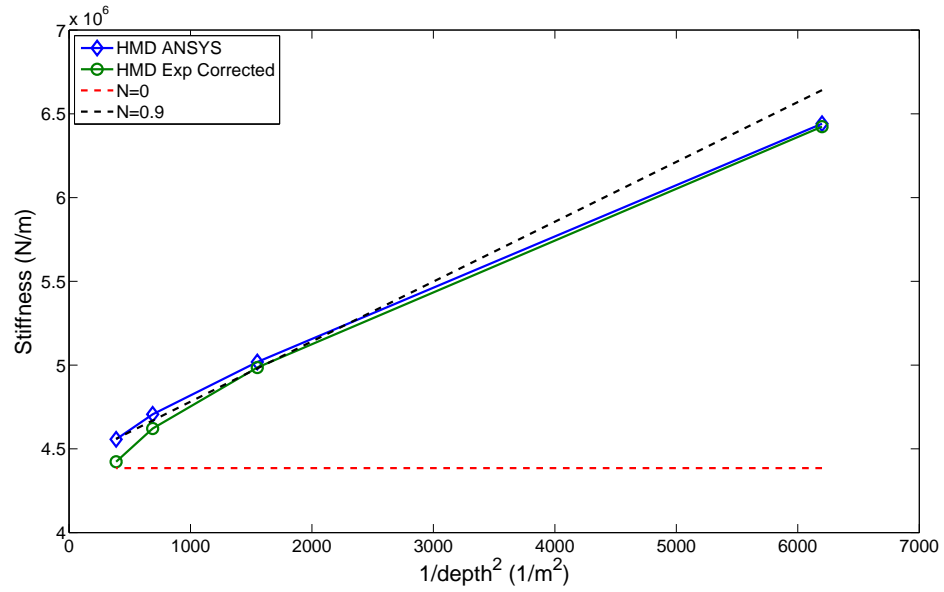


Figure 5.3: Stiffness against $1/\text{depth}^2$ for HMD beams at $L/d = 7.56$. Comparing discrete detail ANSYS and experimental results corrected for test rig flexure against classical solution

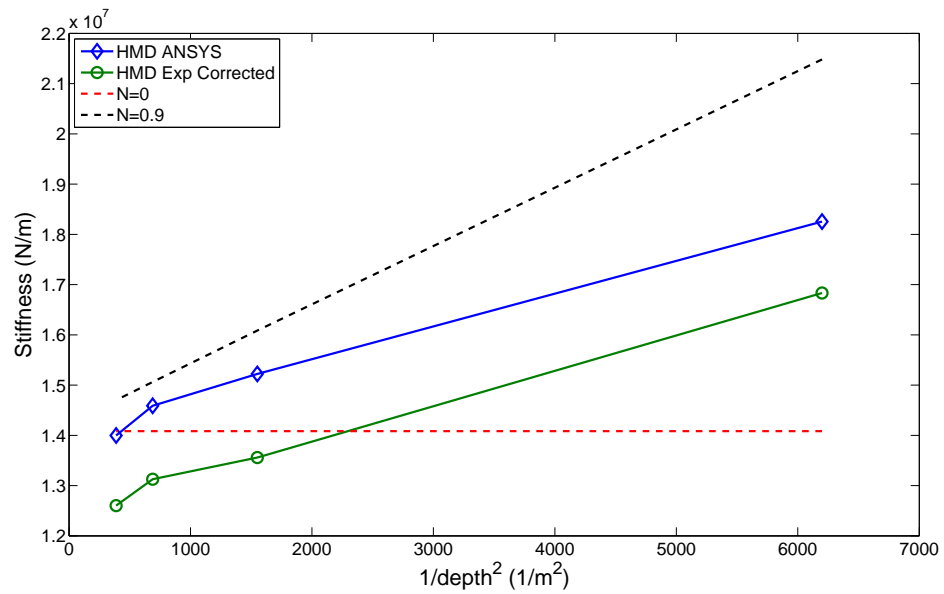


Figure 5.4: Stiffness against $1/\text{depth}^2$ for HMD beams at $L/d = 5.04$. Comparing discrete detail ANSYS and experimental results corrected for test rig flexure against classical solution

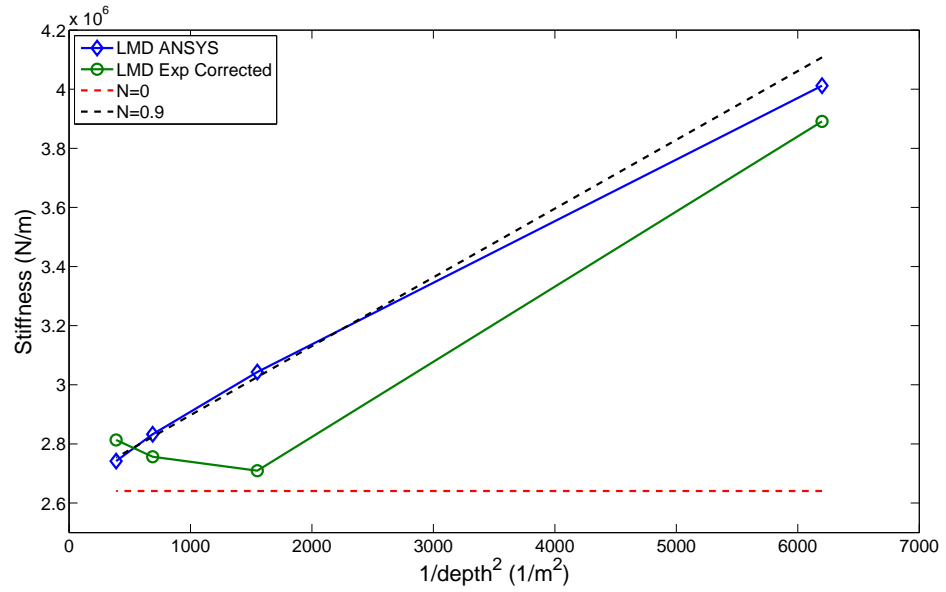


Figure 5.5: *Stiffness against $1/\text{depth}^2$ for LMD beams at $L/d = 8.50$. Comparing discrete detail ANSYS and experimental results corrected for test rig flexure against classical solution*

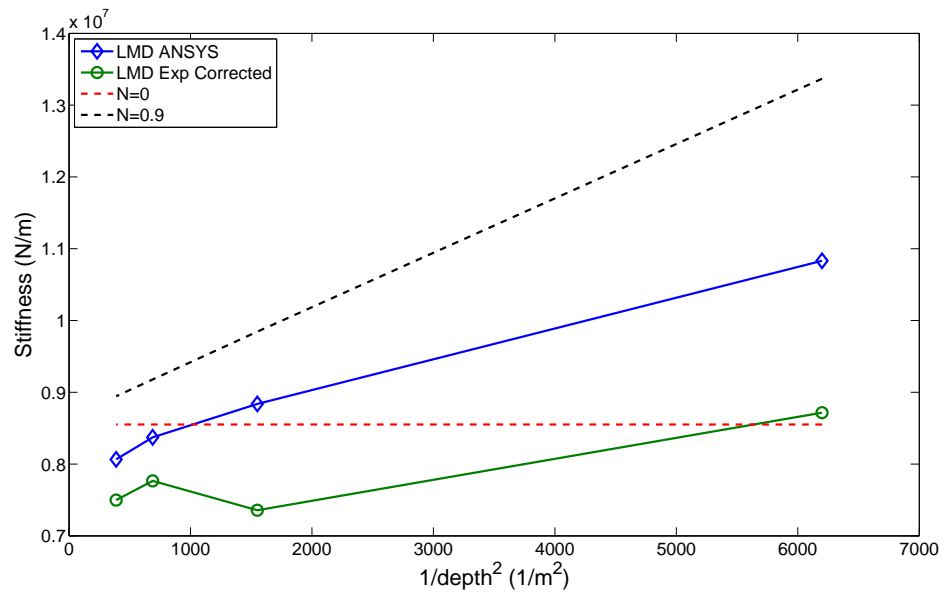


Figure 5.6: *Stiffness against $1/\text{depth}^2$ for LMD beams at $L/d = 5.67$. Comparing discrete detail ANSYS and experimental results corrected for test rig flexure against classical solution*

ment between the ANSYS and corrected experimental results and the departure from the expected range of results based upon the plane stress micropolar numerical solutions for the bending problems. It is possible that the lack of agreement between the ANSYS and corrected experiments, particularly at the shorter spans may be due to local plastic deformation, of the beam test pieces, at the supports; this was evident on examination. If this were the case then the larger depths would be in better agreement, with the ANSYS model, than that of the smaller depths. This is indeed born out in the LMD results but not in the HMD. The LMD test pieces have less matrix material and therefore a greater local deformation around each void may account for this difference between the HMD and LMD.

There is a departure from the expected range for shorter spans which is greater in the lower density material. Based upon the slender beam work, it would appear that the intercept with the vertical axis is not consistent between the different spans implying that there is apparently a size dependent variation in the flexural modulus. This is, however, not predicted in micropolar elasticity as the flexural modulus is size independent. It is possible that, at the shortest span, the number of voids to overall geometry size is too small to rely upon a micropolar continuum description. Alternatively, using the flexural modulus as the isotropic Young's modulus, in the plane stress formulation, may not be appropriate. As previously highlighted the material is anisotropic and therefore the isotropic assumptions made in the plane stress formulation may not hold for this material. The orthotropic Young's modulus, for both materials, is reduced in the through depth direction. With increasing transverse shear in the shorter spans this change in modulus would have a greater effect. This reduction in modulus is greatest for the LMD material which would explain the greater departure from the expected behaviour at lower density.

These results do, however, show that the material is not behaving in a couple stress manner as the nonlinear shape of the plots imply that the coupling number clearly lies between 0 and 1. With test data at shorter spans, from both the detailed ANSYS and experimental results, the CV-MPLST will now be used in an iterative search procedure to find the coupling number for this model material.

5.2 Iterative Constitutive Code

The iterative determination of constitutive properties is classed as an inverse problem, where the response of the material is known but the necessary input parameters, constitutive properties or boundary conditions, to gain the known response are themselves unknown. The applications and types of inverse procedures is broad. They have been used in solid mechanics, in nondestructive testing to identify cracks in materials and determining buckling loads [50]. The finite element method has been used in inverse procedures to identify material constitutive properties using experimental data from miniature dumb-bell test specimens [51] and small scale punch tests [52].

The intention of this inverse approach is to take the experimental stiffness data for all three different spans and compare them against solutions gained from the CV-MPLST code using estimated constitutive properties particularly the coupling number, N . Based upon a measure of fit between these two solutions, the constitutive properties are updated, in an iterative procedure, until a desired agreement is reached. What will follow is an example of this procedure when applied to the HMD ANSYS experimental results. The HMD ANSYS results are used as they are the most consistent data, lying within the bounds of micropolar elasticity at all spans.

5.2.1 Procedure

The iterative procedure has been developed in MATLAB and has been created to be generic for any set of stiffness data as long as the span and depths are defined. This code can be seen in appendix C. Initially, a straight line regression is fitted to the stiffness data at $L/d = 10.08$ to gain an initial estimate of the micropolar flexural modulus E_{fm} and couple modulus γ . This is identical to the procedure used in chapter 3 for the slender beams. In this analysis, the Poisson's ratio is set to 0.3. Next, using the stiffness data at $L/d = 5.04$, an iterative loop is begun to determine the coupling number N . This is carried out by first taking an initial guess for N and calculating the numerical stiffness solutions produced

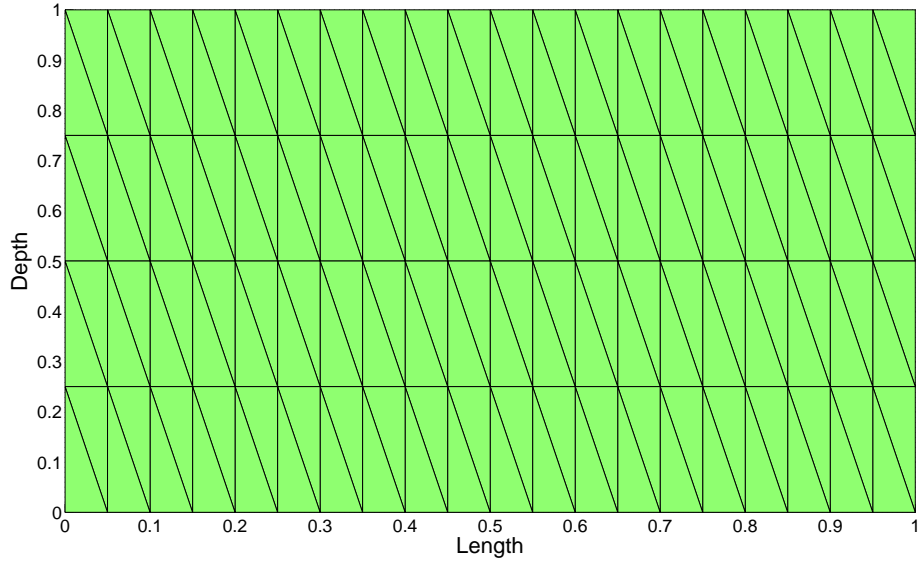


Figure 5.7: *Unit mesh used for HMD $L/d=10.08$*

by the CV-MPLST code at this span using the initial constitutive data. This stiffness data will be termed the model stiffness data. The mesh used in this analysis is of the form shown schematically in figure 5.7, 20 x 4 (length x depth) elements at $L/d = 10.07$, 15 x 4 elements at $L/d = 7.56$ and 10 x 4 elements at $L/d = 5.04$. Due to the varying depths, at different spans, the actual nodal coordinates were gained by appropriately scaling an array of normalised nodal coordinates, with divisions varying from 0 to 1 as seen in figure 5.7, by the depth for the vertical coordinates and by the length for the horizontal coordinates. The number of elements used is based upon the convergence tests in chapter 4. For each span the number of elements along the length is reduced. This is to ensure that a similar element aspect ratio is maintained for all the spans.

Once the initial model stiffness data has been determined this can be compared against the ANSYS data to gain a measure of how well the two sets of data fit. This is done by calculating the coefficient of multiple determination, R^2 . The coefficient of multiple determination is a ratio of the sum of the squared residual

errors SS_{err} and the sum of the squared total errors SS_{tot} [53] which is defined as

$$R^2 = 1 - \frac{SS_{err}}{SS_{tot}} \quad (5.1)$$

where the sum of the squared residual errors are

$$SS_{err} = \sum (K_A - K_M)^2 \quad (5.2)$$

and the sum of the squared total errors are

$$SS_{tot} = \sum (K_A - \bar{K}_A)^2 \quad (5.3)$$

where K_A is the ANSYS stiffness data, K_M is the model stiffness data and \bar{K}_A is the mean of the ANSYS experimental stiffness data. The sets of data are said to be the same when R^2 equals 1. A target value for R^2 is predefined which will be slightly less than 1 and if this is not reached then a new guess for N will be made using the following update rule. The update rule is

$$D_{i+1} = \left[\frac{1}{n} \sum_{i=1}^n \frac{K_A}{K_M} \right] D_i \quad (5.4)$$

where D is the constitutive property to be changed, K_A and K_M have the same meaning as above, n is the number of data points (in this case corresponding to the four depths) and subscript i denotes the current constitutive value and $i + 1$ denotes the updated constitutive property. This procedure is repeated and after repeated iterations the R^2 value should converge to 1. This is repeated until R^2 is greater than or equal to the target, in this case $R^2_{target} = 0.99$, or R^2 begins to diverge away from 1 which would indicate that the correlation between the model data and the ANSYS data is reducing. Applying this iterative procedure for N to the stiffness data for $L/d = 5.04$ the right hand graph shown in figure 5.8 is gained. The iterative loop is broken at $R^2 = 0.93$ as the solution began to diverge, returning $N = 0.112$. It can be seen that there is reasonable agreement for this aspect ratio as expected since this was the data to which the fit was being applied. When, however, this value of N is used to determine the stiffness variation for the two longer spans the fit to the ANSYS data is less satisfactory

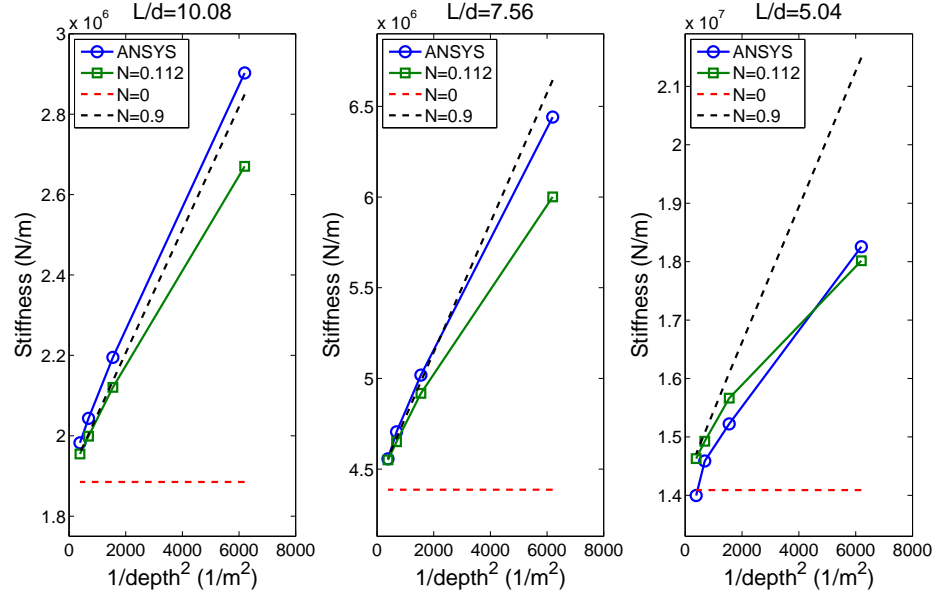


Figure 5.8: Best fit solutions for HMD samples based upon the ANSYS results at the three different spans after the first iteration to find the coupling number N using $L/d = 5.04$, $R^2 = 0.93$ at this span

as shown in the left and central graphs of figure 5.8.

An update of the couple modulus γ is therefore required to bring about a better fit for $L/d = 10.08$ and $L/d = 7.56$. This is required since at $L/d = 10.08$ some shear deformation is actually occurring implying that the initial straight line fit, assuming a slender beam, is slightly incorrect and would not give the precise couple modulus. The same iterative procedure is now repeated to find a value of γ that offers a good correlation at $L/d = 10.08$. A flow diagram of this full iterative procedure is shown in figure 5.9. Again the target is defined as $R^2 = 0.99$ and in this case it is reached. The updated results now show a good agreement for $L/d = 10.08$ and $L/d = 7.56$, figure 5.10. The fit, however, at $L/d = 5.04$ is now slightly reduced, figure 5.10. It is clear from these results that it is not possible to get an exact fit for all the spans using the same constitutive properties, suggesting that this material is not adequately described by isotropic plane stress micropolar elasticity. Nevertheless an excellent correlation is gained for the $L/d = 7.56$ results without using them in the iterative procedure. This would indicate that the progression from $L/d = 10.08$ to $L/d = 7.56$ is properly

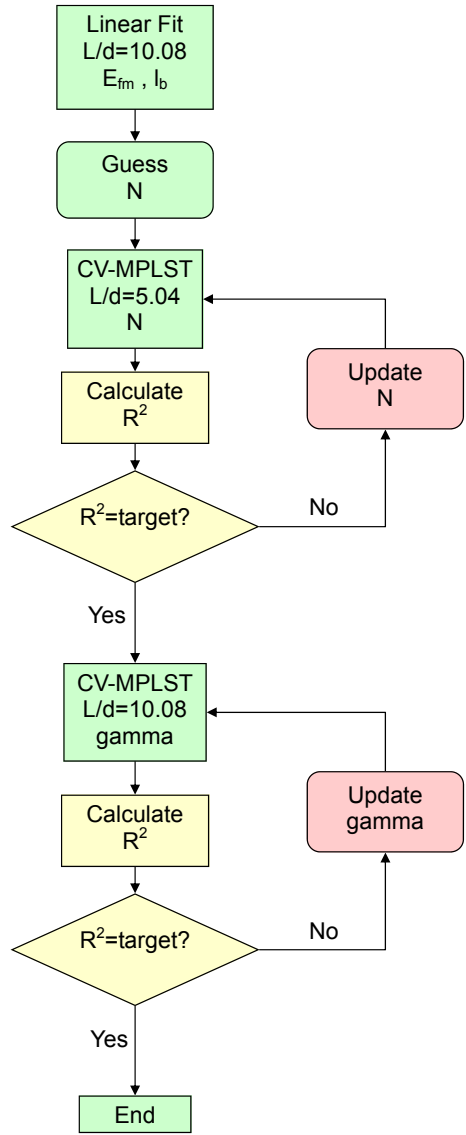


Figure 5.9: Flow chart showing iterative process to find the best fit material parameters for the HMD model material

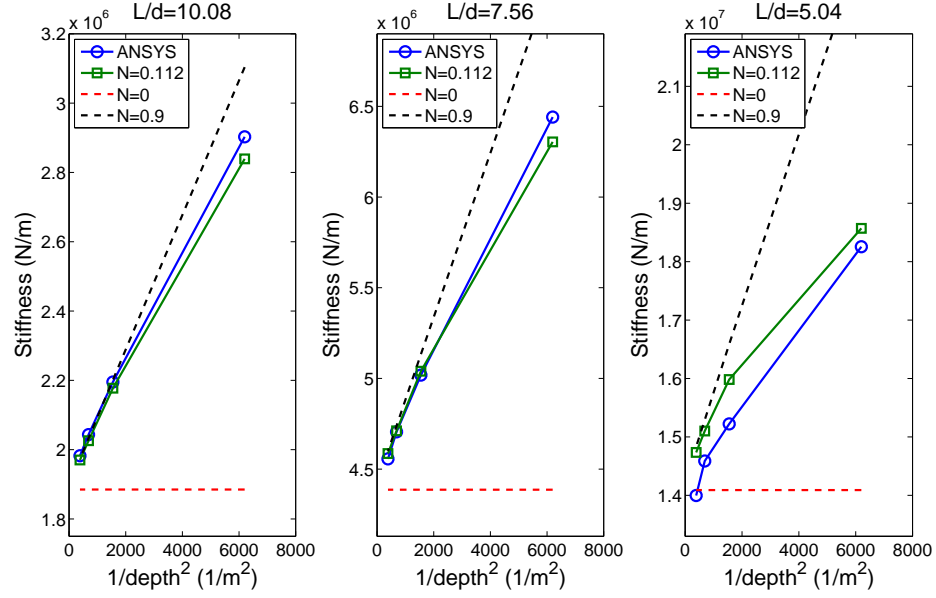


Figure 5.10: Best fit solutions for HMD samples based upon the ANSYS results at the three different spans after the second iteration to find the couple modulus γ using $L/d = 10.08$, $R^2 = 0.99$ at this span

described by micropolar elasticity. The final constitutive data obtained for the HMD ANSYS results are therefore $E_{fm} = 3.9\text{e}10\text{N}/\text{m}^2$, $N = 0.112$, $\gamma = 3.339\text{e}5\text{N}$ and therefore $l_b = 10.14\text{mm}$.

The only constitutive property, used in this analysis, which has not been determined directly for this material from experimental tests, is Poisson's ratio. To ensure that any mismatch between the calculated values and the experimental value is not due to the assumption of a Poisson's ratio value of $v_m = 0.3$, a parameter study of how changing Poisson's ratio would change the solution value at each span was carried out. Poisson's ratio was changed by $\pm 15\%$ and the change in stiffness calculated. This can be seen for the three spans in figure 5.11. The results are normalised against the stiffness gained at each span with $v_m = 0.3$. The greatest variation in stiffness is at the shorter spans. This change, however, is only 0.6% at its greatest. This would not account for the larger departure seen in fitting the model material data. To further check, Poisson's ratio was calculated from a simulated tensile test in ANSYS. It was estimated at 0.33 for both orthogonal directions which is within the $\pm 15\%$ considered.

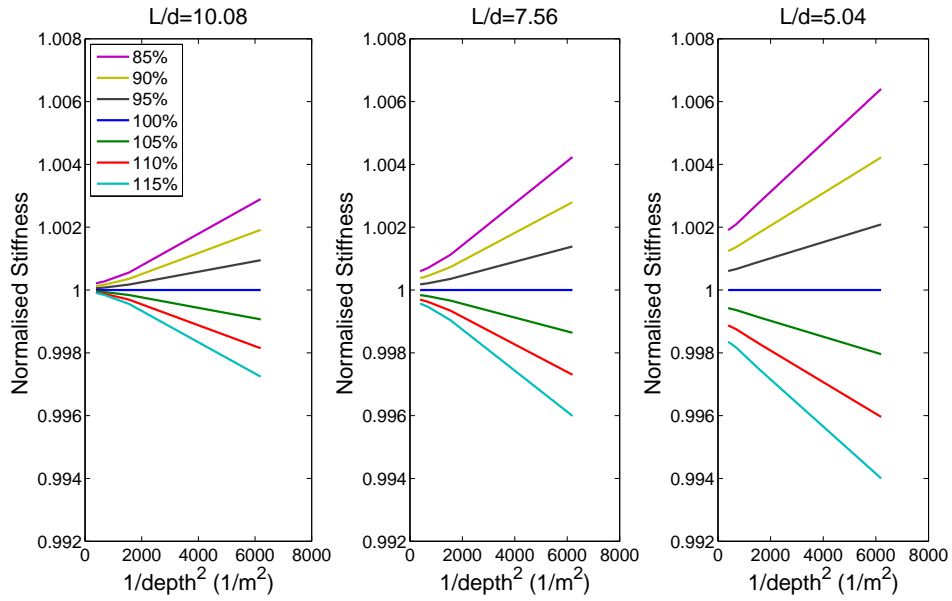


Figure 5.11: Variation of stiffness for $\pm 15\%$ Poisson's ratio for different spans HMD

It is clear that this model material does exhibit a size effect in bending and that it can be described by a micropolar material model at certain spans and void configurations. There is, however, additional material behaviour, particularly at shorter spans, that suggests that micropolar elasticity cannot fully describe the deformation. Whether this observed behaviour indicates experimental error, numerical error or is due to material anisotropy is unclear.

In the following chapter, the same iterative procedure set out in this chapter will be used to determine the constitutive properties from model heterogeneous thick and thin walled diametrically loaded rings. These rings are made from a different material and have an underlying structure that is four times smaller than the beams tested in this chapter. They do, however, show similar trends as seen for the aluminium model material tested in three point bending.

Chapter 6

Model Material - Diametrically Loaded Ring

This chapter presents the determination of plane stress micropolar constitutive properties, flexural modulus, characteristic length and coupling number, from thin and thick walled diametrically loaded rings. Ring samples can have an advantage over rectangular beams as many natural materials have microstructures arranged in radial patterns. For example the growth rings and sap channels of balsa wood or the structure of human bone. From the outset it should be noted that the experimental results used in this chapter were not obtained by the author. Limited attention, therefore, will be given over to explaining the design and execution of the experiment. The constitutive properties obtained, however, are of significance as they show similar trends to that of the model aluminium beams.

Ring test pieces of mean radius R and wall depth d , see figure 6.1, were machined from 6 mm thick Altuglas[®] acrylic sheet. The acrylic sheet has a flexural modulus at 23°C of 3.25 GPa and a Poisson's ratio of 0.39 at 20°C [54]. Two different ring aspect ratios, R/d , were manufactured. The first aspect ratio was $R/d = 8$ and the second was $R/d = 4$. At each aspect ratio there were four different wall depths. This led to eight different sized ring samples. The voids are arranged in a hexagonal pattern, similar to that of the beams in the previous chapters. The

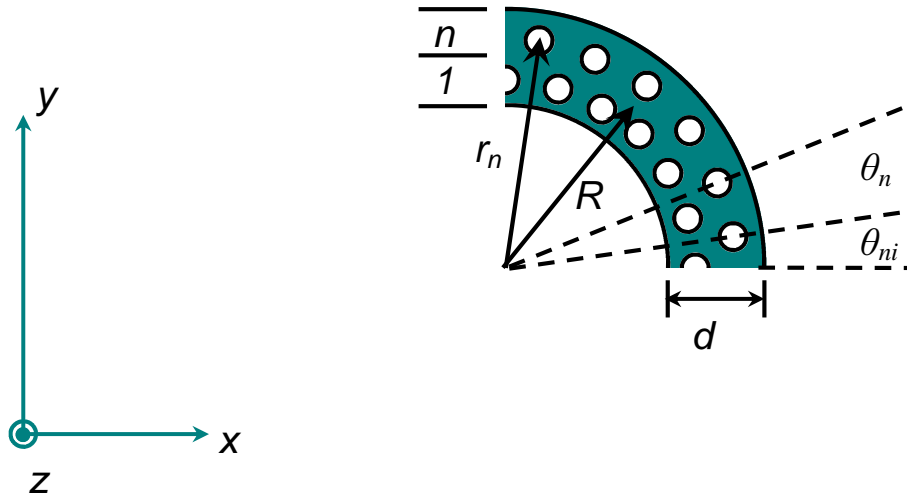


Figure 6.1: Model ring of radius R and depth d with radial void distribution dimensions of pitch n , pitch radius r_n , initial offset angle θ_{ni} and offset angle θ_n

specific positioning of the circular voids, of radius $r=0.79275$ mm, is controlled by the radial pitch number n ; this being the number of voids through depth, and is specific for each of the eight ring samples. At each pitch number, a pitch radius r_n defines the distance from the centroid of the ring to the centre of the void. Also defined are two angles. The first gives the initial offset angle θ_{ni} from the horizontal axis to the centre of the first void. The second angle defines the offset angle θ_n between adjacent voids. These dimensions are shown in table 6.1 for all eight ring samples.

The model rings were loaded diametrically in tension, within the elastic region, and the resulting force displacement curves are used to obtain the ring stiffnesses. These stiffness can be seen in table 6.2. It is clear from table 6.2 that there is a size dependent stiffening. Diametrically loaded rings are similar to straight beams in bending, in that if they were behaving in a classically elastic manner the stiffnesses would have remained constant as the aspect ratio is constant.

Table 6.1: *Geometric data for ring samples*

Ring No.	Radius, R (mm)	Depth, d (mm)	R/d	Pitch Number, n	Pitch Radius r_n (mm)	Initial Offset Angle, θ_{ni} (degrees)	Offset Angle, θ_n (degrees)
1	12.7	3.175	4	1	12.7	0	18
2	25.4	3.175	8	1	25.4	0	9
3	25.4	6.35	4	1	23.8125	0	9
				2	26.9875	4.5	9
4	50.8	6.35	8	1	49.2125	0	4.5
				2	52.3875	2.25	4.5
5	38.1	9.525	4	1	34.925	0	6
				2	38.1	3	6
				3	41.275	0	6
6	76.2	9.525	8	1	73.025	0	3
				2	76.2	1.5	3
				3	79.375	0	3
7	63.5	15.875	4	1	57.15	0	3.6
				2	60.325	1.8	3.6
				3	63.5	0	3.6
				4	66.675	1.8	3.6
				5	69.85	0	3.6
8	127	15.875	8	1	120.65	0	1.8
				2	123.825	0.9	1.8
				3	127	0	1.8
				4	130.175	0.9	1.8
				5	133.35	0	1.8

Table 6.2: *Experimental stiffness results, K , for ring samples at two aspect ratios; $R/d = 8$ and $R/d = 4$*

Depth (mm)	$K_{R/d=8}$ (N/m)	$K_{R/d=4}$ (N/m)
3.175	16.248e3	107.880e3
6.350	13.719e3	90.600e3
9.525	12.399e3	82.634e3
15.875	11.664e3	82.619e3

6.1 Constitutive Properties

The iterative search procedure is now used to fit the micropolar constitutive properties to this experimental data in order to discover the flexural modulus E_{fm} , characteristic length of bending l_b and the coupling number N . To gain an initial estimate of the flexural modulus and the characteristic length, the analytical solution for a thin walled ring, see section 2.3.2, is used to fit a straight line to the experimental data for $R/d = 8$. The iterative procedure is now begun following the flow process set out in figure 6.3 with a target coefficient of determination of $R_{target}^2 = 0.99$. The final constitutive properties are $E_{fm} = 1.82e9\text{N/m}^2$, $N = 0.08$, $\gamma = 834.64\text{N}$, $l_b = 2.345\text{mm}$. A Poisson's ratio of 0.39 was assumed. A plot of the experimental results compared against the best fit stiffnesses gained from the iterative procedure can be seen in figure 6.2. It is immediately clear, once again, that the search procedure is unable to fit plane stress micropolar elastic behaviour exactly to both the ring aspect ratios. This corroborates the suspicion of the previous chapter, that the anisotropic natures of these model materials are not being captured correctly, particularly at smaller aspect ratios, by plane stress isotropic micropolar elasticity. This work does, however, show some interesting similarities between the constitutive properties obtained from the rings and the rectangular beams.

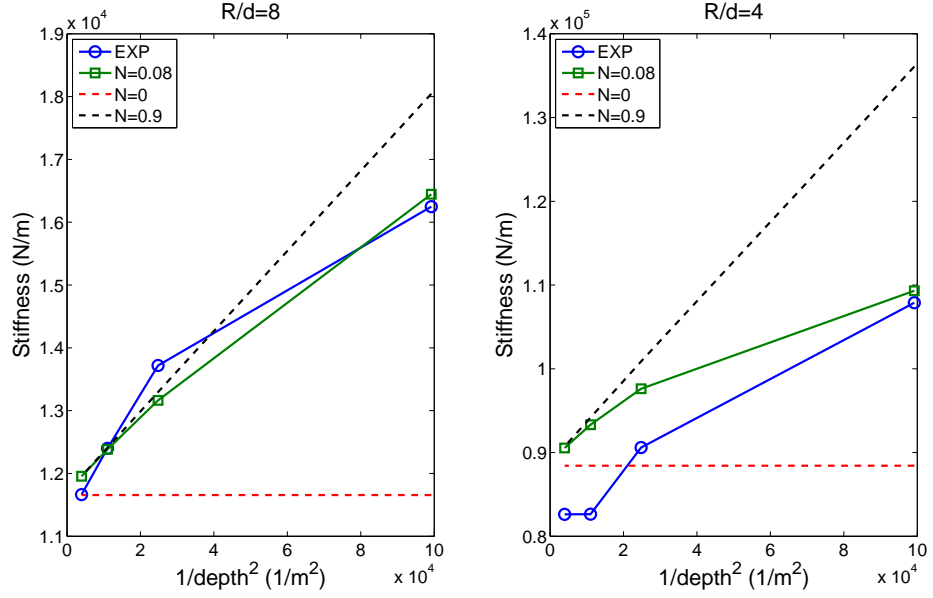


Figure 6.2: Best fit solution for ring samples based upon experimental stiffness results

6.2 Discussion

Comparing the constitutive properties gained for the HMD ANSYS data and the experimental rings show remarkable similarities considering the differences in geometry and the fact that the ANSYS data is an idealisation while the ring results are obtained from experiment. Geometrically the ring samples are approximately four times smaller than the rectangular beams and the elastic modulus of the matrix material is twenty times smaller in the acrylic rings. Although the rings are at a different scale to the rectangular beams, the relative hole pattern is very similar. This results in three similarities that are noteworthy. The first is the similarity of coupling number. For the HMD beam samples a coupling number of $N = 0.11$ was obtained and a coupling number of $N = 0.08$ was obtained for the rings. Secondly the ratio of matrix modulus to micropolar flexural modulus is very similar. In both the rectangular beams and the rings, the micropolar flexural modulus is approximately 56% of the matrix modulus. This is to be expected as a similar proportion of material is removed, in a geometrically similar manner, in both cases. Thirdly and most significantly the ratio of the void radius to

the characteristic length is almost identical. In both cases the radius is approximately 34% of the characteristic length. These similarities are important as the trends are preserved for a similar hole pattern but at a different scale and matrix material properties. They are also gained through testing different geometries under different loading conditions. This consistency implies that the micropolar material properties are intrinsic for a given microstructure.

This chapter has shown that although different testing geometries and matrix materials are used consistent constitutive properties are obtained. This highlights the applicability of micropolar elasticity, particularly at larger aspect ratios, in capturing size effects in bending.

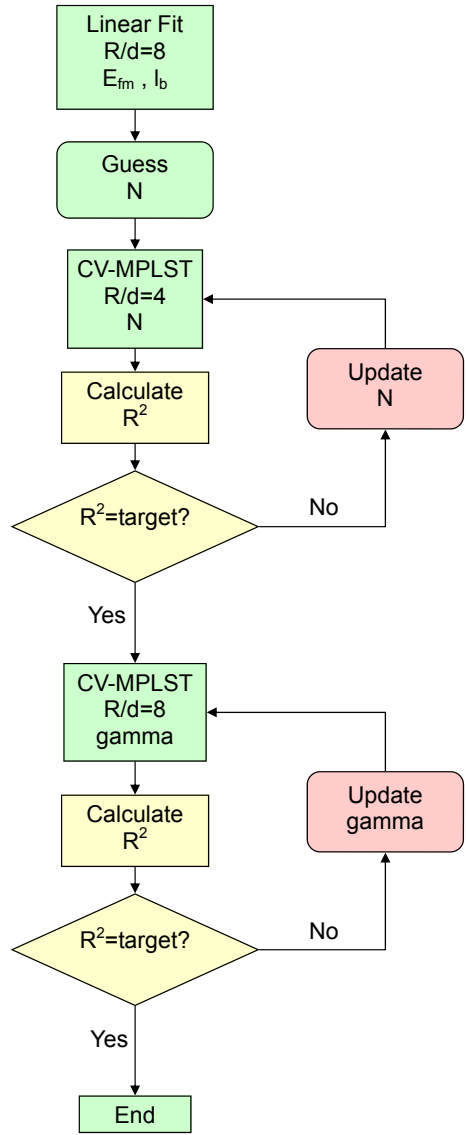


Figure 6.3: Flow chart showing iterative process to find the best fit material parameters from the model ring experimental results

Chapter 7

Summary and Conclusions

A model material has been created that shows distinctive size stiffening when tested in three point bending. Constitutive properties namely, micropolar flexural modulus and characteristic length of bending, have been identified that are logical; the characteristic length is of the same order as the microstructure and the flexural modulus is reduced below that of the matrix material. A slender micropolar beam finite element, whose solution convergence is insensitive to variations in characteristic length, is able to replicate the slender beam deformation using the constitutive properties already identified thus allowing its use in analysing more complex space frame structures. A plane stress and plane strain micropolar control volume finite element has been developed that has equivalent or better accuracy over its equivalent finite element. The formulation is based upon a code frame work developed for a control volume finite element discrete Kirchhoff plate bending element that utilises the symbolic mathematics kernel of MATLAB to determine the element stiffness matrix in a quadrature free routine. The use of quadrature free elements allows an accurate and direct comparison between the competing finite element and control volume methods. The increased geometric versatility of the plane stress CVFEM enables its use in predicting the deformation of deep micropolar beams in bending using the constitutive properties gained from the slender beams. The development of the CVFEM has allowed the sensitivity of the size stiffening effect upon the coupling number, in thicker beams, to be quantified. Subsequently this is used in an iterative procedure that

allows the inverse identification of the coupling number and the update of the characteristic length for the HMD material. Applying the procedure, however, to the LMD material to identify the coupling number has not been possible because of inconsistency in the experimental data. The most likely cause of which is material anisotropy and its incompatibility with the isotropic material model. The inverse procedure has also been used to fit material data to ring samples, at a different scale to the model aluminium beams. This again showed that material anisotropy is an issue but it did, however, show that there is consistency to the micropolar material properties obtained that is unaffected by changes to geometry, bulk material properties and scale.

Real Materials

Ultimately it should be the goal of any work with heterogeneous materials modelling to be able to accurately replicate the deformation of a real material with random inclusions. Real materials, however, offer additional challenges over and above those of model materials. These challenges are associated with the experimental determination of the constitutive properties. Some heterogeneous materials have large void volume fractions and therefore less matrix material. This means that the ability to carry load is reduced and thus these materials require to be tested at relatively low loads. In addition, the voids tend to be smaller than those in the model material used here. These two features mean that standard materials testing equipment is not well suited to testing these materials as small load cells and an increased accuracy of displacement measurement is required. Often at this scale the micro size effects are small and may be masked by frictions and local loading effects in the testing procedures as already noted in the literature [12]. Further to this, surface damage, which occurs when the samples are machined, will artificially reduce the materials ability to carry load. Both these effects have been noted in the literature before but should be highlighted as an issue. Custom testing equipment can be manufactured that is sensitive enough to detect the size effects however the effect of surface damage is not so easily rectified. A greater understanding of the relationship between microstructural geometry and size effects would be of great benefit when apply generalised

models to heterogeneous materials and the study of model materials can help in this.

Future Work

In this work the use of a model material has offered some unique opportunities over a real material. It has given the opportunity to test at a larger scale, magnifying the size effect so that it can be identified, without doubt, on standard mechanical testing equipment. With the model material's simplified microstructure it has been possible to simulate it in full geometric detail in ANSYS. This has allowed a validation of the experiments and opened up future work. Indeed the agreement between the HMD ANSYS models and the experiments is sufficiently good to allow future studies using ANSYS alone. These studies can shed light upon: the role of material anisotropy, the relationship between microstructural geometry and constitutive properties, the role of surface damage and at what scales generalised elastic models are applicable.

An understanding of the microstructure's role upon the constitutive properties would be very informative in the understanding of heterogeneous materials. Investigations into void volume fraction, void packing arrangements, including material anisotropy, and void compliance could allow the development of empirical rules that explain how the alteration of the above parameters change the constitutive properties. First and foremost this could extend the understanding of the characteristic length beyond the loose definition that it should be in the order of the microstructure and exposing voids at the surface of a model material will be beneficial to the understanding of surface damage effects in real materials. It could be envisaged that a model material be made that has an engineered microstructure, controlling void size and distribution during manufacture, to deliver enhanced structural properties.

It is also clear from this work that a micropolar continuum is not applicable in all cases. It has been proposed that the lack of agreement between numerical solutions and experimental results is due to material anisotropy, however, an additional phenomenon may be at work. With a heterogeneous material there

will be transitions, at certain length scales, between continuum models. The first transition is from classical to generalised elastic behaviour. This change is described in generalised continua by the length scale constitutive parameter. There is, however, another transition. Micropolar elasticity predicts a stiffness approaching infinity as the geometric size is reduced; this, however, is unphysical. This is demonstrated in the current work as the smallest beam geometry, one hole through thickness, is the smallest beam that would preserve the detail of the microstructure and therefore it represents an upper bound for the micropolar bending stiffness. This demonstrates a geometric limit to the micropolar description of this model material. Local effects, introduced by loading and boundary conditions may also affect where this limit exists. Model material simulations would shed light upon this.

Concluding Remarks

Returning to the specific question of this thesis: ‘is a micropolar elastic continuum a feasible modelling approach in computational structural mechanics to capture the deformation of a heterogeneous material?’, it is clear from this work that it is capable of capturing the size effect in the model material; however, its applicability breaks down for smaller aspect ratios. Further work is required to define its limits.

Heterogeneous materials have many beneficial structural properties, however, quantifying and replicating this in generalised elastic models is difficult. The real difficulty lies where, in trying to observe and quantify the phenomena, it is being obscured: the chosen testing procedure may damage the material in preparation and therefore render the test erroneous or the test itself may have inaccuracies that mask or add to the material deformation. Conversely, the test procedure may be sound but the chosen generalised elastic theory is not endowed with enough degrees of freedom to properly describe the material response; as might be the case for the model material presented here. In any likelihood it will be a combination of all these factors and it will be up to individual judgment as to whether an adequate description has been gained from a generalised elastic model.

Appendix A

Discrete Kirchhoff Triangular Element

A.1 Mindlin Plate Bending Theory

A.1.1 Deformations

According to Mindlin plate theory a straight line normal to the midsurface of the plate, in an undeformed configuration, figure A.1 (a) , is assumed to remain straight when the plate is loaded but not necessarily normal to the midsurface, as shown in figure A.1 (b). This allows for transverse shear deformation of the plate. This deformation is due to the rotations θ_x and θ_y of lines that are normal to the midsurface of the undeformed plate. Thus the strain-displacement relationships for small angles of rotation are

$$\begin{aligned} u &= -z\theta_x & \epsilon_x &= -z\theta_{x,x} & \gamma_{xy} &= -z(\theta_{x,y} + \theta_{y,x}) \\ v &= -z\theta_y & \epsilon_y &= -z\theta_{y,y} & \gamma_{yz} &= w_{,y} - \theta_y \\ & & & & \gamma_{zx} &= w_{,x} - \theta_x \end{aligned} \tag{A.1}$$

and therefore the bending strains ϵ_b are related to curvatures thus

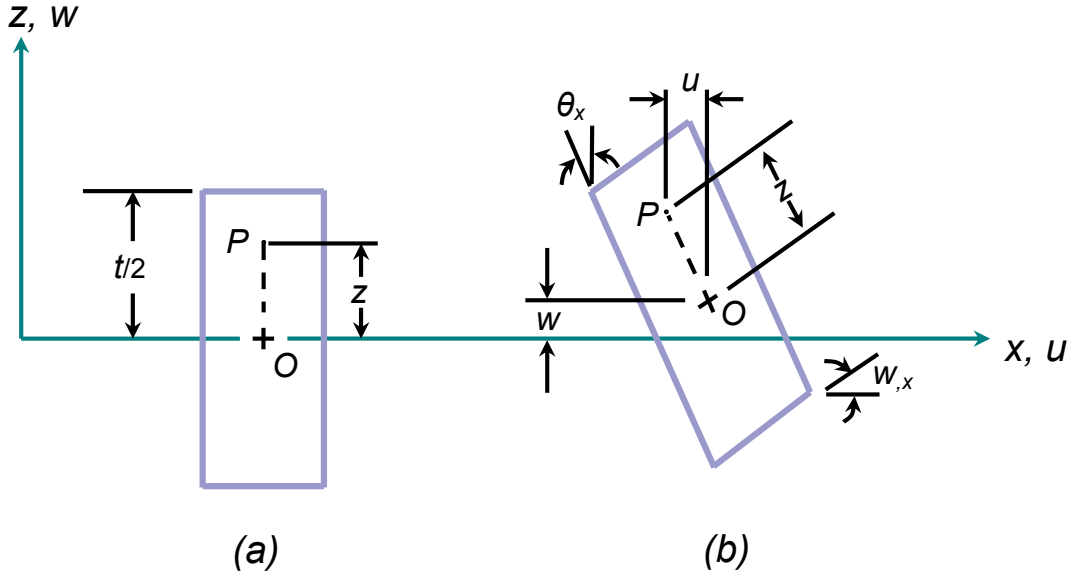


Figure A.1: *Differential plate element undeformed (a) and deformed plate(b)*

$$\epsilon_b = \begin{Bmatrix} \epsilon_x \\ \epsilon_y \\ \gamma_{xy} \end{Bmatrix} = -z \begin{Bmatrix} \theta_{x,x} \\ \theta_{y,y} \\ \theta_{x,y} + \theta_{y,x} \end{Bmatrix} \quad (\text{A.2})$$

A.1.2 Moment Curvature Relations

The curvature vector χ is given by

$$\chi = \begin{Bmatrix} \theta_{x,x} \\ \theta_{y,y} \\ \theta_{x,y} + \theta_{y,x} \end{Bmatrix} \quad (\text{A.3})$$

while the bending moments per unit length are related to the curvature vector by

$$\mathbf{M} = \mathbf{D}\chi \quad (\text{A.4})$$

where \mathbf{M} is the bending moment vector

$$\mathbf{M} = \begin{Bmatrix} M_x \\ M_y \\ M_{xy} \end{Bmatrix} \quad (\text{A.5})$$

\mathbf{D} is the constitutive matrix

$$\mathbf{D} = \frac{Eh^3}{12(1-\nu^2)} \begin{bmatrix} 1 & \nu & 0 \\ \nu & 1 & 0 \\ 0 & 0 & \frac{1-\nu}{2} \end{bmatrix} \quad (\text{A.6})$$

and E is Young's modulus, ν is Poisson's ratio and h is the plate thickness.

A.1.3 Equilibrium

The equilibrium equations for the plate midsurface are

$$\begin{aligned} T_{x,x} + T_{y,y} &= -pA \\ M_{x,x} + M_{xy,y} - T_x &= 0 \\ M_{xy,x} + M_{y,y} - T_y &= 0 \end{aligned} \quad (\text{A.7})$$

where T are shear forces per unit length and p is a transverse distributed load per unit area acting on the midsurface of area A .

A.2 DKT Element

The formulation of the DKT element begins with a straight edged triangle with 3 vertex and 3 midside nodes, figure A.2 (a). The rotations θ_x and θ_y within the element are interpolated using a complete polynomial for the nodal degrees of freedom, θ_{xi} and θ_{yi} where $i = 1, 6$ refer to the element nodes.

$$\theta_x = \sum N_i \theta_{xi} \quad \theta_y = \sum N_i \theta_{yi} \quad (\text{A.8})$$

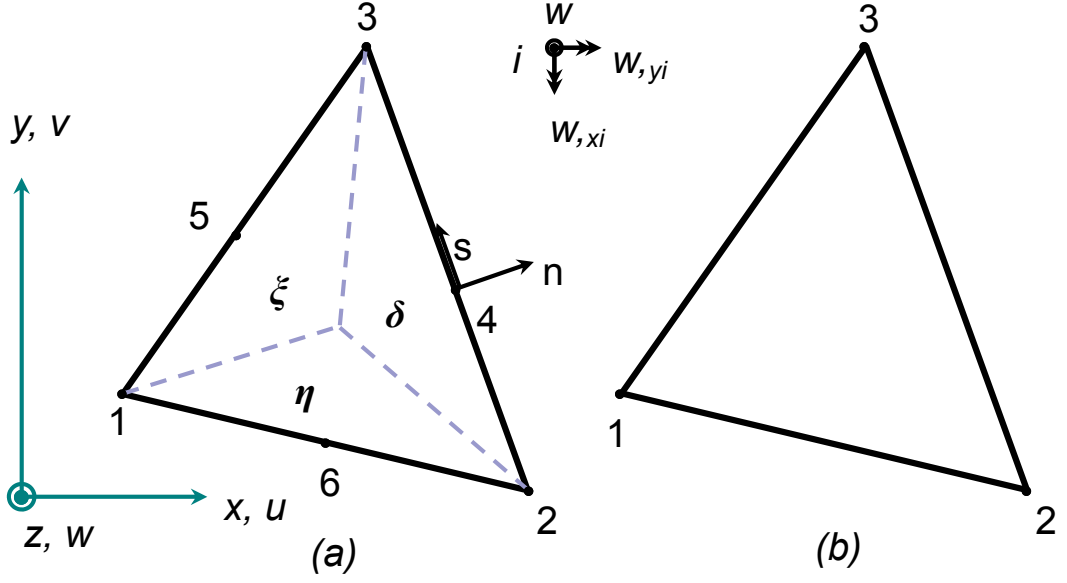


Figure A.2: Transition to the DKT element. (a) 6 noded Mindlin element with the triangular area coordinates δ , ξ and η . (b) 3 noded DKT element with vertex node degrees of freedom (w_i , $w_{,xi}$, $w_{,yi}$)

The shape functions $N_i(\xi, \eta)$ for the quadratic interpolations, where $\delta = (1 - \xi - \eta)$, are

$$\begin{aligned}
 N_1 &= 2(1 - \xi - \eta)\left(\frac{1}{2} - \xi - \eta\right) \\
 N_2 &= \xi(2\eta - 1) \\
 N_3 &= \eta(2\xi - 1) \\
 N_4 &= 4\xi\eta \\
 N_5 &= 4\eta(1 - \xi - \eta) \\
 N_6 &= 4\xi(1 - \xi - \eta)
 \end{aligned} \tag{A.9}$$

ξ and η being the usual natural coordinates of the element [55]. The transverse displacement along the element sides are prescribed by a cubic function in the edge tangent coordinate s , giving the edge tangent slope as:

$$w_{,sk} = -\frac{3}{2l_{ij}}w_i - \frac{1}{4}w_{,si} + \frac{3}{2l_{ij}}w_j + \frac{1}{4}w_{,sj} \tag{A.10}$$

where k denotes the midside node of the element edge that connects nodes i and j and is of length l_{ij} .

An element with nine degrees of freedom, figure A.2 (b), is sought where the rotations θ_x and θ_y are expressed in terms of the vertex node degrees of freedom, w_i , $w_{,xi}$ and $w_{,yi}$. For the triangular element, the full displacement vector is

$$\mathbf{d} = [w_i \quad w_{,yi} \quad -w_{,xi}]^T \quad \text{for } i = 1, 2, 3 \quad (\text{A.11})$$

This is achieved by applying the following constraints.

1. Transverse shear strains γ_{yz} and γ_{zx} vanish at the vertex nodes. From (A.1)

$$\theta_{xi} = w_{,xi} \quad \text{and} \quad \theta_{yi} = w_{,yi} \quad \text{for } i = 1, 2, 3 \quad (\text{A.12})$$

2. Transverse shear strain γ_{sz} vanishes at the mid side nodes

$$\theta_{sk} = w_{,sk} \quad \text{for } k = 4, 5, 6 \quad (\text{A.13})$$

3. Normal rotations vary linearly along the element edge in the edge normal coordinate n

$$\theta_{nk} = \frac{1}{2}(w_{,ni} + w_{,nj}) \quad \text{for } k = 4, 5, 6 \quad (\text{A.14})$$

where k denotes the midside node of the element side connecting nodes i and j .

On applying the discrete Kirchhoff constraints the vectors \mathbf{H}_x and \mathbf{H}_y are obtained as new shape functions relating element rotations, θ_x and θ_y , to the desired element displacement vector (A.11) [55].

$$\begin{aligned} \theta_x &= \mathbf{H}_x^T(\xi, \eta)\mathbf{d} \\ \theta_y &= \mathbf{H}_y^T(\xi, \eta)\mathbf{d} \end{aligned} \quad (\text{A.15})$$

From equations (A.3) and (A.15) the moment curvature transformation matrix \mathbf{B} can be obtained

$$\boldsymbol{\chi} = \mathbf{B}\mathbf{d} \quad (\text{A.16})$$

where B is

$$\mathbf{B}(\xi, \eta) = \frac{1}{2A} \begin{bmatrix} y_{31}\mathbf{H}_{x,\xi}^T + y_{12}\mathbf{H}_{x,\eta}^T \\ -x_{31}\mathbf{H}_{y,\xi}^T - x_{12}\mathbf{H}_{y,\eta}^T \\ -x_{31}\mathbf{H}_{x,\xi}^T - x_{12}\mathbf{H}_{x,\eta}^T + y_{31}\mathbf{H}_{y,\xi}^T + y_{12}\mathbf{H}_{y,\eta}^T \end{bmatrix} \quad (\text{A.17})$$

In the control volume based method, the shear forces acting per unit length are also required in order to impose the proper equilibrium conditions upon the control volume. The shear forces are obtained directly from the derivative of the bending moments (A.7)

$$\mathbf{T} = \begin{bmatrix} T_x \\ T_y \end{bmatrix} = \frac{1}{2A} \begin{bmatrix} y_{31}M_{x,\xi} + y_{12}M_{x,\eta} - x_{31}M_{xy,\xi} - x_{12}M_{xy,\eta} \\ y_{31}M_{xy,\xi} + y_{12}M_{xy,\eta} - x_{31}M_{y,\xi} - x_{12}M_{y,\eta} \end{bmatrix} \quad (\text{A.18})$$

where

$$\begin{Bmatrix} M_x \\ M_y \\ M_{xy} \end{Bmatrix} = \mathbf{DBd} \quad (\text{A.19})$$

A.3 Element Stiffness Matrix

Both the FE and CVFE methods are founded upon the same moment curvature relationships, but the formulations differ with regards to the element stiffness matrix. In the FE-DKT element, the stiffness matrix is derived using the principle of minimum potential energy (A.20). The CV-DKT differs from this because the stiffness matrix is composed of a set of discrete equilibrium equations.

A.3.1 Finite Element Method

In the finite element method, the stiffness matrix for the DKT element is

$$\mathbf{k}_{\text{FEM}} = 2A \int_0^1 \int_0^{1-\eta} \mathbf{B}^T \mathbf{D}_b \mathbf{B} d\xi d\eta \quad (\text{A.20})$$

This equation (A.20) was symbolically integrated using the Maple kernel of MATLAB [46]. To obtain a comparison with a commercially available code the SHELL63 element of ANSYS was chosen. This is a quadratic element composed of 4 DKT elements [49] and 3 point quadrature is employed in evaluating the stiffness matrix.

A.3.2 Control Volume Finite Element Method

A dual mesh of interconnecting control volumes is set up, with each control volume centred upon a node of the finite element mesh, see figure A.3(a). The

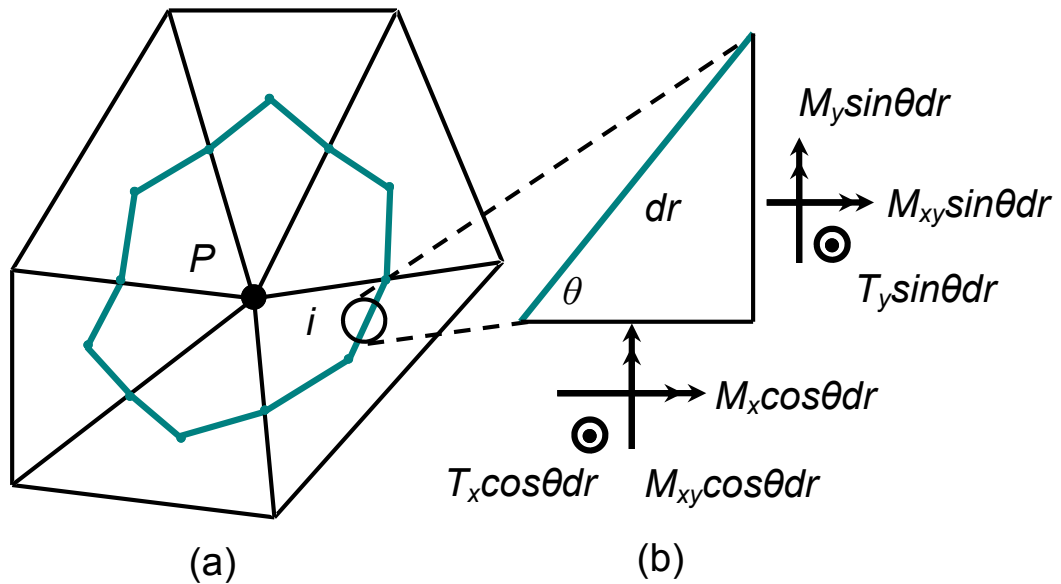


Figure A.3: (a) Control volume dual mesh centred on finite element node P (b) Equilibrium of forces acting upon a differential line dr along the control volume face

control volume faces are constructed by connecting a point midway along the finite element mesh edge to the centre of area of that corresponding finite element.

The stress resultants per unit length from equations (A.18) and (A.19), are integrated along each face of the control volume with respect to the line coordinate r , anti-clockwise around the CV node, figure A.3(b). This integration gives rise

to the stress resultants acting on each face. For a face i these are \mathbf{T}_z^i , \mathbf{M}_x^i and \mathbf{M}_y^i , representing the total transverse force and total moments about the x and y coordinates respectively. Equations (A.21), (A.22) and (A.23) are thus functions to determine the internal actions upon each face of the control volume.

Transverse Force:

$$\mathbf{T}_z^i = \int T_x \cos\theta dr + \int T_y \sin\theta dr \quad (\text{A.21})$$

Total Moment about the x-axis:

$$\mathbf{M}_x^i = \int M_y \sin\theta dr + \int M_{xy} \cos\theta dr - \int (y_r - y_i) (T_x \cos\theta dr + T_y \sin\theta dr) \quad (\text{A.22})$$

Total Moment about the y-axis:

$$\mathbf{M}_y^i = \int M_x \cos\theta dr + \int M_{xy} \sin\theta dr - \int (x_r - x_i) (T_x \cos\theta dr + T_y \sin\theta dr) \quad (\text{A.23})$$

where (x_r, y_r) are the coordinates of the moment arm along the differential line and (x_i, y_i) are the coordinates of the centre of the control volume.

As the moment curvature matrix is a function of the area coordinates a substitution of the line coordinate r for the area coordinates of the corresponding elements is made. Thus the integration of the stress resultants per unit length becomes an integration in the area coordinates, see figure A.4 (a). The substitution for each face of the control volume, within an element, is different and follows the rules set out in table A.1.

A substitution of area coordinates within the moment curvature relations is also required to perform each integration. These are based upon the geometry of the control volume face. For example in figure A.4 (b) if an integration was carried out between c and o , ξ and δ are equal to each other and due to the relationship that $\delta + \eta + \xi = 1$ it follows that $\eta = 1/2(1 - \xi)$. Table A.1 summarises these substitutions.

Equilibrium is imposed on the control volume by summing all the internal actions on each face for the control volume. The equilibrium equations can be expressed

Table A.1: *Substitutions for the discrete equation integrals and moment curvature matrix*

Direction of Integration	Integral Substitutions	Area Coordinate Substitutions in Moment Curvature Matrix, \mathbf{B}
from c to o	$\int dr = \int_0^{1/3} 3L_{oc}d\eta$	letting $\xi = 1/2(1 - \eta)$
from b to o	$\int dr = \int_0^{1/3} 3L_{ob}d\xi$	letting $\eta = 1/2(1 - \xi)$
from a to o	$\int dr = \int_0^{1/3} 3L_{oa}d\delta$	letting $\eta = \xi$ and $\eta = 1/2(1 - \delta)$

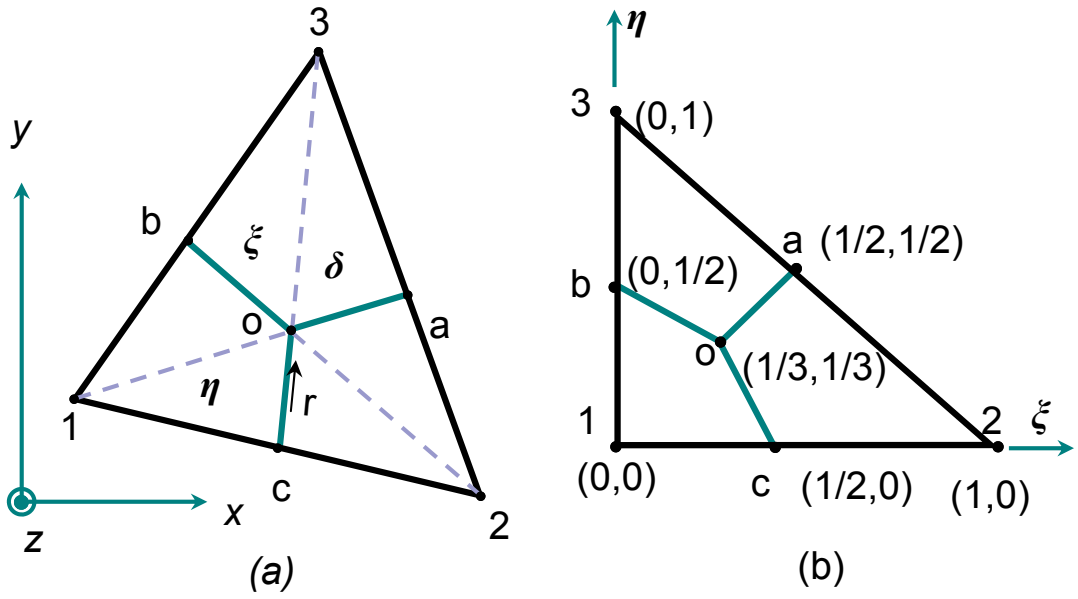


Figure A.4: (a) Element coordinate systems: global Cartesian, line and area. Element and control volume node labelling convention (b) Specific area coordinates relating to element and control volume nodes

as:

$$\sum_{i=1}^n \mathbf{T}_z^i + \mathbf{T}_z^E = 0 \quad (\text{A.24})$$

$$\sum_{i=1}^n \mathbf{M}_x^i + \mathbf{M}_x^E = 0 \quad (\text{A.25})$$

$$\sum_{i=1}^n \mathbf{M}_y^i + \mathbf{M}_y^E = 0 \quad (\text{A.26})$$

where \mathbf{T}_z^E , \mathbf{M}_x^E and \mathbf{M}_y^E are any externally applied forces or moments on the control volume and n is the number of faces of a volume. This is carried out for each element in the mesh and assembled into the global stiffness matrix in a manner analogous to the standard finite element procedure [37].

$$\begin{bmatrix} \mathbf{K}_{zw} & \mathbf{K}_{zw,y} & \mathbf{K}_{zw,x} \\ \mathbf{K}_{m_x w} & \mathbf{K}_{m_x w,y} & \mathbf{K}_{m_x w,x} \\ \mathbf{K}_{m_y w} & \mathbf{K}_{m_y w,y} & \mathbf{K}_{m_y w,x} \end{bmatrix} \begin{Bmatrix} w \\ w,y \\ -w,x \end{Bmatrix} = \begin{Bmatrix} -\mathbf{T}_z^E \\ -\mathbf{M}_x^E \\ -\mathbf{M}_y^E \end{Bmatrix} \quad (\text{A.27})$$

A.4 Boundary Conditions and Solution

The presented method is now equivalent to that of a finite element procedure with the structural equations in the form

$$[\mathbf{K}]\{\mathbf{d}\} = \{\mathbf{P}\} \quad (\text{A.28})$$

where $\{\mathbf{d}\}$ is the vector of nodal displacements, $\{\mathbf{P}\}$ is the vector of externally applied force and moments and $[\mathbf{K}]$ is the stiffness matrix (A.27). The load vector can now be modified to include applied loads and the appropriate boundary constraints applied to the stiffness matrix as in the finite element method. The stiffness matrix can then be solved by either a direct or iterative solution strategy. In the presented work, the MATLAB matrix left division routine was used.

A.5 Results

The presented method has a proper rank to its stiffness matrix and passes the patch test for states of pure bending and twist, table A.2. The convergence of maximum displacement against the analytical solution [56], with an increasing number of elements, n (figure A.5), along the plate edge, was compared against existing FE method with no quadrature and that of the commercial code ANSYS for various loading and boundary conditions. The boundary conditions used were simply supported and clamped. In both simply supported and clamped boundary cases, two conditions exist; hard and soft. For a simply supported boundary the hard condition is $w = \theta_n = 0$ and soft is $w = 0$. For a clamped boundary the hard condition is $w = \theta_n = \theta_s = 0$ and soft is $w = \theta_s = 0$, where w is the lateral displacement and θ_s and θ_n are rotations at the boundary about the tangent s

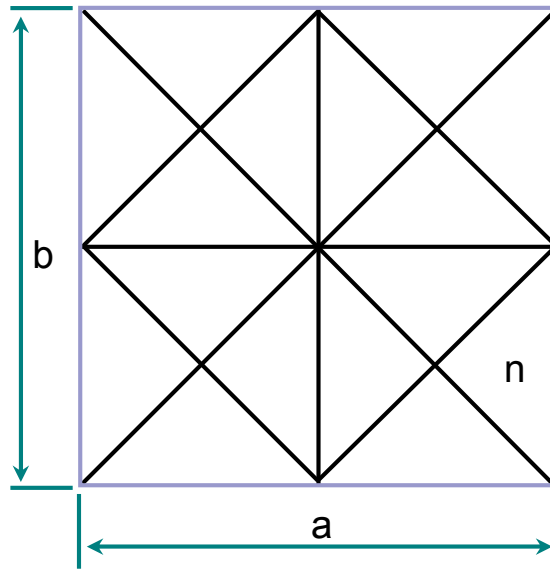


Figure A.5: *Triangular mesh of 2x2 square plate of dimensions a and b*

and the normal n respectively.

A.5.1 Patch Test

A patch of 4 elements of dimensions $a = 20\text{m}$, $b = 20\text{m}$ and $h = 0.1\text{m}$ (figure A.6) with Young's Modulus, $E = 1e3\text{N/m}^2$ and Poisson's Ratio, $\nu = 0.3$ was loaded in pure bending. The loading was:

$$\text{Node 1 - } M_x = 10\text{N/m}, M_y = -10\text{N/m}$$

$$\text{Node 2 - } M_x = 10\text{N/m}, M_y = 10\text{N/m}, w = 0$$

$$\text{Node 3 - } M_x = -10\text{N/m}, M_y = 10\text{N/m}, w = 0$$

$$\text{Node 4 - } M_x = -10\text{N/m}, M_y = -10\text{N/m}, w = 0$$

The same patch of elements were loaded for pure twist. The loading was:

$$\text{Node 1 - } M_x = 10\text{N/m}, M_y = -10\text{N/m}$$

$$\text{Node 2 - } M_x = -10\text{N/m}, M_y = -10\text{N/m}, w = 0$$

$$\text{Node 3 - } M_x = -10\text{N/m}, M_y = 10\text{N/m}, w = 0$$

$$\text{Node 4 - } M_x = 10\text{N/m}, M_y = 10\text{N/m}, w = 0$$

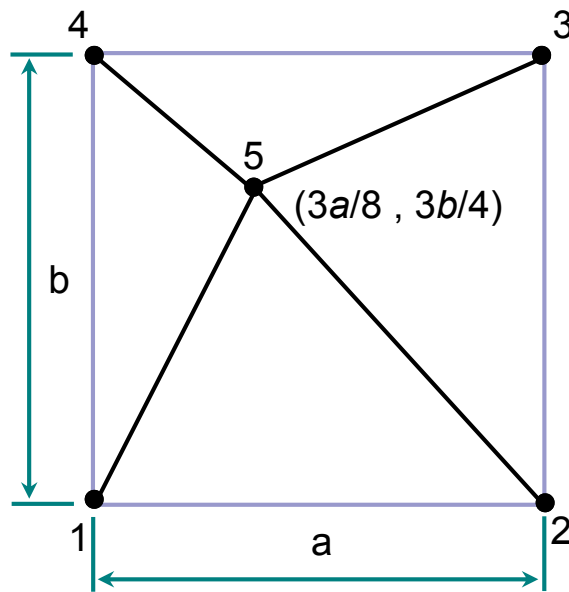


Figure A.6: Patch test mesh

For a state of pure bending and twist the CV-DKT element passed the patch test as shown in table A.2, displaying a state of pure bending and twist exactly.

A.5.2 Uniformly Distributed Load (UDL)

A square plate of dimensions $a = b = L = 1\text{m}$ and $L/h = 20$ with Young's Modulus, $E = 1e7\text{N/m}^2$ and Poisson's Ratio, $\nu = 0.3$ was loaded by a uniform pressure of 10N/m^2 . For hard (figure A.7) and soft (figure A.8) clamped and hard (figure A.9) simply supported boundary conditions the CV method converges more rapidly, as the mesh is refined, than the equivalent FEM and ANSYS elements. The method, however, appears to converge to a value slightly greater than the exact solution in the soft (figure A.10) simply supported case.

A.5.3 Centrally Applied Load

The same plate was loaded by a centrally applied point load of 1N . For hard (figure A.11) and soft (figure A.12) clamped plates the method predicts the central

Table A.2: Patch test results for a state of pure bending and twist, where w_n is the transverse displacement of node n and M_x , M_y and M_{xy} are the x bending moments, y bending moments and twisting moments respectively. Moments were calculated at the element centroids.

		w_1 (m)	w_5 (m)	M_x (N/m)	M_y (N/m)	M_{xy} (N/m)
Bending	Element 1	-	-	1.00000	0.99999	6.94e-16
	Element 2	-	-	1.00000	1.00000	8.24e-17
	Element 3	-	-	1.00000	1.00000	1.47e-16
	Element 4	-	-	0.99999	1.00000	5.18e-16
	Displacement	0.00000	0.70875	-	-	-
	Exact	0.00000	0.70875	1.00	1.00	0.00
Twist	Element 1	-	-	8.98e-17	-3.64e-15	1.00000
	Element 2	-	-	-4.57e-17	2.59e-16	1.00000
	Element 3	-	-	-5.52e-16	-4.90e-16	1.00000
	Element 4	-	-	-5.35e-16	-1.76e-16	1.00000
	Displacement	-6.23999	-0.97499	-	-	-
	Exact	-	-	0.00	0.00	1.00

displacement as accurately as the existing quadrature free FE formulation at a given level of mesh refinement. For the hard (figure A.13) simply supported case convergence is to the analytical solution but again for the soft (figure A.14) simply supported case convergence to a value above the analytical solution is observed.

A.5.4 Boundary Conditions

The boundary conditions appear to affect the convergence of the solution. For both soft and hard clamped boundaries the convergence to the analytical solution is good. When considering the simply supported case, there is a question about whether there is indeed two boundary condition types, soft (figures A.10 and A.14) and hard (figures A.9 and A.13), as in the finite element formulation. The hard case, on increasing discretisation does converge to the exact value. The soft case does not appear to converge properly to the analytical solution. On further investigation of the soft simple support boundary condition it is noted that the rotation about the normal, θ_n , does not converge to zero, on increasing discretisation (figure A.15), as shown in finite element (figure A.16). In the hard simple supported case this is prescribed and thus satisfied automatically. As the hard case is that of the classical simply supported boundary condition [37] it is suggested that only the hard case be used, as the soft boundary condition is under constrained for the CVFEM formulation.

A.6 Conclusion

A control volume based finite element method is shown here for the prediction of bending deformations in thin plates. The method is a direct equivalent to the existing discrete Kirchhoff triangular element and displays equivalent or better displacement convergence under various loads and boundary conditions. The method is quadrature free, utilising the symbolic integration tools of the Maple kernel of MATLAB.

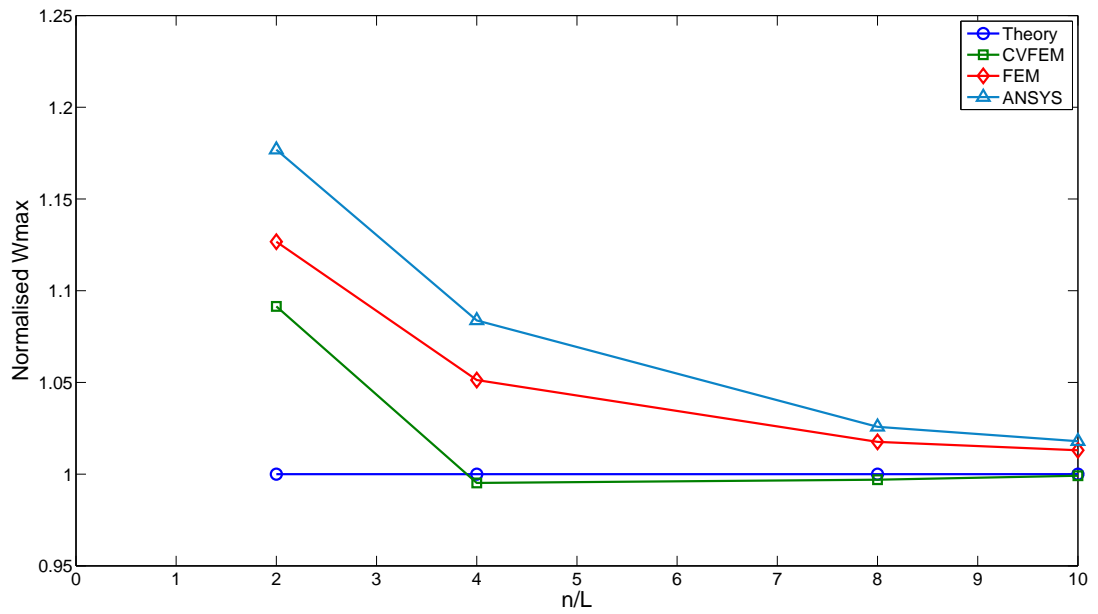


Figure A.7: Central deflection convergence to thin plate theory. Hard clamped with uniform load, $a/b = 1$ and $h = 0.05$

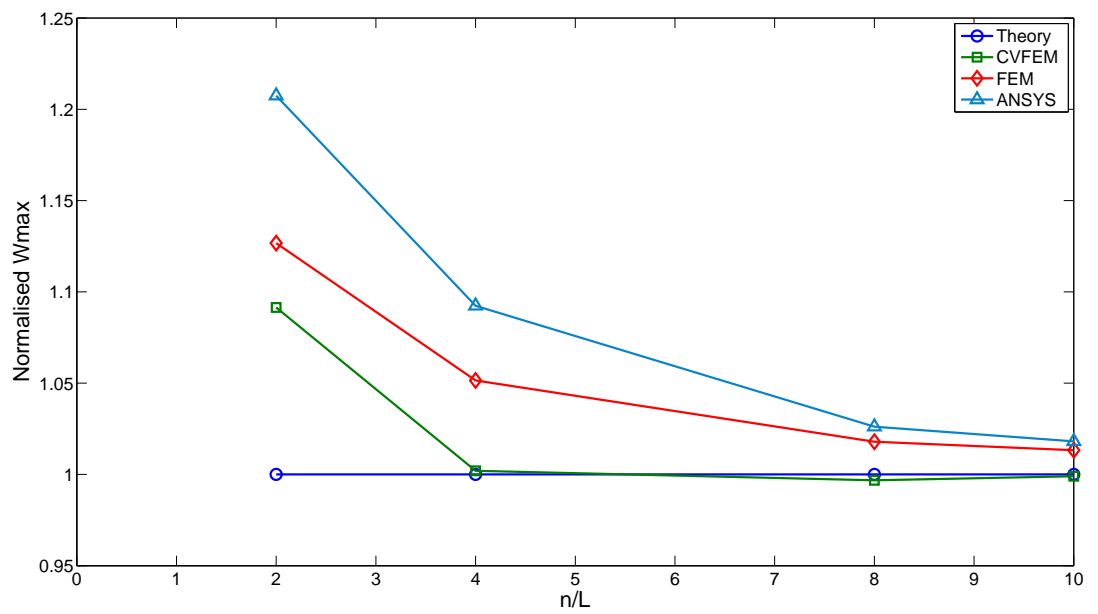


Figure A.8: Central deflection convergence to thin plate theory. Soft clamped with uniform load, $a/b = 1$ and $h = 0.05$

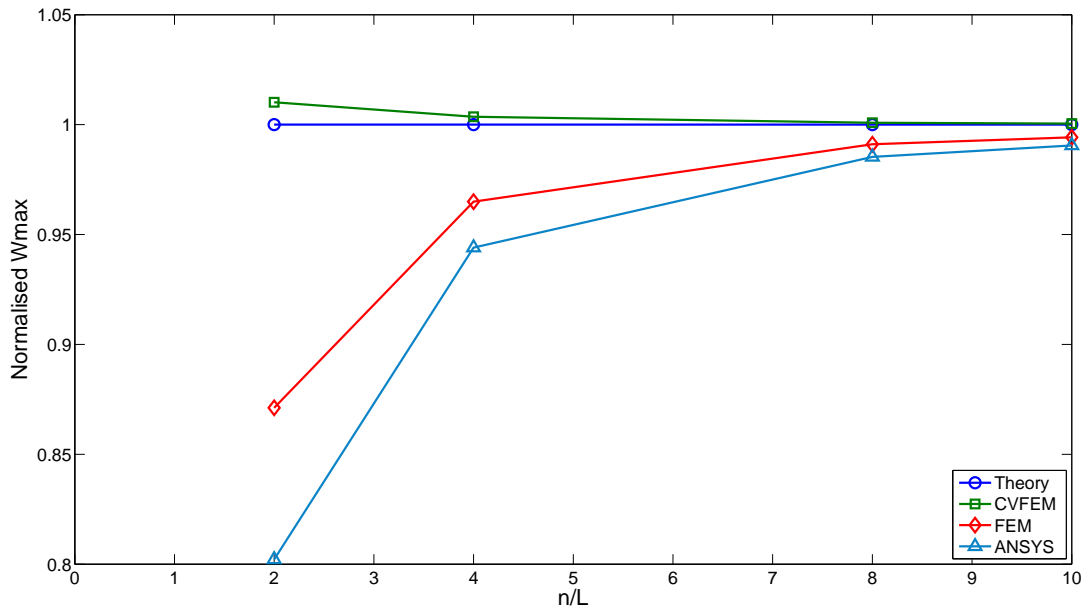


Figure A.9: Central deflection convergence to thin plate theory. Hard simply supported with uniform load, $a/b = 1$ and $h = 0.05$

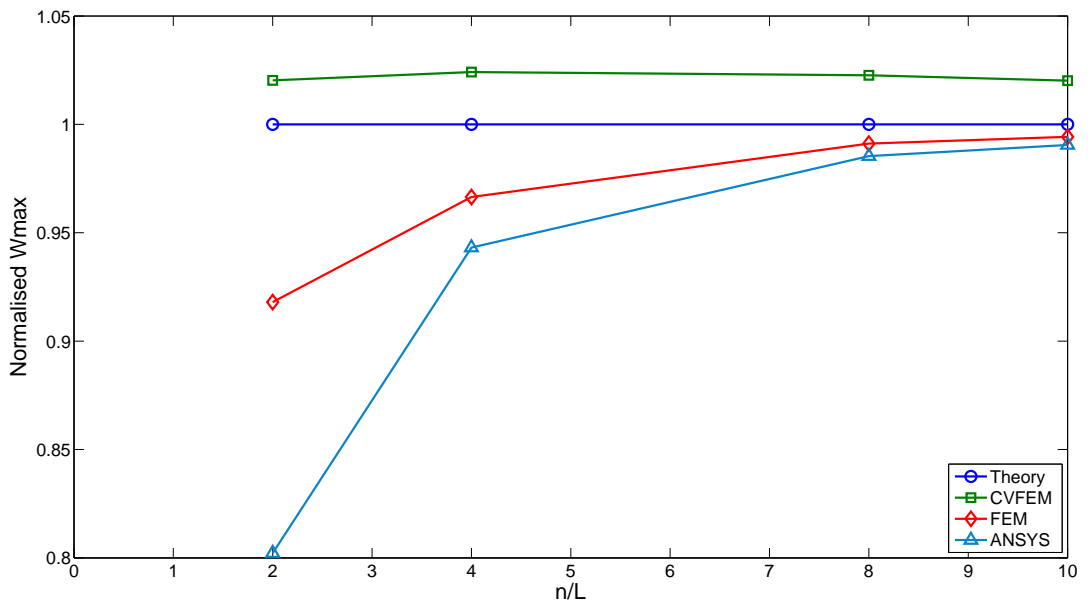


Figure A.10: Central deflection convergence to thin plate theory. Soft simply supported with uniform load, $a/b = 1$ and $h = 0.05$

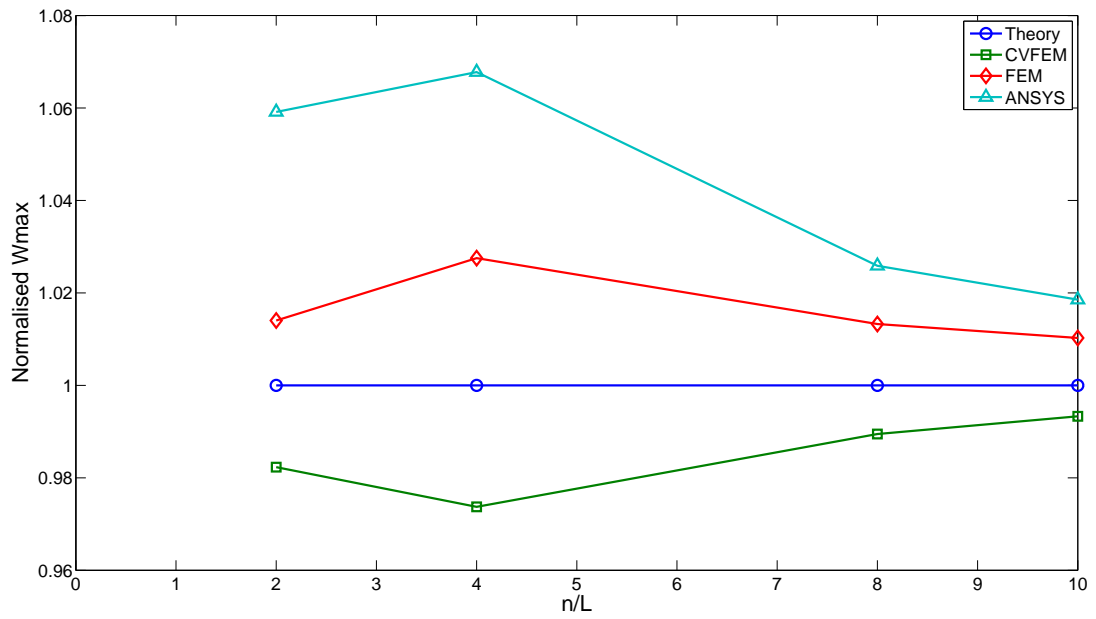


Figure A.11: Central deflection convergence to thin plate theory. Hard clamped with central point load, $a/b = 1$ and $h = 0.05$

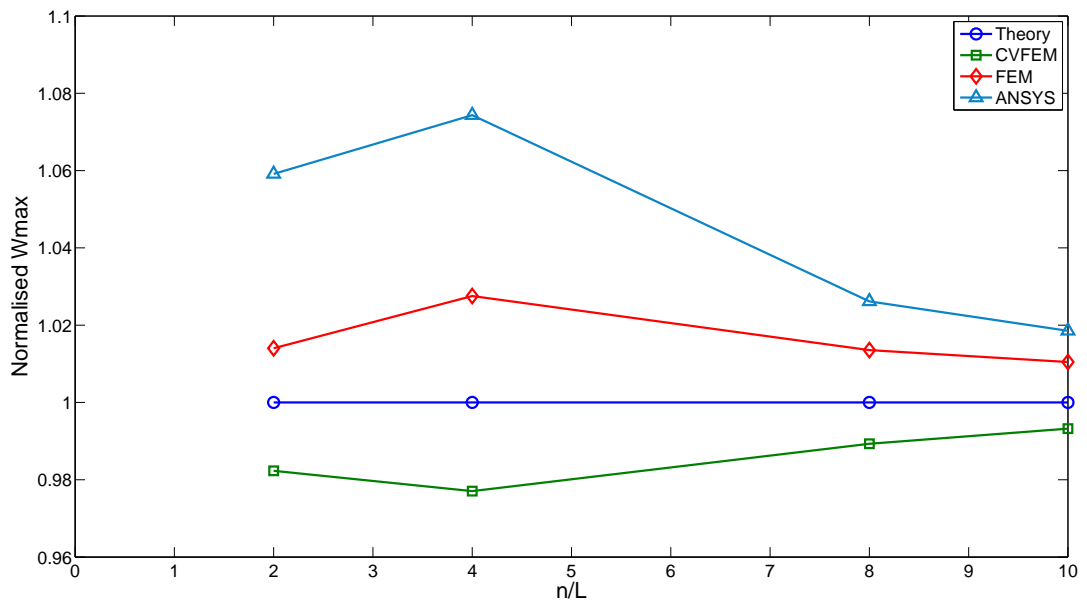


Figure A.12: Central deflection convergence to thin plate theory. Soft clamped with central point load, $a/b = 1$ and $h = 0.05$

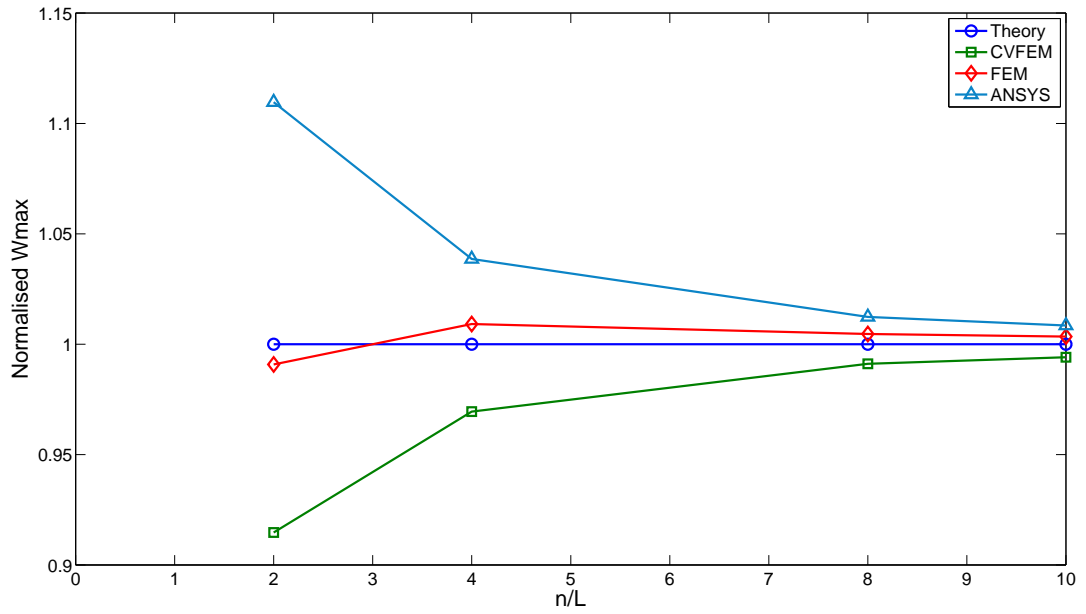


Figure A.13: Central deflection convergence to thin plate theory. Hard simply supported with central point load, $a/b = 1$ and $h = 0.05$

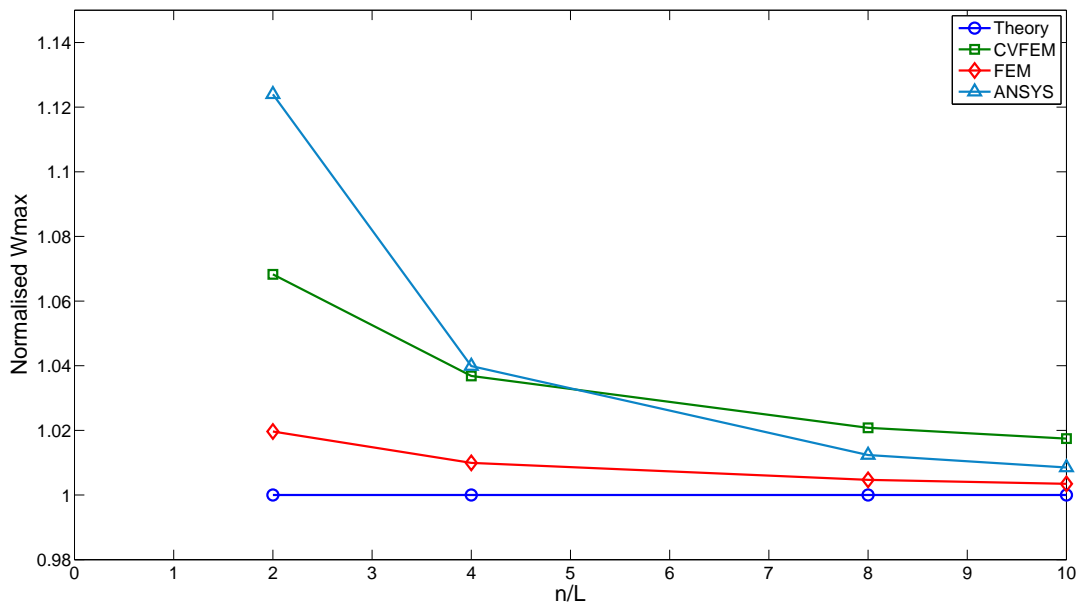


Figure A.14: Central deflection convergence to thin plate theory. Soft simply supported with central point load, $a/b = 1$ and $h = 0.05$

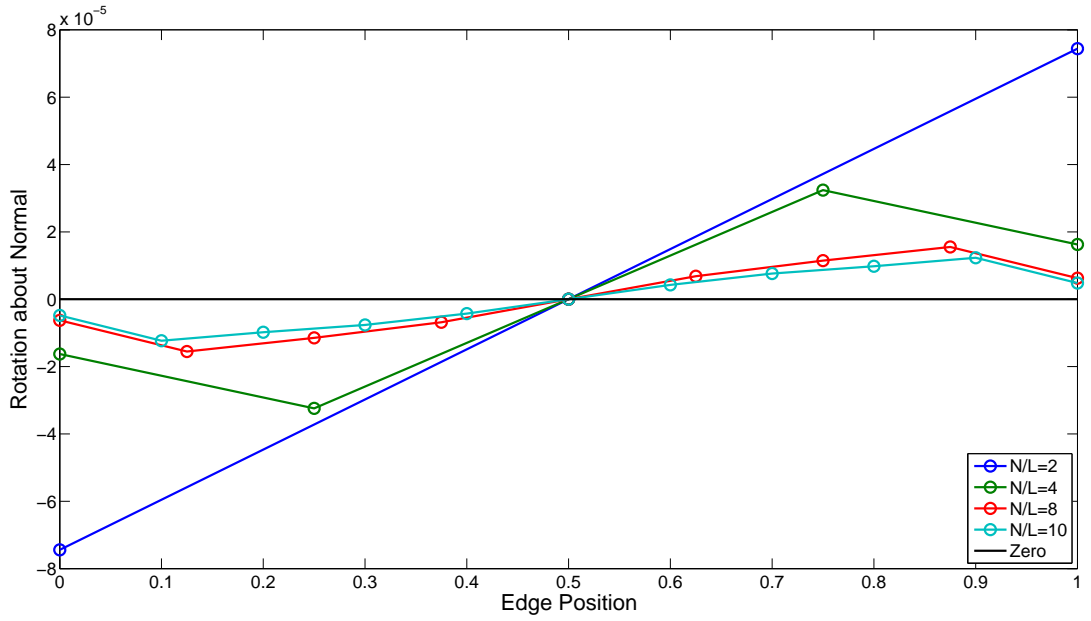


Figure A.15: Convergence of rotation about the normal along plate boundary for CVFEM. Soft simply supported with central point load, $a/b = 1$ and $h = 0.05$

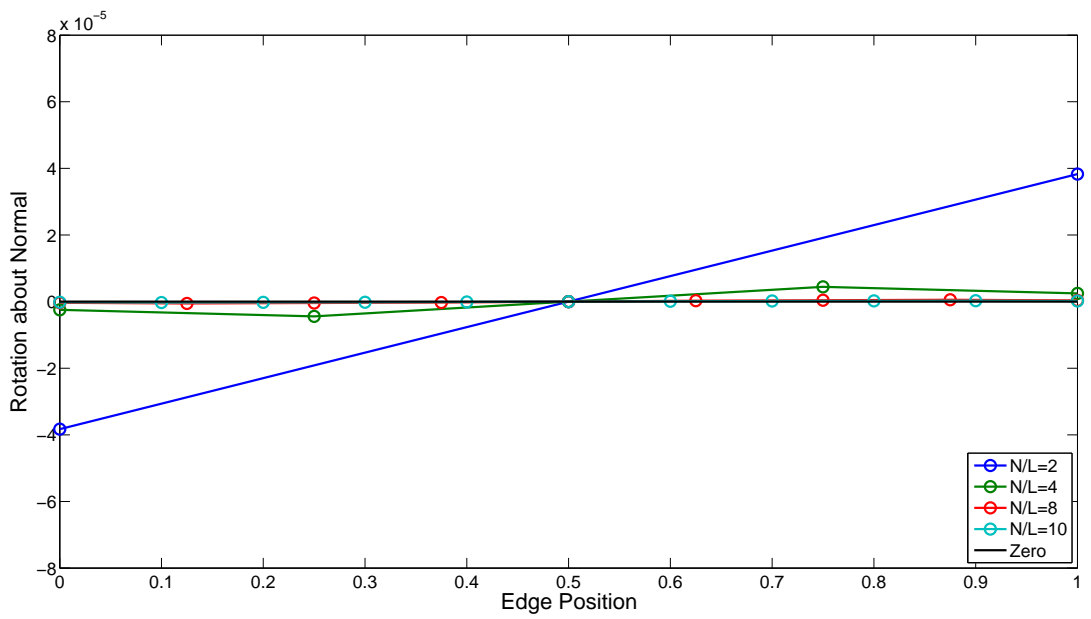


Figure A.16: Convergence of rotation about the normal along plate boundary for FEM. Soft simply supported with central point load, $a/b = 1$ and $h = 0.05$

Appendix B

MATLAB Control Volume Finite Element Codes

B.1 CV-DKT

```
1 %Author: A J Beveridge
2 %Created: 2008-09-22
3 %For: To create element stiffness matrix for
4 %control volume discete Kirchhoff triangular
5 %element
6
7 close all
8 clear all
9 clc
10
11 syms x23 x31 x12 y23 y31 y12 %predefine symbolic variable
12 syms D11 D12 D21 D22 D33
13
14 Db=[D11 D12 0           %define constitutive matrix
15     D21 D22 0           %eqn.(A.6)
16     0 0 D33];
17
18 A=x31*y12-x12*y31;      %calculate 2 x element area
```

```

19
20 syms L1 L2 L3 %define area coordinates
21
22 N=[2*(1-L2-L3)*((1/2)-L2-L3),%quadratic shape functions
23     L2*(2*L2-1), %eqn.(A.9)
24     L3*(2*L3-1),
25     4*L2*L3,
26     4*L3*(1-L2-L3),
27     4*L2*(1-L2-L3)];
28
29
30 l23=x23^2+y23^2; %calculate element edge lengths
31 l31=x31^2+y31^2;
32 l12=x12^2+y12^2;
33
34 %-----
35 %Discrete kirchhoff constraints
36 %-----
37
38 a4=-x23/l23;
39 a5=-x31/l31;
40 a6=-x12/l12;
41
42 b4=(3/4)*x23*y23/l23;
43 b5=(3/4)*x31*y31/l31;
44 b6=(3/4)*x12*y12/l12;
45
46 c4=((1/4)*x23^2-(1/2)*y23^2)/l23;
47 c5=((1/4)*x31^2-(1/2)*y31^2)/l31;
48 c6=((1/4)*x12^2-(1/2)*y12^2)/l12;
49
50 d4=-y23/l23;
51 d5=-y31/l31;
52 d6=-y12/l12;
53
54 e4=((1/4)*y23^2-(1/2)*x23^2)/l23;
55 e5=((1/4)*y31^2-(1/2)*x31^2)/l31;
56 e6=((1/4)*y12^2-(1/2)*x12^2)/l12;
57
58

```

```

59 %
60 %New shape functions eqn.(A.15)
61 %
62 Hx=[1.5*(a6*N(6)-a5*N(5)),
63      b5*N(5)+b6*N(6),
64      N(1)-c5*N(5)-c6*N(6),
65      1.5*(a4*N(4)-a6*N(6)),
66      b6*N(6)+b4*N(4),
67      N(2)-c6*N(6)-c4*N(4),
68      1.5*(a5*N(5)-a4*N(4)),
69      b4*N(4)+b5*N(5),
70      N(3)-c4*N(4)-c5*N(5)];
71
72 Hy=[1.5*(d6*N(6)-d5*N(5)),
73      -N(1)+e5*N(5)+e6*N(6),
74      -b5*N(5)-b6*N(6),
75      1.5*(d4*N(4)-d6*N(6)),
76      -N(2)+e6*N(6)+e4*N(4),
77      -b6*N(6)-b4*N(4),
78      1.5*(d5*N(5)-d4*N(4)),
79      -N(3)+e4*N(4)+e5*N(5),
80      -b4*N(4)-b5*N(5)];
81
82 Hx=simple(Hx);           %This step optimises the
83 Hy=simple(Hy);           %symbolic output
84 %
85 %Differentiate new shape functions with respect to the
86 %area coordinates
87 %
88 dHxL2=diff(Hx,L2);
89 dHxL3=diff(Hx,L3);
90 dHyL2=diff(Hy,L2);
91 dHyL3=diff(Hy,L3);
92
93 dHxL2=simple(dHxL2);
94 dHxL3=simple(dHxL3);
95 dHyL2=simple(dHyL2);
96 dHyL3=simple(dHyL3);
97
98 %

```

```

99 %Calculate moment curvature matrix eqn.(A.17)
100 %-----
101 B=(1/A)*[(y31*dHxL2. ')+(y12*dHxL3. '),
102      (-x31*dHyL2. ')+(-x12*dHyL3. '),
103      (-x31*dHxL2. ')+(-x12*dHxL3. ')+(y31*dHyL2. ')+(y12*dHyL3. ')] ;
104
105 Bb=simple(B);
106 Mb=Db*Bb; %Calculate bending stresses
107
108 Mx=Mb(1, :);
109 My=Mb(2, :);
110 Mxy=Mb(3, :);
111 %-----
112 %Calculate shear stresses eqn.(A.18)
113 %-----
114 dtxL2=diff(Mx,L2);
115 dtxL3=diff(Mx,L3);
116 dtyL2=diff(My,L2);
117 dtyL3=diff(My,L3);
118 dtxyL2=diff(Mxy,L2);
119 dtxyL3=diff(Mxy,L3);
120
121 T=(1/A)*[(y31*dtxL2)+(y12*dtxL3)+(-x31*dtxyL2)+(-x12*dtxyL3),
122      (y31*dtxyL2)+(y12*dtxyL3)+(-x31*dtyL2)+(-x12*dtyL3)] ;
123
124 Bqd=T;
125 Bdd=Db*Bb;
126 %-----
127 %Control volume geometry
128 %-----
129 syms x1 x2 x3 y1 y2 y3 %nodal coordinates
130 x=[x1;x2;x3];
131 y=[y1;y2;y3];
132 syms Loa Lob Loc %CV face lengths
133 syms COSoa SINoa COSob SINob COSoc SINoc
134 %-----
135 %Moment arm functions
136 %-----
137 X=(x1*(1-L2-L3))+(x2*L2)+(x3*L3);
138 Y=(y1*(1-L2-L3))+(y2*L2)+(y3*L3);

```

```

139 %-----
140 %Shear integrals, eqn.(A.21) substitutions in table A.1
141 %-----
142 Bqq=subs(Bqd,L2,(1/2)*(1-L3),0); %substitute area coordinates
143 %integrate stress resultants
144 Qoc=(3*Loc*COSoc*int(Bqq(1,:),L3,0,1/3))
145     +(3*Loc*SINoc*int(Bqq(2,:),L3,0,1/3));
146 clear Bqq
147 Bqq=subs(Bqd,L3,(1/2)*(1-L2),0);
148 Qob=(3*Lob*COSob*int(Bqq(1,:),L2,0,1/3))
149     +(3*Lob*SINob*int(Bqq(2,:),L2,0,1/3));
150 clear Bqq
151 Bq1=subs(Bqd,L3,L2,0);
152 Bqq=subs(Bq1,L2,(1/2)*(1-L1),0);
153 Qoa=(3*Loa*COSoa*int(Bqq(1,:),L1,0,1/3))
154     +(3*Loa*SINoa*int(Bqq(2,:),L1,0,1/3));
155 %-----
156 %Moment integrals eqns.(A.22) and (A.23)
157 %-----
158 B=subs(Bdd,L2,(1/2)*(1-L3),0);
159 Mocx=(3*Loc*COSoc*int(B(1,:),L3,0,1/3))
160     +(3*Loc*SINoc*int(B(3,:),L3,0,1/3));
161 Mocy=(3*Loc*SINoc*int(B(2,:),L3,0,1/3))
162     +(3*Loc*COSoc*int(B(3,:),L3,0,1/3));
163 clear B
164 B=subs(Bdd,L3,(1/2)*(1-L2),0);
165 Mobx=(3*Lob*COSob*int(B(1,:),L2,0,1/3))
166     +(3*Lob*SINob*int(B(3,:),L2,0,1/3));
167 Moby=(3*Lob*SINob*int(B(2,:),L2,0,1/3))
168     +(3*Lob*COSob*int(B(3,:),L2,0,1/3));
169 clear B
170 B1=subs(Bdd,L3,L2,0);
171 B=subs(B1,L2,(1/2)*(1-L1),0);
172 Moax=(3*Loa*COSoa*int(B(1,:),L1,0,1/3))
173     +(3*Loa*SINoa*int(B(3,:),L1,0,1/3));
174 Moay=(3*Loa*SINoa*int(B(2,:),L1,0,1/3))
175     +(3*Loa*COSoa*int(B(3,:),L1,0,1/3));
176 %-----
177 %Shear moment integrals eqns.(A.22) and (A.23)
178 %-----

```

```

179 clear Bqq
180 Xs=subs(X,L2,(1/2)*(1-L3),0);
181 Ys=subs(Y,L2,(1/2)*(1-L3),0);
182 Bqq=subs(Bqd,L2,(1/2)*(1-L3),0);
183 MQocxi=(3*Loc*COSoc*int((Xs-x1)*Bqq(1,:),L3,0,1/3))
184         +(3*Loc*SINoc*int((Xs-x1)*Bqq(2,:),L3,0,1/3));
185 MQocyi=(3*Loc*COSoc*int((Ys-y1)*Bqq(1,:),L3,0,1/3))
186         +(3*Loc*SINoc*int((Ys-y1)*Bqq(2,:),L3,0,1/3));
187 MQocxj=(3*Loc*COSoc*int((Xs-x2)*Bqq(1,:),L3,0,1/3))
188         +(3*Loc*SINoc*int((Xs-x2)*Bqq(2,:),L3,0,1/3));
189 MQocyj=(3*Loc*COSoc*int((Ys-y2)*Bqq(1,:),L3,0,1/3))
190         +(3*Loc*SINoc*int((Ys-y2)*Bqq(2,:),L3,0,1/3));
191 clear Xs
192 clear Ys
193 clear Bqq
194 Xs=subs(X,L3,(1/2)*(1-L2),0);
195 Ys=subs(Y,L3,(1/2)*(1-L2),0);
196 Bqq=subs(Bqd,L3,(1/2)*(1-L2),0);
197 MQobxi=(3*Lob*COSob*int((Xs-x1)*Bqq(1,:),L2,0,1/3))
198         +(3*Lob*SINob*int((Xs-x1)*Bqq(2,:),L2,0,1/3));
199 MQobyi=(3*Lob*COSob*int((Ys-y1)*Bqq(1,:),L2,0,1/3))
200         +(3*Lob*SINob*int((Ys-y1)*Bqq(2,:),L2,0,1/3));
201 MQobxk=(3*Lob*COSob*int((Xs-x3)*Bqq(1,:),L2,0,1/3))
202         +(3*Lob*SINob*int((Xs-x3)*Bqq(2,:),L2,0,1/3));
203 MQobyk=(3*Lob*COSob*int((Ys-y3)*Bqq(1,:),L2,0,1/3))
204         +(3*Lob*SINob*int((Ys-y3)*Bqq(2,:),L2,0,1/3));
205 clear Xs
206 clear Ys
207 clear Bqq
208 Xs1=subs(X,L3,L2,0);
209 Xs=subs(Xs1,L2,(1/2)*(1-L1),0);
210 Ys1=subs(Y,L3,L2,0);
211 Ys=subs(Ys1,L2,(1/2)*(1-L1),0);
212 Bq1=subs(Bqd,L3,L2,0);
213 Bqq=subs(Bq1,L2,(1/2)*(1-L1),0);
214 MQoaxj=(3*Loa*COSoa*int((Xs-x2)*Bqq(1,:),L1,0,1/3))
215         +(3*Loa*SINoa*int((Xs-x2)*Bqq(2,:),L1,0,1/3));
216 MQoayj=(3*Loa*COSoa*int((Ys-y2)*Bqq(1,:),L1,0,1/3))
217         +(3*Loa*SINoa*int((Ys-y2)*Bqq(2,:),L1,0,1/3));
218 MQoaxk=(3*Loa*COSoa*int((Xs-x3)*Bqq(1,:),L1,0,1/3))

```

```

219         +(3*Loa*SINoa*int((Xs-x3)*Bqq(2,:),L1,0,1/3));
220 MQoayk=(3*Loa*COSoa*int((Ys-y3)*Bqq(1,:),L1,0,1/3))
221         +(3*Loa*SINoa*int((Ys-y3)*Bqq(2,:),L1,0,1/3));
222 %-----
223 %Assemble global stiffness matrix from CV equilibrium eqn.(A.27)
224 %-----
225 %NODE i;
226 %-----
227 %Equilibrium in Z direction
228 k(1,:)=- (Qoc-Qob);
229 %Equilibrium in moments in X direction
230 k(3,:)=- ((Mocx-MQocxi)-(Mobx-MQobxi));
231 %Equilibrium in moments in Y direction
232 k(2,:)=( (Mocy-MQocyi)-(Moby-MQobyi));
233 %-----
234 %NODE j;
235 %-----
236 %Equilibrium in Z direction
237 k(4,:)=- (Qoa-Qoc);
238 %Equilibrium in moments in X direction
239 k(6,:)=- ((Moax-MQoaxj)-(Mocx-MQocxj));
240 %Equilibrium in moments in Y direction
241 k(5,:)=( (Moay-MQoayj)-(Mocy-MQocyj));
242 %-----
243 %NODE k;
244 %-----
245 %Equilibrium in Z direction
246 k(7,:)=- (Qob-Qoa);
247 %Equilibrium in moments in X direction
248 k(9,:)=- ((Mobx-MQobxk)-(Moax-MQoaxk));
249 %Equilibrium in moments in Y direction
250 k(8,:)=( (Moby-MQobyk)-(Moay-MQoayk));

```

B.2 CV-MPLST

```

1 %Author: A J Beveridge
2 %Created: 2010-04-23

```

```

3 %For: To create element stiffness matrix for
4 %linear strain micropolar control volume
5 %finite element CV-MPLST
6
7 close all
8 clear all
9 clc
10
11 syms x23 x31 x12 y23 y31 y12
12 syms D11 D12 D21 D22 D33 D34 D43 D44 D55 D66
13
14 D=[D11 D12 0 0 0 0           %define constitutive matrix
15     D21 D22 0 0 0 0           %eqn.(4.8)
16     0 0 D33 D34 0 0
17     0 0 D43 D44 0 0
18     0 0 0 0 D55 0
19     0 0 0 0 0 D66];
20
21 A=x31*y12-x12*y31;           %%calculate 2 x element area
22
23 syms L1 L2 L3
24
25 N=[L1*(2*L1-1)               %quadratic shape functions
26     L2*(2*L2-1)               %eqn.(4.3)
27     L3*(2*L3-1)
28     4*L1*L2
29     4*L2*L3
30     4*L3*L1];
31 %-----
32 %Differentiate shape functions
33 %-----
34 dNxL1=diff(N,L1);
35 dNxL2=diff(N,L2);
36 dNxL3=diff(N,L3);
37 dNyL1=diff(N,L1);
38 dNyL2=diff(N,L2);
39 dNyL3=diff(N,L3);
40
41 dNxL1=simple(dNxL1);
42 dNxL2=simple(dNxL2);

```

```

43 dNxL3=simple(dNxL3);
44 dNyL1=simple(dNyL1);
45 dNyL2=simple(dNyL2);
46 dNyL3=simple(dNyL3);
47
48 dNx=(1/A)*(y23*dNxL1+y31*dNxL2+y12*dNxL3);
49 dNy=(1/A)*(-x23*dNyL1-x31*dNyL2-x12*dNyL3);
50 %-----
51 %Define strain displacement matrix B and assemble
52 %from shape functions eqn.(4.13)
53 %-----
54 B=sym(zeros(6,18));
55
56 for n=1:6
57     B(1,(3*n-2))=dNx(n);
58     B(2,(3*n-1))=dNy(n);
59     B(3,(3*n-2))=dNy(n);
60     B(3,(3*n))=N(n);
61     B(4,(3*n-1))=dNx(n);
62     B(4,(3*n))=-N(n);
63     B(5,(3*n))=dNx(n);
64     B(6,(3*n))=dNy(n);
65 end
66
67 %calculate stress resultants eqn.(4.14)
68 Sr=D*B;
69 %-----
70 %Define control volume geometry
71 %-----
72 syms x1 x2 x3 x4 x5 x6 y1 y2 y3 y4 y5 y6 %nodal coordinates
73 x=[x1;x2;x3;x4;x5;x6];
74 y=[y1;y2;y3;y4;y5;y6];
75 syms Lga Lhb Lhc Lid Lie Lgf Ljg Ljh Lji %CV face lengths
76 syms COSga SINGa COShb SINhb COShc SINhc COSid SINid COSie SINie
77 syms COSgf SINGf COSjg SINjg COSjh SINjh COSji SINji
78 %-----
79 %Moment Arm Functions eqn.(4.24)
80 %-----
81 X=(x(1)*L1)+(x(2)*L2)+(x(3)*L3);
82 Y=(y(1)*L1)+(y(2)*L2)+(y(3)*L3);

```

```

83 %
84 %Calculate discrete integrals
85 %
86 %Integrating in L3
87 %Line g-a eqns.(4.26, 4.27, 4.28)
88 Srs=subs(Sr,L2,(1/3)*L1,0);
89 Srss=subs(Srs,L1,(3/4)*(1-L3),0);
90 Xs=subs(X,L2,(1/3)*L1,0);
91 Xss=subs(Xs,L1,(3/4)*(1-L3),0);
92 Ys=subs(Y,L2,(1/3)*L1,0);
93 Yss=subs(Ys,L1,(3/4)*(1-L3),0);
94 Fsxga=(5*Lga*COSga*int(Srss(1,:),L3,0,1/5));
95 Fsyga=(5*Lga*SINga*int(Srss(2,:),L3,0,1/5));
96 Ftyxga=(5*Lga*SINga*int(Srss(3,:),L3,0,1/5));
97 Ftxyga=(5*Lga*COSga*int(Srss(4,:),L3,0,1/5));
98 Mxga=(5*Lga*COSga*int(Srss(5,:),L3,0,1/5));
99 Myga=(5*Lga*SINga*int(Srss(6,:),L3,0,1/5));
100 Msxga1=(5*Lga*SINga*int((Yss-y(1))*Srss(3,:),L3,0,1/5));
101 Msyga1=(5*Lga*COSga*int((Xss-x(1))*Srss(4,:),L3,0,1/5));
102 Msxga4=(5*Lga*SINga*int((Yss-y(4))*Srss(3,:),L3,0,1/5));
103 Msyga4=(5*Lga*COSga*int((Xss-x(4))*Srss(4,:),L3,0,1/5));
104 clear Srs Srss Xs Xss Ys Yss
105 %Line h-b (continues for all other CV faces see table 4.2
106 %for substitutions)
107 Srs=subs(Sr,L1,(1/3)*L2,0);
108 Srss=subs(Srs,L2,(3/4)*(1-L3),0);
109 Xs=subs(X,L1,(1/3)*L2,0);
110 Xss=subs(Xs,L2,(3/4)*(1-L3),0);
111 Ys=subs(Y,L1,(1/3)*L2,0);
112 Yss=subs(Ys,L2,(3/4)*(1-L3),0);
113 Fsxhb=(5*Lhb*COSHb*int(Srss(1,:),L3,0,1/5));
114 Fsyhb=(5*Lhb*SINHb*int(Srss(2,:),L3,0,1/5));
115 Ftyxhb=(5*Lhb*SINHb*int(Srss(3,:),L3,0,1/5));
116 Ftxyhb=(5*Lhb*COSHb*int(Srss(4,:),L3,0,1/5));
117 Mxhb=(5*Lhb*COSHb*int(Srss(5,:),L3,0,1/5));
118 Myhb=(5*Lhb*SINHb*int(Srss(6,:),L3,0,1/5));
119 Msxhb2=(5*Lhb*SINHb*int((Yss-y(2))*Srss(3,:),L3,0,1/5));
120 Msyhb2=(5*Lhb*COSHb*int((Xss-x(2))*Srss(4,:),L3,0,1/5));
121 Msxhb4=(5*Lhb*SINHb*int((Yss-y(4))*Srss(3,:),L3,0,1/5));
122 Msyhb4=(5*Lhb*COSHb*int((Xss-x(4))*Srss(4,:),L3,0,1/5));

```

```

123 clear Srs Srss Xs Xss Ys Yss
124 %Line j-i
125 Srs=subs(Sr,L1,L2,0);
126 Srss=subs(Srs,L2,((1/2)*(1-L3)),0);
127 Xs=subs(X,L1,L2,0);
128 Xss=subs(Xs,L2,((1/2)*(1-L3)),0);
129 Ys=subs(Y,L1,L2,0);
130 Yss=subs(Ys,L2,((1/2)*(1-L3)),0);
131 Fsxji=((15/4)*Lji*COSji*int(Srss(1,:),L3,1/3,3/5));
132 Fsyji=((15/4)*Lji*SINji*int(Srss(2,:),L3,1/3,3/5));
133 Ftyxji=((15/4)*Lji*SINji*int(Srss(3,:),L3,1/3,3/5));
134 Ftxyji=((15/4)*Lji*COSji*int(Srss(4,:),L3,1/3,3/5));
135 Mxji=((15/4)*Lji*COSji*int(Srss(5,:),L3,1/3,3/5));
136 Myji=((15/4)*Lji*SINji*int(Srss(6,:),L3,1/3,3/5));
137 Msxji5=((15/4)*Lji*SINji*int((Yss-y(5))*Srss(3,:),L3,1/3,3/5));
138 Msyji5=((15/4)*Lji*COSji*int((Xss-x(5))*Srss(4,:),L3,1/3,3/5));
139 Msxji6=((15/4)*Lji*SINji*int((Yss-y(6))*Srss(3,:),L3,1/3,3/5));
140 Msyji6=((15/4)*Lji*COSji*int((Xss-x(6))*Srss(4,:),L3,1/3,3/5));
141 clear Srs Srss Xs Xss Ys Yss
142 %—————
143 %Integrating in L1
144 %Line h-c
145 Srs=subs(Sr,L3,(1/3)*L2,0);
146 Srss=subs(Srs,L2,(3/4)*(1-L1),0);
147 Xs=subs(X,L3,(1/3)*L2,0);
148 Xss=subs(Xs,L2,(3/4)*(1-L1),0);
149 Ys=subs(Y,L3,(1/3)*L2,0);
150 Yss=subs(Ys,L2,(3/4)*(1-L1),0);
151 Fsxhc=(5*Lhc*COSHc*int(Srss(1,:),L1,0,1/5));
152 Fsyhc=(5*Lhc*SINHc*int(Srss(2,:),L1,0,1/5));
153 Ftyxhc=(5*Lhc*SINHc*int(Srss(3,:),L1,0,1/5));
154 Ftxyhc=(5*Lhc*COSHc*int(Srss(4,:),L1,0,1/5));
155 Mxhc=(5*Lhc*COSHc*int(Srss(5,:),L1,0,1/5));
156 Myhc=(5*Lhc*SINHc*int(Srss(6,:),L1,0,1/5));
157 Msxhc2=(5*Lhc*SINHc*int((Yss-y(2))*Srss(3,:),L1,0,1/5));
158 Msyhc2=(5*Lhc*COSHc*int((Xss-x(2))*Srss(4,:),L1,0,1/5));
159 Msxhc5=(5*Lhc*SINHc*int((Yss-y(5))*Srss(3,:),L1,0,1/5));
160 Msyhc5=(5*Lhc*COSHc*int((Xss-x(5))*Srss(4,:),L1,0,1/5));
161 clear Srs Srss Xs Xss Ys Yss
162 %Line i-d

```

```

163 Srs=subs(Sr,L2,(1/3)*L3,0);
164 Srss=subs(Srs,L3,(3/4)*(1-L1),0);
165 Xs=subs(X,L2,(1/3)*L3,0);
166 Xss=subs(Xs,L3,(3/4)*(1-L1),0);
167 Ys=subs(Y,L2,(1/3)*L3,0);
168 Yss=subs(Ys,L3,(3/4)*(1-L1),0);
169 Fsxid=(5*Lid*COSid*int(Srss(1,:),L1,0,1/5));
170 Fsyid=(5*Lid*SINid*int(Srss(2,:),L1,0,1/5));
171 Ftyxid=(5*Lid*SINid*int(Srss(3,:),L1,0,1/5));
172 Ftxyid=(5*Lid*COSid*int(Srss(4,:),L1,0,1/5));
173 Mxid=(5*Lid*COSid*int(Srss(5,:),L1,0,1/5));
174 Myid=(5*Lid*SINid*int(Srss(6,:),L1,0,1/5));
175 Msxid3=(5*Lid*SINid*int((Yss-y(3))*Srss(3,:),L1,0,1/5));
176 Msyid3=(5*Lid*COSid*int((Xss-x(3))*Srss(4,:),L1,0,1/5));
177 Msxid5=(5*Lid*SINid*int((Yss-y(5))*Srss(3,:),L1,0,1/5));
178 Msyid5=(5*Lid*COSid*int((Xss-x(5))*Srss(4,:),L1,0,1/5));
179 clear Srs Srss Xs Xss Ys Yss
180 %Line j-g
181 Srs=subs(Sr,L2,L3,0);
182 Srss=subs(Srs,L3,((1/2)*(1-L1)),0);
183 Xs=subs(X,L2,L3,0);
184 Xss=subs(Xs,L3,((1/2)*(1-L1)),0);
185 Ys=subs(Y,L2,L3,0);
186 Yss=subs(Ys,L3,((1/2)*(1-L1)),0);
187 Fsxjg=((15/4)*Ljg*COSjg*int(Srss(1,:),L1,1/3,3/5));
188 Fsyjg=((15/4)*Ljg*SINjg*int(Srss(2,:),L1,1/3,3/5));
189 Ftyxjg=((15/4)*Ljg*SINjg*int(Srss(3,:),L1,1/3,3/5));
190 Ftxyjg=((15/4)*Ljg*COSjg*int(Srss(4,:),L1,1/3,3/5));
191 Mxjg=((15/4)*Ljg*COSjg*int(Srss(5,:),L1,1/3,3/5));
192 Myjg=((15/4)*Ljg*SINjg*int(Srss(6,:),L1,1/3,3/5));
193 Msxjg4=((15/4)*Ljg*SINjg*int((Yss-y(4))*Srss(3,:),L1,1/3,3/5));
194 Msyjg4=((15/4)*Ljg*COSjg*int((Xss-x(4))*Srss(4,:),L1,1/3,3/5));
195 Msxjg6=((15/4)*Ljg*SINjg*int((Yss-y(6))*Srss(3,:),L1,1/3,3/5));
196 Msyjg6=((15/4)*Ljg*COSjg*int((Xss-x(6))*Srss(4,:),L1,1/3,3/5));
197 clear Srs Srss Xs Xss Ys Yss
198 %
199 %Integrating in L2
200 %Line i-e
201 Srs=subs(Sr,L1,(1/3)*L3,0);
202 Srss=subs(Srs,L3,(3/4)*(1-L2),0);

```

```

203 Xs=subs(X,L1,(1/3)*L3,0);
204 Xss=subs(Xs,L3,(3/4)*(1-L2),0);
205 Ys=subs(Y,L1,(1/3)*L3,0);
206 Yss=subs(Ys,L3,(3/4)*(1-L2),0);
207 Fsxie=(5*Lie*COSie*int(Srssl(1,:),L2,0,1/5));
208 Fsyie=(5*Lie*SINie*int(Srssl(2,:),L2,0,1/5));
209 Ftyxie=(5*Lie*SINie*int(Srssl(3,:),L2,0,1/5));
210 Ftxyie=(5*Lie*COSie*int(Srssl(4,:),L2,0,1/5));
211 Mxie=(5*Lie*COSie*int(Srssl(5,:),L2,0,1/5));
212 Myie=(5*Lie*SINie*int(Srssl(6,:),L2,0,1/5));
213 Msxie3=(5*Lie*SINie*int((Yss-y(3))*Srssl(3,:),L2,0,1/5));
214 Msyie3=(5*Lie*COSie*int((Xss-x(3))*Srssl(4,:),L2,0,1/5));
215 Msxie6=(5*Lie*SINie*int((Yss-y(6))*Srssl(3,:),L2,0,1/5));
216 Msyie6=(5*Lie*COSie*int((Xss-x(6))*Srssl(4,:),L2,0,1/5));
217 clear Srs Srssl Xs Xss Ys Yss
218 %Line g-f
219 Srs=subs(Sr,L3,(1/3)*L1,0);
220 Srssl=subs(Srs,L1,(3/4)*(1-L2),0);
221 Xs=subs(X,L3,(1/3)*L1,0);
222 Xss=subs(Xs,L1,(3/4)*(1-L2),0);
223 Ys=subs(Y,L3,(1/3)*L1,0);
224 Yss=subs(Ys,L1,(3/4)*(1-L2),0);
225 Fsxgfl=(5*Lgf*COSgfl*int(Srssl(1,:),L2,0,1/5));
226 Fsygfl=(5*Lgf*SINGfl*int(Srssl(2,:),L2,0,1/5));
227 Ftyxgfl=(5*Lgf*SINGfl*int(Srssl(3,:),L2,0,1/5));
228 Ftxygfl=(5*Lgf*COSgfl*int(Srssl(4,:),L2,0,1/5));
229 Mxgfl=(5*Lgf*COSgfl*int(Srssl(5,:),L2,0,1/5));
230 Mygfl=(5*Lgf*SINGfl*int(Srssl(6,:),L2,0,1/5));
231 Msxgfl1=(5*Lgf*SINGfl*int((Yss-y(1))*Srssl(3,:),L2,0,1/5));
232 Msygfl1=(5*Lgf*COSgfl*int((Xss-x(1))*Srssl(4,:),L2,0,1/5));
233 Msxgfl6=(5*Lgf*SINGfl*int((Yss-y(6))*Srssl(3,:),L2,0,1/5));
234 Msygfl6=(5*Lgf*COSgfl*int((Xss-x(6))*Srssl(4,:),L2,0,1/5));
235 clear Srs Srssl Xs Xss Ys Yss
236 %Line j-h
237 Srs=subs(Sr,L1,L3,0);
238 Srssl=subs(Srs,L3,((1/2)*(1-L2)),0);
239 Xs=subs(X,L1,L3,0);
240 Xss=subs(Xs,L3,((1/2)*(1-L2)),0);
241 Ys=subs(Y,L1,L3,0);
242 Yss=subs(Ys,L3,((1/2)*(1-L2)),0);

```

```

243 Fsxjh=((15/4)*Ljh*COSjh*int(Srss(1,:),L2,1/3,3/5));
244 Fsyjh=((15/4)*Ljh*SINjh*int(Srss(2,:),L2,1/3,3/5));
245 Ftyxjh=((15/4)*Ljh*SINjh*int(Srss(3,:),L2,1/3,3/5));
246 Ftxyjh=((15/4)*Ljh*COSjh*int(Srss(4,:),L2,1/3,3/5));
247 Mxjh=((15/4)*Ljh*COSjh*int(Srss(5,:),L2,1/3,3/5));
248 Myjh=((15/4)*Ljh*SINjh*int(Srss(6,:),L2,1/3,3/5));
249 Msxjh4=((15/4)*Ljh*SINjh*int((Yss-y(4))*Srss(3,:),L2,1/3,3/5));
250 Msyjh4=((15/4)*Ljh*COSjh*int((Xss-x(4))*Srss(4,:),L2,1/3,3/5));
251 Msxjh5=((15/4)*Ljh*SINjh*int((Yss-y(5))*Srss(3,:),L2,1/3,3/5));
252 Msyjh5=((15/4)*Ljh*COSjh*int((Xss-x(5))*Srss(4,:),L2,1/3,3/5));
253 clear Srs Srss Xs Xss Ys Yss
254 %-----
255 %Assemble global stiffness matrix from CV equilibrium equations
256 %eqn.(4.29)
257 %-----
258 %node 1
259 %equilibrium in x stress
260 k(1,:)=(-(Fsxga+Ftyxga)+(Fsxgf+Ftyxgf));
261 %equilibrium in y stress
262 k(2,:)=(-(Fsyga+Ftxyga)+(Fsygf+Ftxygf));
263 %equilibrium of couple stress
264 k(3,:)=(-(Mxga+Myga)-Msxga1+Msyga1
265          +((Mxgf+Mygf)-Msxgf1+Msygf1));
266 %node 2
267 k(4,:)=(-(Fsxhc+Ftyxhc)+(Fsxhb+Ftyxhb));
268 k(5,:)=(-(Fsyhc+Ftxyhc)+(Fsyhb+Ftxyhb));
269 k(6,:)=(-(Mxhc+Myhc)-Msxhc2+Msyh2)
270          +((Mxhb+Myhb)-Msxhb2+Msyhb2));
271 %node 3
272 k(7,:)=(-(Fsxie+Ftyxie)+(Fsxid+Ftyxid));
273 k(8,:)=(-(Fsyie+Ftxyie)+(Fsyid+Ftxyid));
274 k(9,:)=(-(Mxie+Myie)-Msxie3+Msyie3)
275          +((Mxid+Myid)-Msxid3+Msyid3));
276 %node 4
277 k(10,:)=(-(Fsxhb+Ftyxhb)+(Fsxjh+Ftyxjh)
278           +((Fsxjg+Ftyxjg)+(Fsxga+Ftyxga)));
279 k(11,:)=(-(Fsyhb+Ftxyhb)+(Fsyjh+Ftxyjh)
280           +((Fsyjg+Ftxyjg)+(Fsyga+Ftxyga)));
281 k(12,:)=(-(Mxhb+Myhb)-Msxhb4+Msyhb4)-((Mxjh+Myjh)-Msxjh4+Msyjh4)
282          +((Mxjg+Myjg)-Msxjg4+Msyjg4)+((Mxga+Myga)-Msxga4+Msyga4));

```

```

283 %node 5
284 k(13,:) = -( (Fsxid+Ftyxid)+(Fsxji+Ftyxji))
285           + ( (Fsxjh+Ftyxjh)+(Fsxhc+Ftyxhc));
286 k(14,:) = -( (Fsyid+Ftxyid)+(Fsyji+Ftxyji))
287           + ( (Fsyjh+Ftxyjh)+(Fsyhc+Ftxyhc));
288 k(15,:) = -( (Mxid+Myid)-Msxid5+Msyid5)-( (Mxji+Myji)-Msxji5+Msyji5)
289           + ( (Mxjh+Myjh)-Msxjh5+Msyjh5)+ ( (Mxhc+Myhc)-Msxhc5+Msyh5);
290 %node 6
291 k(16,:) = -( (Fsxgf+Ftyxgf)+(Fsxjg+Ftyxjg))
292           + ( (Fsxji+Ftyxji)+(Fsxie+Ftyxie));
293 k(17,:) = -( (Fsygf+Ftxygf)+(Fsyjg+Ftxyjg))
294           + ( (Fsyji+Ftxyji)+(Fsyie+Ftxyie));
295 k(18,:) = -( (Mxgf+Mygf)-Msxgf6+Msygf6)-( (Mxjg+Myjg)-Msxjg6+Msyjg6)
296           + ( (Mxji+Myji)-Msxji6+Msyji6)+ ( (Mxie+Myie)-Msxie6+Msyie6);

```

Appendix C

MATLAB Iterative Constitutive Code

C.1 MicropolarBeamREGbeta Code

```
1 %MicropolarBeamREGbeta
2 %Author: A J Beveridge
3 %Created: 2010-03-01
4 %Modified: 2010-05-28
5 %For: To pick the correct constitutive properties to fit
6 %experimental data with a plane micropolar model.
7
8 clc
9 close all
10 clear all
11
12 CON=0.99; %target value of coefficient of multiple determination
13
14 ANSYSk=[2902642.537 6440910.148 18255016.34 %HMD ANSYS data
15 2195098.345 5018438.961 15222982.09
16 2043225.003 4705825.946 14587940.23
17 1982382.113 4556734.854 13998064.82];
18
```

```

19 depth=[0.0127;0.0254;0.0381;0.0508];
20 b=0.0127;
21 span=[10.08;7.56;5.04];
22 L_h=[10;7;5];
23 %-----
24 %Initial guess of Em and gamma from straight line fit
25 %-----
26 STIFF10=ANSYSk(:,1);
27 iGuess=polyfit(1./depth.^2,STIFF10,1);
28 Em=iGuess(2)/(4*b*(1/span(1))^3); %eqn.(3.1)
29 lb=sqrt(iGuess(1)/(4*b*Em*(1/span(1)^3))); %eqn.(3.1)
30 gamma=(lb^2*Em)/12; %eqn.(2.45)
31 N=0.25;
32 vm=0.3;
33 %-----
34 %Loop i for N using L/h=5.04
35 %-----
36 %calculate initial results from guessed material properties
37 for i=1:length(depth)
38     d=depth(i)
39     L=(span(3)*d)/2;
40     Lh=L_h(3);
41     %function containing CVFEM solution procedure
42     [CVFEMstif]=CVFEMsolution(L,d,b,Em,vm,gamma,N,Lh);
43     f(i)=CVFEMstif;
44     y(i)=ANSYSk(i,3);
45 end
46 %calculate coefficient of multiple determination
47 ymean=(1/length(y))*sum(y);
48 err=(y-f).^2;
49 tot=(y-ymean).^2;
50 SSerr=sum(err); %eqn.(5.2)
51 SStot=sum(tot); %eqn.(5.3)
52 R2i=1-(SSerr/SStot); %eqn.(5.1)
53 R2im=R2i;
54 %begin loop to optimise material property
55 while R2i<CON
56     for i=1:length(depth)
57         d=depth(i)
58         L=(span(3)*d)/2;

```

```

59         Lh=L_h(3);
60         [CVFEMstif]=CVFEMsolution(L,d,b,Em,vm,gamma,N,Lh);
61         f(i)=CVFEMstif;
62         y(i)=ANSYSk(i,3);
63     end
64     ymean=(1/length(y))*sum(y);
65     res=(y-f);
66     err=(y-f).^2;
67     tot=(y-ymean).^2;
68     SSerr=sum(err);
69     SStot=sum(tot);
70     R2i=1-(SSerr/SStot)
71     if R2im>R2i
72         Nm=N
73         break %break loop if R2 diverges from previous iteration
74     end
75     R2im=R2i
76     Nm=N
77     %update guess of the coupling number
78     N=(1/length(y))*sum((y./f))*Nm; %eqn.(5.4)
79 end
80 R2i=R2im;
81 N=Nm;
82 %-----
83 %Loop j for gamma using L/d=10.08
84 %-----
85 for i=1:length(depth)
86     d=depth(i)
87     L=(span(1)*d)/2;
88     Lh=L_h(1);
89     [CVFEMstif]=CVFEMsolution(L,d,b,Em,vm,gamma,N,Lh);
90     f(i)=CVFEMstif;
91     y(i)=ANSYSk(i,1);
92 end
93 ymean=(1/length(y))*sum(y);
94 err=(y-f).^2;
95 tot=(y-ymean).^2;
96 SSerr=sum(err);
97 SStot=sum(tot);
98 R2j=1-(SSerr/SStot);

```

```

99 R2jm=R2j;
100 while R2j<CON
101     for i=1:length(depth)
102         d=depth(i)
103         L=(span(1)*d)/2;
104         Lh=L_h(1);
105         [CVFEMstif]=CVFEMsolution(L,d,b,Em,vm,gamma,N,Lh);
106         f(i)=CVFEMstif;
107         y(i)=ANSYSk(i,1);
108     end
109     ymean=(1/length(y))*sum(y);
110     res=(y-f);
111     err=(y-f).^2;
112     tot=(y-ymean).^2;
113     SSerr=sum(err);
114     SStot=sum(tot);
115     R2j=1-(SSerr/SStot)
116     if R2jm>R2j
117         break
118     end
119     R2jm=R2j
120     gamma_c=gamma
121     gamma=(1/length(y))*sum((y./f))*gamma_c;
122 end
123 R2j=R2jm;
124 gamma=gamma_c;

```

Appendix D

Ansys Discrete Detail Input Files

D.1 HMD Geometry Input B1

```
1 fini
2 /clear
3 /prep7
4
5 NCx=8
6
7 ES=1
8 refine=1
9
10 pi=3.141592654
11 L1=0.016
12 L2=0.0127
13 r1=0.0035
14 r2=(1+(ES/10))*r1
15 r3=(1+(ES/10))*r2
16
17 et,1,183
18 keyopt,1,3,3
19 real,1
20 R,,0.0127
21
```

```

22 mp,ex,1,70.0E9
23 mp,prxy,1,0.3
24
25 k,,
26 k,,L1/2
27 k,,L1/2,L2/2
28 k,,,L2/2
29 k,,(L1/2)-(L1/2)/(10),
30 k,,(L1/2)-(L1/2)/(10),L2/2
31 k,,, (L2/2)-(L1/2)/(20)
32 k,,L1/2,(L2/2)-(L1/2)/(20)
33 k,,(L1/2)-(L1/2)/10,(L2/2)-(L1/2)/(20)
34
35 CIRCLE,1,r1,,,90,2
36 CIRCLE,1,r2,,,90,2
37
38 a,12,15,14,11,12
39 a,11,14,13,10,11
40 a,15,7,9,14,15
41 a,14,9,5,13,14
42 a,7,4,6,9,7
43 a,9,6,3,8,9
44 a,9,8,2,5,9
45
46 lesize,12,,,4*refine
47 lesize,8,,,4*refine
48 lesize,10,,,4*refine
49 lesize,1,,,9*refine
50 lesize,2,,,9*refine
51 lesize,3,,,9*refine
52 lesize,4,,,9*refine
53 lesize,5,,,1*refine
54 lesize,6,,,1*refine
55 lesize,7,,,1*refine
56 lesize,9,,,9*refine
57 lesize,11,,,9*refine
58 lesize,13,,,1*refine
59 lesize,14,,,9*refine
60 lesize,11,,,9*refine
61 lesize,15,,,1*refine

```

```

62 lesize,16,,,1*refine
63 lesize,17,,,1*refine
64 lesize,18,,,1*refine
65 lesize,19,,,9*refine
66 lesize,20,,,1*refine
67
68 mshkey,1
69 amesh,all
70
71 ARSYM,Y,all
72 ARSYM,X,all
73
74 *DO,X,1,NCx
75     AGEN,2,1,28,,X*L1,,,,0
76 *ENDDO
77
78 AGEN,2,1,14,,-(L1),
79
80 asel,all
81
82 NUMMRG,all,10E-6
83 NUMCMP,all

```

D.2 LMD Geometry Input B1

```

1 fini
2 /clear
3 /prep7
4
5 NCx=16
6 NCy=1
7
8 ES=1
9 refine=0.5
10
11 pi=3.141592654
12 L1=0.009

```

```

13 L2=0.0127
14 r1=0.0035
15 r2=(1+(ES/10))*r1
16 r3=(1+(ES/10))*r2
17
18
19 et,1,183
20 keyopt,1,3,3
21 real,1
22 R,,0.0127
23
24 mp,ex,1,70E9
25 mp,prxy,1,0.3
26
27 k,,
28 k,,L1/2
29 k,,L1/2,L2/2
30 k,,,L2/2
31 k,,, (L2/2)-(L1/2)/(2.5)
32 k,,L1/2, (L2/2)-(L1/2)/(2.5)
33
34 CIRCLE,1,r1,,,90,2
35 CIRCLE,1,r2,,,90,2
36
37 a,8,9,12,11,8
38 a,7,8,11,10,7
39 a,11,12,5,6,11
40 a,10,11,6,2,10
41 a,5,4,3,6,5
42
43 lesize,14,,,10*refine
44 lesize,9,,,10*refine
45 lesize,4,,,10*refine
46 lesize,2,,,10*refine
47 lesize,1,,,10*refine
48 lesize,3,,,10*refine
49 lesize,11,,,10*refine
50 lesize,7,,,1*refine
51 lesize,6,,,1*refine
52 lesize,5,,,1*refine

```

```
53 lesize,12,,,4*refine
54 lesize,10,,,4*refine
55 lesize,8,,,4*refine
56 lesize,13,,,5*refine
57 lesize,15,,,5*refine
58
59 mshkey,1
60 amesh,all
61
62 ARSYM,Y,all
63 ARSYM,X,all
64
65 *DO,X,1,NCx
66     AGEN,2,1,20,,X*L1,,,,0
67 *ENDDO
68
69 AGEN,2,1,10,,-(L1),
70
71 asel,all
72
73 NUMMRG,all,10E-6
74 NUMCMP,all
```

Bibliography

- [1] L. J. Gibson and M. F. Ashby. *Cellular Solids*. Cambridge University Press, 1999.
- [2] C. Tekoglu and P. Onck. Size effects in two-dimensional voronoi foams: A comparison between generalized continua and discrete models. *Journal of the Mechanics and Physics of Solids*, 56(12):3541–3564, December 2008.
- [3] M. H. Sadd. *Elasticity : theory, applications, and numerics*. Elsevier Butterworth Heinemann, 2005.
- [4] R. D. Mindlin and H. F. Tiersten. Effects of couple-stresses in linear elasticity. *Archive for Rational Mechanics and Analysis*, 11(1):415–448, January 1962.
- [5] A. C. Eringen. Linear theory of micropolar elasticity. *Journal of Mathematics and Mechanics*, 15(6):909–923, 1966.
- [6] W. Nowacki. *Theory of Micropolar Elasticity*. Springer-Verlag, 1972.
- [7] A. C. Eringen. *Microcontinuum Field Theories I: Foundations and Solids*. Springer-Verlag New York, 1999.
- [8] P. Neff. The cosserat couple modulus for continuous solids is zero viz the linearized cauchy-stress tensor is symmetric. *ZAMM*, 86(11):892–912, 2006.
- [9] R. D. Gauthier. *Experimental investigations of micropolar media*. World Scientific, Singapore, 1981.

- [10] R. D. Gauthier and W. E. Jahsman. A quest for micropolar elastic constants. *Journal of Applied Mechanics*, 42:369–374, 1975.
- [11] D. Bigoni and W. J. Drugan. Analytical derivation of cosserat moduli via homogenization of heterogeneous elastic materials. *Journal of Applied Mechanics*, 74(4):741–753, 2007.
- [12] R. S. Lakes. Experimental methods for study of cosserat elastic solids and other generalized elastic continua. *Continuum models for materials with micro-structure*, 1995.
- [13] R.S. Lakes. Size effects and micromechanics of a porous solid. *Journal of Materials Science*, 18(9):2572–2580, September 1983.
- [14] G.V. Krishna Reddy and N.K. Venkatasubramanian. On the flexural rigidity of a micropolar elastic circular cylinder. *Journal of Applied Mechanics*, 45:429–431, 1978.
- [15] R.S. Lakes. Experimental microelasticity of two porous solids. *International Journal of Solids and Structures*, 22(1):55–63, 1986.
- [16] J.F.C Yang and R.S. Lakes. Experimental study of micropolar and couple stress elasticity in bone in bending. *Journal of Biomechanics*, 15:91–98, 1982.
- [17] W. B. Anderson and R. S. Lakes. Size effects due to cosserat elasticity and surface damage in closed-cell polymethacrylimide foam. *Journal of Materials Science*, 29(24):6413–6419, January 1994.
- [18] H. C. Park and R. S. Lakes. Torsion of a micropolar elastic prism of square cross-section. *International Journal of Solids and Structures*, 23(4):485–503, 1987.
- [19] R. S. Lakes, D. Gorman, and W. Bonfield. Holographic screening method for microelastic solids. *Journal of Materials Science*, 20(8):2882–2888, 1985.
- [20] P. M. Buechner and R. S. Lakes. Size effects in the elasticity and viscoelasticity of bone. *Biomechanics and Modeling in Mechanobiology*, 1(4):295–301, April 2003.

- [21] A. W. McFarland and J. S. Colton. Role of material microstructure in plate stiffness with relevance to microcantilever sensors. *Journal of Micromechanics and Microengineering*, 15(5):1060–1067, May 2005.
- [22] J. E. Goldberg, M. H. Baluch, T. Korman, and S. L. Koh. Finite element approach to bending of micropolar plates. *International Journal for Numerical Methods in Engineering*, 8(2):311–321, 1974.
- [23] M. H. Baluch and J. E. Goldberg. Finite element approach to plane microelasticity. *Journal of the Structural Division (ASCE)*, ST9:1957–1964, 1972.
- [24] N. Sahoo. Finite element method for orthotropic micropolar elasticity. *International Journal of Engineering Science*, 22(3):319–330, 1984.
- [25] E. Providas. Finite element method in plane cosserat elasticity. *Computers & Structures*, 80(27-30):2059–2069, November 2002.
- [26] M. A. Wheel. A control volume-based finite element method for plane micropolar elasticity. *International Journal for Numerical Methods in Engineering*, 75(8):992–1006, 2008.
- [27] S. Nakamura and R. S. Lakes. Finite element analysis of Saint-Venant end effects in micropolar elastic solids. *Engineering Computations*, 12:571–587, 1995.
- [28] L. Li and S. Xie. Finite element method for linear micropolar elasticity and numerical study of some scale effects phenomena in mems. *International Journal of Mechanical Sciences*, 46(11):1571–1587, November 2004.
- [29] U. Yang D and Y. Huang F. Analysis of poissons ratio for a micropolar elastic rectangular plate using the finite element method. *Engineering Computations: Int J for Computer-Aided Engineering*, pages 1012–1030, 2001.
- [30] H. Zhang, H. Wang, B. Chen, and Z. Xie. Analysis of cosserat materials with voronoi cell finite element method and parametric variational principle. *Computer Methods in Applied Mechanics and Engineering*, 197(6-8):741–755, January 2008.

- [31] F. Y. Huang, B. H. Yan, J. L. Yan, and D. U. Yang. Bending analysis of micropolar elastic beam using a 3-D finite element method. *International Journal of Engineering Science*, pages 275–286, February 2000.
- [32] D. Branke, J. Brummund, G. Haasemann, and V. Ulbricht. Finite element (FE) simulation of textile-reinforced composites using a cosserat element. *PAMM*, 8(1):10537–10538, 2008.
- [33] P. Hutapea and P. Qiao. Micropolar in-plane shear and rotation moduli of unidirectional fiber composites with fiber-matrix interfacial. *Journal of Composite Materials*, 36(11):1381–1399, June 2002.
- [34] P. Hutapea, F. G. Yuan, and N. J. Pagano. Micro-stress prediction in composite laminates with high stress gradients. *International Journal of Solids and Structures*, pages 2215–2248, May 2003.
- [35] F. Y. Huang, B. H. Yan, J. L. Yan, and D. U. Yang. Bending analysis of micropolar elastic beam using a 3-D finite element method. *International Journal of Engineering Science*, 38(3):275–286, 2000.
- [36] ANSYS[®] Academic Research, Release 12.1, Mechanical APDL, ANSYS, Inc.
- [37] R. D. Cook, D. S. Malkus, and M. E. Plesha. *Concepts and Applications of Finite Element Analysis*. John Wiley & Sons, 1989.
- [38] MATLAB[®] Student Version, R2009a 7.8.0.347, The MathWorks[™], Inc.
- [39] B. R. Baliga and S. V. Patankar. A new finite-element formulation for convection-diffusion problems. *Numerical Heat Transfer*, 3(4):393–409, 1980.
- [40] I. Demirdzic and S. Muzaferija. Finite volume method for stress analysis in complex domains. *International Journal for Numerical Methods in Engineering*, 37(21):3751–3766, 1994.
- [41] G. A. Taylor, C. Bailey, and M. Cross. A vertex-based finite volume method applied to non-linear material problems in computational solid mechanics. *International Journal for Numerical Methods in Engineering*, 56(4):507–529, 2003.

- [42] I. Bijelonja, I. Demirdzic, and S. Muzaferija. A finite volume method for incompressible linear elasticity. *Computer Methods in Applied Mechanics and Engineering*, 195(44-47):6378–6390, September 2006.
- [43] P. Wenke and M. A. Wheel. A finite volume method for solid mechanics incorporating rotational degrees of freedom. *Computers & Structures*, 81(5):321–329, March 2003.
- [44] M. A. Wheel. A finite volume method for analysing the bending deformation of thick and thin plates. *Computer Methods in Applied Mechanics and Engineering*, 147(1-2):199–208, July 1997.
- [45] N. Fallah. A cell vertex and cell centred finite volume method for plate bending analysis. *Computer Methods in Applied Mechanics and Engineering*, 193(33-35):3457–3470, August 2004.
- [46] MATLAB[®] Student Version, R14 sp3 7.1.0.124, The MathWorks[™], Inc.
- [47] J. L. Batoz. An explicit formulation for an efficient triangular plate-bending element. *International Journal for Numerical Methods in Engineering*, 18(7):1077–1089, 1982.
- [48] C. Jeyachandrabose, J. Kirkhope, and R. C. Babu. An alternative explicit formulation for the dkt plate-bending element. *International Journal for Numerical Methods in Engineering*, 21(7):1289–1293, 1985.
- [49] G. Gendron. A review of four PC packages for FE structural analysis. *Finite Elements in Analysis and Design*, 28(2):105–114, December 1997.
- [50] H. D. Bui. *Inverse problems in the mechanics of materials : an introduction*. CRC Press, 1994.
- [51] G. Partheepan, D. K. Sehgal, and R. K. Pandey. An inverse finite element algorithm to identify constitutive properties using dumb-bell miniature specimen. *Modelling and Simulation in Materials Science and Engineering*, 14(8):1433–1445, December 2006.

- [52] A. Husain. An inverse finite element procedure for the determination of constitutive tensile behavior of materials using miniature specimen. *Computational Materials Science*, 31(1-2):84–92, September 2004.
- [53] N. R. Draper and H. Smith. *Applied Regression Analysis*. Wiley, 1966.
- [54] ALTUGLAS[®] Cast & Extruded Sheet Technical Brochure, Altuglas International, Arkema Group.
- [55] J. L. Batoz, K. J. Bathe, and L. W. Ho. A study of three-node triangular plate bending elements. *International Journal for Numerical Methods in Engineering*, 15(12):1771–1812, 1980.
- [56] S. Timoshenko. *Theory of Plates and Shells*. McGraw-Hill, 1987.